# IMPROVED PERFORMANCE OF LEDS USING SHADOW MASK DEPOSITION OF NON-PLANAR DIELECTRICS

Thesis

Submitted to

The School of Engineering of the

UNIVERSITY OF DAYTON

in Partial Fulfillment of the Requirements for

The Degree

Master of Science in Electro-Optics

by

Sarah Beth Blickenstaff

UNIVERSITY OF DAYTON

Dayton, Ohio

December, 2004

IMPROVED PERFORMANCE OF LEDS USING SHADOW MASK DEPOSITION OF NON-PLANAR DIELECTRICS

APPROVED BY:

Andrew M. Sarangan, Ph.D.
Assistant Professor,
Electro-Optics Program
University of Dayton
Committee Chairman

Joseph W. Haus, Ph.D.
Director and Professor,
Electro-Optics Program
University of Dayton
Committee Member

Thomas R. Nelson, Ph.D.
Research Physicist,
Sensors Directorate
Air Force Research Laboratory
Committee Member

Donald L. Moon, Ph.D.
Associate Dean
Graduate Engineering Programs & Research
School of Engineering

Joseph E. Saliba, Ph.D., P.E.
Dean, School of Engineering

# ABSTRACT

IMPROVED PERFORMANCE OF LEDS USING SHADOW MASK DEPOSITION OF NON-PLANAR DIELECTRICS

Sarah Beth Blickenstaff
University of Dayton

Advisor: Dr. Andrew M. Sarangan

Light emitting diodes (LEDs) play an important role in telecommunication networks and display systems. In this paper, we describe a cost-efficient method for improving the brightness and overall efficiency of LEDs. In the first section of this thesis, we report on the deposition of non-planar $SiO_2$ and $SiN_x$ dielectric layers using plasma-enhanced chemical vapor deposition (PECVD), RF-sputtering and reactive RF-sputtering through metal and dielectric shadow masks. The layers were analyzed for trends in deposition rate and curvature as a function of shadow mask material and geometry, as well as the deposition method. Increasing the top hole diameter, which is the limiting aperture of the shadow mask cavity, increased the rate of deposition inside the cavity, but it also decreased the curvature of the resulting aspheric microlens. As the height of the shadow mask cavity was increased, both the cavity deposition rate and microlens curvature increased. $SiO_2$ deposited by PECVD produced aspheric microlenses with the most curvature, while sputtering $SiO_2$ produced microlenses with the highest process efficiency. Using an alumina shadow mask created microlenses with higher deposition

rates and more curvature than a nickel shadow mask for each deposition method. In the second section of this thesis, we report on the use of these results to fabricate a shadow mask from which single layer dielectric encapsulations were deposited onto the emitting surfaces of LEDs, and compared to neighboring bare LEDs to determine the percent increase of emission created by adding the encapsulation. The intensity of emission of a LED with an aspheric encapsulation increased the emitted power, thus the extraction efficiency, of the LED. Increasing the curvatures of the encapsulations increased the percent increase of emission of the LEDs. Increasing the emitting aperture diameters of the extended source LEDs decreased their percent increase of emission. A calculation was performed that simulated the relative extraction efficiency of an encapsulated LED to a bare LED as a function of emitting aperture diameter to compare the experimental data to theory. The simulation showed that the relative extraction efficiency of a hemispherically encapsulated, extended source LED decreases with increasing emitting aperture diameter.

ACKNOWLEDGEMENTS

I would like to thank Dr. Andrew Sarangan, my advisor, and Dr. Thomas Nelson (Air Force Research Laboratory) for originating the idea for this research. They have guided me through the research process and provided me with the help I needed to complete this project. I would also like to thank Dr. Kevin Leedy (AFRL) for providing the expertise regarding sputtering of the dielectric materials. Donald Agresta (AFRL) helped with the deposition of dielectrics by PECVD. James Ehret (AFRL) grew the epitaxial layers of the LED using his extensive knowledge of molecular beam epitaxy (MBE).

TABLE OF CONTENTS

## LIST OF ILLUSTRATIONS

## LIST OF TABLES

# CHAPTER I

# INTRODUCTION

The problem presented in this thesis involves the use of one method to create many possibilities. This technique for deposition of non-planar dielectric layers can, with a few minor adjustments, alleviate many of the issues inherent in the current approaches to microlens formation. In this thesis, we present a detailed study of the trends in the deposition of dielectric materials through a shadow mask, with the goal of producing layers that possess sufficient curvature to improve the emission from surface emitting light emitting diodes (LEDs) and lasers. The dimensions of the shadow mask cavities were varied to observe the changes in curvatures and thicknesses of the deposited dielectric layers. The shadow mask was constructed from two different materials to determine their effect on microlens shape and thickness. Finally, the deposition method and deposited species were varied to examine which technique produced optimized microlens characteristics. The results from the shadow mask development study were used to deposit microlenses using the best shadow mask material, shadow mask cavity geometries, deposition method and dielectric materials. The microlenses were deposited onto the emitting surface of LEDs to verify the enhancement of the output power of the devices.

This study is very important to the field of optoelectronics because it offers a solution to some of the issues facing the telecommunications and lighting industries. The never-ending goal of these industries is to find a light source that can produce more output power for the same amount of input current, as well as maintaining or decreasing fabrication time and expense. LEDs and resonant-cavity LEDs (RC-LEDs) with more output power can be used in lighting and display systems that are brighter and more energy efficient than the conventional systems used today. A vertical cavity surface emitting laser (VCSEL) oscillating at the lowest-order transverse mode profile will have brighter emission that couples better into fibers, thus reducing the need for in-line signal amplifiers for fiber-based telecommunications networks. These goals could be accomplished with the technique for depositing non-planar dielectric layers described in this thesis.

The shadow mask development study yielded many important conclusions pertaining to how the shadow mask material, geometry and deposition method affected the microlens curvature and thickness. The shadow mask made from alumina produced aspheric microlenses with greater thicknesses and curvatures than those produced from nickel. Smaller shadow mask cavity height proved to greatly increase microlens thickness and curvature. In contrast, increasing the diameter of the circular aperture at the top of the shadow mask cavity produced microlenses with greater thicknesses but less curvature. The deposition method and material that produced microlenses with the most curvature was plasma-enhanced chemical vapor deposition (PECVD) of $SiO_2$, while the method with the highest process efficiency was RF-sputtering of $SiO_2$.

Encapsulating LEDs with aspheric dielectric microlenses by depositing dielectric material with a shadow mask enhanced the output power of the LEDs. This result was caused by the encapsulation increasing the extraction efficiency of the LED. The output power of LEDs with aspheric dielectric encapsulations was compared to the output power of an LED with a planar dielectric layer with a thickness similar to the thickness of the aspheric encapsulation. In three out of six instances, the LEDs with the aspheric dielectric encapsulations increased the output power of the LEDs more than the LEDs with the planar dielectric layer. The output power of the LEDs decreased with decreasing curvature of the aspheric dielectric encapsulation. As the emitting apertures of the LEDs were increased, the output power of the LEDs with aspheric dielectric encapsulations decreased. This was attributed to the fact that the LEDs that were tested were extended sources, not point sources. A calculation was performed that showed how the extraction efficiency of an extended source LED with an aspheric dielectric encapsulation decreased with increasing emitting aperture diameter, thus validating the experimental results.

# CHAPTER II

# REVIEW OF LED EFFICIENCY

## LED Efficiency

LEDs consist of a P-N junction into which minority carriers are injected. As the holes travel into the n-type material and the electrons into the p-type material, the electrons and holes recombine to release a photon. The radiative recombination of electrons and holes is known as a photoluminescent process. In an ideal LED, every recombination of an electron and hole would result in the emission of a photon from the device. The L-I relation of a perfect LED (if that were possible) could be represented as

$$\frac{L}{I} = \frac{h\upsilon}{q}.$$

Here $I$ is the injected current in Amperes and $L$ is the light output power in Watts. In real devices, photons can be re-absorbed in the semiconductor material or reflected back into the semiconductor at the LED/air interface if its angle of incidence with the interface doesn't fall within a specific range of angles. Another issue with semiconductor materials is that they can contain defects, such as foreign materials or inconsistencies in crystal growth, including the surface. The electron-hole recombination near the defects can result in non-radiative recombination in which a phonon is emitted instead of a photon, causing

lattice vibration. The overall efficiency of an LED is a measure of the imperfections present in a specific LED design and is included in the L-I expression that becomes

$$\frac{L}{I} = \frac{h\upsilon}{q}\eta_o .$$

In this equation, $\eta_o$ is the overall efficiency of an LED presented as the percentage of electron-hole recombinations that form a photon that is emitted out of the top surface of the LED. The overall efficiency of an LED is the product of the injection, recombination and extraction efficiencies.

The injection efficiency of an LED can be described by either the electron or hole injection efficiency. Both descriptions indicate the ratio of the minority carrier (electron or hole) density to the total current density injected into an LED. For the example of injecting minority carriers (electrons) into the p-side of the P-N homojunction, the electron injection efficiency can be expressed, using the carrier diffusion equations, as

$$\eta_{inj} = \left(1 + \frac{\mu_p L_n N_A}{\mu_n L_p N_D}\right)^{-1} .$$

Here $\mu_p$ and $\mu_n$ are the hole and electron mobilities, $L_p$ and $L_n$ are the minority carrier diffusion lengths and $N_A$ and $N_D$ are the dopant levels of acceptor and donors in the p- and n-type materials, respectively. In a GaAs-based semiconductor LED, the holes have mobilities that are about 20 times smaller than the mobilities for the electrons. In an LED where $N_A$ and $N_D$ are equal, the difference in electron and hole mobilities causes most of the electron-hole recombinations to take place on the p-side of the homojunction and the electron injection efficiency to be greater than the hole injection efficiency. Since the electron injection efficiency is dependant on doping levels in the semiconductor

materials, the ratio can be increased by growing the n-type material so that $N_D$ is much larger than $N_A$, which increases the donor concentration on the n-side of the homojunction. Conversely, to increase the hole injection efficiency, the level of dopants in the p-side ($N_A$) can be increased. However, doping a semiconductor to too high a level can result in a decrease in radiative recombinations due to increased nonradiative recombination pathways in the material. The injection efficiency in a GaAs-based semiconductor LED can be made approximately 80%.

Recombination efficiency (also known as internal quantum efficiency) is the ratio of radiative recombinations to the radiative plus nonradiative recombinations. The radiative recombination of an electron-hole pair produces a photon, while a nonradiative recombination produces a phonon. A defect in the semiconductor can cause a nonradiative recombination rather than a radiative one. Defects in the semiconductor material can be caused by introducing foreign substances into the crystal lattice or by defects in the lattice structure. The semiconductor/air interface is considered a defect since it is an inconsistency in the lattice structure. Near the surface, where the photons will exit, the recombination efficiency is low because nonradiative recombinations out number radiative recombinations. Expressed in terms of radiative and nonradiative carrier lifetimes, the recombination efficiency is

$$\eta_r = \frac{\tau_{nr}}{\tau_{nr} + \tau_r} = \frac{1}{1 + \frac{\tau_r}{\tau_{nr}}}.$$

In this equation, $\tau_{nr}$ is the nonradiative carrier lifetime and $\tau_r$ is the radiative carrier lifetime. The recombination efficiency can be increased by either reducing the radiative carrier lifetime or increasing the nonradiative carrier lifetime. Reducing the radiative

carrier lifetime will increase the rate of radiative recombinations, while increasing the lifetime of the nonradiative carriers will slow the rate of nonradiative recombinations. The recombination efficiency of an LED with a GaAs-based homojunction is about 50%, while introducing a double heterojunction into the LED structure increases it to 80%. By creating the active region from quantum wells, the recombination efficiency will be brought close to unity.

The extraction efficiency of an LED is a comparison of the number of photons that exit the device to the total number of photons generated from the active region. Photons are generated in all directions from the active region of the LED, not only directed toward the exit window. The extraction efficiency is affected by the angle that the photon intersects with the exit window. The photons that strike the exit window at an angle greater than or equal to the critical angle are reflected off of the surface and back into the device because of total internal reflection (TIR). The critical angle can be expressed as

$$\theta_c = \sin^{-1}\left(\frac{n_2}{n_1}\right).$$

Here $n_2$ is the index of refraction of air, or 1.0, and $n_1$ is the refractive index of the semiconductor, which is about 3.5 for typical GaAs-base LEDs. For a GaAs-based LED, the critical angle is 17°, meaning that every photon that strikes the exit window at an angle of 17° or greater from the normal will be reflected back into the semiconductor. The only photons that make it through the exit window are the ones that strike the surface at angles less than the critical angle. Assuming the emission to be a Lambertian source, the extraction efficiency of an LED with a point source emission area can be expressed as

$$\eta_{ext} = \frac{1}{2}\left(\frac{n_a}{n_s}\right)^2\left[1-\left(\frac{n_s - n_a}{n_s + n_a}\right)^2\right].$$

In this equation, $n_a$ is the refractive index of air and $n_s$ is the refractive index of the semiconductor. Typical values for the extraction efficiency with a GaAs-based semiconductor structure are about 2%. The extraction efficiency of a bare GaAs-based LED is the limiting factor of overall efficiency because of its low value. The overall LED efficiency becomes

$$\eta_o = \eta_{inj} \times \eta_r \times \eta_{ext}.$$

## Encapsulated LED Extraction Efficiency

The extraction efficiency of an LED can be improved by incorporating an encapsulation onto the emitting surface of the device. Typically, an epoxy hemisphere is created to encapsulate an LED, which creates a higher critical angle at the semiconductor/epoxy interface than the semiconductor/air interface of a bare LED. This is due to the smaller difference in refractive indices of the semiconductor and epoxy compared to the difference between the refractive indices of the semiconductor and air. Compared to the 17° critical angle of the bare LED at the semiconductor/air interface, the addition of the epoxy to the semiconductor increases the critical angle at the semiconductor/epoxy interface to about 35° (for an epoxy with a refractive index of 2.0). This allows more of the photons generated at the active region to be transmitted through the interface and into the epoxy. The hemispherical encapsulation allows almost all of photons that make it into the epoxy to travel through the air/epoxy interface unimpeded. This occurs because the hemispherical dome creates nearly perpendicular angles of

incidence at the epoxy/air interface for most photons coming from the semiconductor/epoxy interface, preventing reflection of the photons at the air/epoxy interface. A set of point source LED calculations are presented here that compare the improvement of the extraction efficiency by encapsulating an LED with a planar dielectric layer and a hemispheric dielectric layer. The dielectric is $n_d$ with a refractive index of 2.0 and $n_s$ is the semiconductor with refractive index of 3.5.

Bare LED

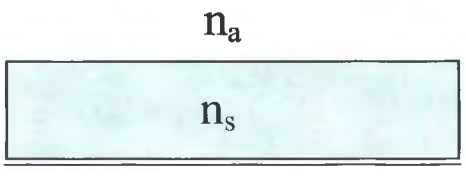


**Figure 2.1** Diagram of a semiconductor LED ($n_s$), where the exit window is adjacent to air ($n_a$)

$$\eta_{ext} = \frac{1}{2}\left(\frac{n_a}{n_s}\right)^2\left[1-\left(\frac{n_s-n_a}{n_s+n_a}\right)^2\right]$$

$$\eta_{ext} = \frac{1}{2}\left(\frac{1}{3.5}\right)^2\left[1-\left(\frac{3.5-1}{3.5+1}\right)^2\right]$$

$$\eta_{ext} = 0.028 = 2.8\%$$

Planar Dielectric Encapsulation

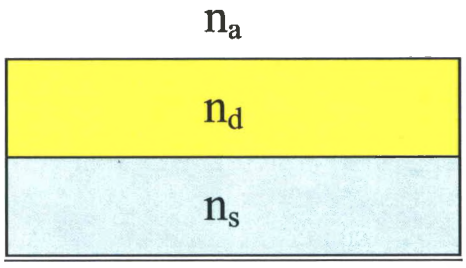


**Figure 2.2** Diagram of a semiconductor LED ($n_s$) with a planar dielectric layer ($n_d$)

$$\eta_{ext} = \frac{1}{2}\left(\frac{n_a}{n_s}\right)^2\left[1-\left(\frac{n_s-n_d}{n_s+n_d}\right)^2\right]\left[1-\left(\frac{n_d-n_a}{n_d+n_a}\right)^2\right]$$

$$\eta_{ext} = \frac{1}{2}\left(\frac{1}{3.5}\right)^2\left[1-\left(\frac{3.5-2.0}{3.5+2.0}\right)^2\right]\left[1-\left(\frac{2.0-1}{2.0+1}\right)^2\right]$$

$$\eta_{ext} = 0.034 = 3.4\%$$

The addition of a planar dielectric encapsulation to the LED increases the extraction efficiency, but only by about 1%. Although the lower index contrast of the semiconductor/dielectric interface increases the extraction from that interface, there is still the issue of TIR at the next interface. The dielectric/air interface has a critical angle of 30°, meaning that a large fraction of the photons that are transmitted into the dielectric are totally internally reflected off of the dielectric/air interface and back into the

dielectric. The combination of the reflected photons at both planar interfaces reduces the effect of increasing the critical angle by adding a dielectric layer.

Hemispheric Dielectric Encapsulation

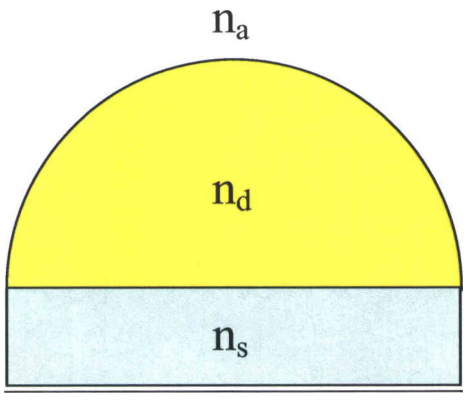


**Figure 2.3** Diagram of a semiconductor LED ($n_s$) with a hemispheric dielectric layer ($n_d$)

$$\eta_{ext} = \frac{1}{2}\left(\frac{n_d}{n_s}\right)^2\left[1-\left(\frac{n_s-n_d}{n_s+n_d}\right)^2\right]\left[1-\left(\frac{n_d-n_a}{n_d+n_a}\right)^2\right]$$

$$\eta_{ext} = \frac{1}{2}\left(\frac{2.0}{3.5}\right)^2\left[1-\left(\frac{3.5-2.0}{3.5+2.0}\right)^2\right]\left[1-\left(\frac{2.0-1}{2.0+1}\right)^2\right]$$

$$\eta_{ext} = 0.134 = 13.4\%$$

By creating the encapsulation with a spherical shape, the full effect of lowering the index contrast at the semiconductor/dielectric interface is realized. The range of angles

allowed into the dielectric more than doubles by the increase of the critical angle at this interface to 35°. For this point source calculation, the hemispherical dielectric/air interface does not reflect most of the photons being transmitted through the semiconductor/dielectric interface. Since the LED is a Lambertian source with an intensity profile of $I = I_o * \cos^n(\theta)$ and most of the intensity is concentrated around $\theta = 0$, the increase of the range of angles allowed into the dielectric layer greatly increases the intensity of light that is emitted from the LED. The increase in extraction efficiency by adding a hemispherical encapsulation would be maximized by creating the encapsulation out of a material with an index of refraction that equaled the semiconductor.

# CHAPTER III

# CURRENT APPROACHES TO MICROLENS FORMATION

In this chapter, the different approaches available for fabricating microlenses are described.

## Grayscale Lithography

There are two main approaches for creating grayscale masks. The first approach is to spatially change the transmission coefficient of the photomask. This can be achieved by using a high energy beam sensitive (HEBS) glass as the substrate material, and writing the pattern with an e-beam lithography system. The dosage from the e-beam directly alters the transmission coefficient of the photomask. The second approach is to create an array of on/off binary patterns on a standard photomask, with feature sizes smaller the diffraction limit of the lithography system. The density of the arrays can be used to control the amount of light incident on the photoresist. This can be achieved by combining the pulse width modulation (PWM) and pulse density modulation (PDM) methods [1]. In PWM, the pixel size in an array of evenly spaced pixels is modulated to adjust the intensity of light through the photomask. PDM changes the space between pixels of the same size to change the light throughput of the photomask. The alteration of both pixel size and spacing within a photomask assures the level of light intensity through

the mask conforms to the amount specified by the design, thus increasing the accuracy of which the 3D structure will be transferred to the photoresist.

Grayscale lithography can also create hemispherical microlenses without the need for photoresist. This is achieved by using a grayscale photomask to transfer a 3D hemispherical pattern into a negatively photosensitive hybrid sol-gel glass material [2]. Patterning the end material directly eliminates the need to etch the structure patterned in photoresist into the end material, saving time and expense. The intensity of light through the photomask can vary in steps from the center of the microlens design. Varying the intensity of light that strikes the sol-gel changes the amount of polymerization that occurs within the hybrid glass. A decrease in polymerization of the sol-gel results in smaller thickness of glass after development, thus leaving behind a convex, spherical microlens.

## Thermal Reflow

Thermal reflow of a cylinder of material can create hemispherical microlenses. Heating and reflow of negatively photosensitive hybrid sol-gel glass material creates hemispherical microlenses without the need for patterning and etching of photoresist or grayscale lithography [3]. A photomask exposes the circular hole pattern into the sol-gel. The unexposed material develops away to leave cylinders of sol-gel with the same diameter as the circular holes in the photomask. An oven heats the sol-gel cylinders at a temperature high enough to melt the sol-gel, thus forming hemispherical shapes by the surface-tension effect.

The diameter of a spherical microlens produced by thermal reflow can be controlled by heating a cylinder of photoresist located on top of another cylinder, with a slightly

larger diameter than the photoresist cylinder, made of a material with a higher melting point than the photoresist [4]. Lithographic processes form the pedestals from thin film aluminum. The heated cylinders of photoresist, resting on top of the aluminum pedestals, melt to form the microlenses. The spreading of the material from heating is prevented because the edge of the pedestal satisfies any surface contact angle. The resulting hemispherical microlenses have diameters that match the diameters of the pedestals.

Another method of producing hemispheric microlenses from photoresist involves exposing PMMA to x-ray radiation [5]. The x-ray mask is fabricated with a Au absorbing layer everywhere except for circular apertures consisting of a thin silicon layer, which is transparent to x-rays. The x-rays break some of the bonds in the polymer chains of the PMMA, causing its average molecular weight to decrease. This also reduces the glass transition temperature ($T_g$) of the PMMA, or the temperature at which the polymer undergoes the phase change from a plastic to a glass. When the PMMA is heated, the lower $T_g$ of the exposed polymer region causes the volume to expand. The surface tension of the expanded layer of the PMMA causes the heated photoresist to form a hemispherical shape. The heights of the resulting microlenses increase with increased heating temperature.

## Replication with Mold

Several methods for mass production of spherical microlenses utilize a negative mold of master microlenses. A nickel mold can produce microlenses made from a polymer [6]. The master mold is patterned from an array of microlenses formed by thermal reflow of photoresist. Electroformed nickel on the surface of the master microlenses forms the

negative mold. To form the microlenses, a heated press melts and presses the optical grade PMMA powder into the nickel mold. The melted PMMA conforms to the nickel mold, cools to room temperature and is released from the mold. A similar method by Moon *et al* [6] utilizes a UV curable photopolymer to mass-produce microlenses [7]. The same process is used to develop a negative nickel mold from master microlenses formed by thermal reflow. UV radiation cures the photopolymer after injection into the nickel mold, with and without applied pressure, to initiate cross-linking of the monomers.

The molding technique can also create mechanically flexible molds made of an elastomer instead of a nickel [8]. These molds offer the advantage of releasing from the molded microlenses easily and nondestructively. A heated press forms the elastomer against the lens master array and thermally cures the elastomer to form the mold. The placement of the mold on a glass plate ensures that it does not deform during the subsequent processes. Silica nanoparticles in a UV curable epoxy initiate polymer cross-linking with the epoxy during UV curing. The epoxy is spread on top of the elastomer mold and covered with a quartz plate. After the setup is exposed to UV radiation, the mold is separated from the cured epoxy, leaving the epoxy microlenses adhered to the quartz plate. A similar method to that developed by Kunnavakkam *et al* [8] involves UV curing of sol-gel glass instead of the epoxy loaded with silica nanoparticles [9]. The elastomer mold is pressed into the sol-gel glass and UV cured to form thick microlenses.

### Thermal Reflow and Dry Etch

Etching techniques can transfer the hemispherical patterns created by thermal reflow of photoresist to the substrate material. This can be achieved by using inductively

coupled plasma (ICP) to etch a photoresist pattern into a sapphire substrate [10]. Heating photoresist to a temperature above the glass transition temperature creates the initial spherical microlenses. An ICP system etches the photoresist microlenses and sapphire substrate, in which a radio frequency (RF) power generator delivers inductive power to create plasma from a 1:1 mixture of $BCL_3$ and $Cl_2$ gases. The etch rate of sapphire is less than that for the photoresist; therefore, the microlenses etched into the sapphire have radii of curvature higher than the original photoresist microlenses.

A similar technique to make spherical microlenses incorporates GaN and AlN substrates to form the microlenses [11]. Thermal reflow of cylindrical photoresist posts forms the master microlens array on GaN and AlN substrates. A similar chlorine-based ICP etching technique described by Park *et al* [10] transfers the lens structure to the substrates. GaN and AlN substrates were chosen over sapphire to integrate growth of III-nitride optoelectronic devices with microlenses. These substrates allow the devices to be operated at blue and ultraviolet wavelengths. GaN is transparent down to 370nm in wavelength, while deep UV applications require an AlN-based material system that is transparent to a wavelength of 200nm.

## Selective Wet Etch

The formation of spherical microlenses in semiconductor material can be conducted by exploiting the diffusion-limited etching properties of a $Br_2$ solution [12]. PECVD forms a mask layer of SiN onto GaAs and InP substrates. Photolithography and reactive ion etching (RIE) create circular holes through the SiN mask layer and into the semiconductor. When placing the patterned semiconductor in a solution of HBr : $H_2O_2$ :

$H_2O$ with the ratio of 2 : 1 : 60, the etchant does not etch the SiN mask layer, however, the $Br_2$ molecules will attack the exposed semiconductor. The $Br_2$ molecules will concentrate near the edge of the circular semiconductor hole due to their low mobility. This causes the etch rate to increase near the edge of the circle, creating a convex spherical lens at the bottom of the semiconductor hole. Increasing the time the patterned semiconductor is immersed in the etching solution increases the curvature of the microlens and its sag height. Placing the etched semiconductor into a solution of hydrofluoric acid (HF) removes the remaining SiN mask layer.

Diffusion-limited wet etching can also fabricate spherical microlenses from an InP/InGaAsP substrate [13]. Metalorganic chemical vapor deposition (MOCVD) epitaxially grows the InGaAsP layer to be lattice-matched to the InP substrate. Photolithography techniques pattern circular holes into a mask layer of photoresist. Immersing the semiconductor and photoresist pattern in a solution of $HBr\text{-}H_3PO_4\text{-}(0.5M)K_2Cr_2O_7$ with a ratio of 1 : 1 : 1 produces an etch rate that is equal for both the InP and InGaAsP layers. This ratio of solution components provides the lowest surface roughness of the resulting microlenses and ensures that the photoresist mask layer is not attacked during the etching process. The photoresist mask layer is removed with solvents.

## Focused Ion Beam (FIB)

Focused ion beam (FIB) technology can mill material away from a substrate, as well as deposit material onto a substrate to create a specified pattern. In one application, the FIB mills material from a BK7 glass substrate to form a spherical microlens [14]. A liquid gallium source generates the ions. The milling depth at a single location is

controlled by adjusting the beam limiting aperture size, ion dose, dwell time (at that location) and beam current. Rastoring the beam line-by-line mills the microlens from the BK7 substrate. To form a microlens array, each lens has to be formed individually.

Another focused ion beam technique developed by Fu *et al* [14] involves flowing a gaseous material into the vacuum chamber along with the accelerated ion beam to deposit the material onto the substrate, rather than etching material away from the substrate [14]. A gas deposits $SiO_2$ onto the substrate. In FIB deposition, both ion milling of the substrate and deposition of gaseous material take place. If the ion dose is too high, the ions will bombard the substrate and more milling than deposition will take place. If the ion dose is too low, the deposited species will not stick to the substrate. Adjusting the ion dose, beam current and dwell time at each location controls the thickness of deposition.

## Hot Embossing

Focused ion beam technology can also create concave spherical lenses to act as molds for the hot embossing of polycarbonate [15]. Gradually increasing the ion dose of the gallium ion beam toward the center of the lens forms the concave hemispheric lens. Nickel and stainless steel produce molds with pitting holes due to the materials not being homogeneous and to the large grain size of the metals. Silicon provides the mold with the smoothest surface suitable for microlens replication. A sheet of polycarbonate material is placed between a flat nickel backing plate and the silicon concave lens mold. Applying downward pressure and heat, above the glass transition temperature of polycarbonate, hot embosses the polycarbonate into the mold to form the microlens shapes.

Hot embossing of polycarbonate spherical microlenses can also be accomplished by using a silicon mold with circular openings [16]. Photolithographic patterning of photoresist into circular patterns and subsequent reactive ion etching of the silicon substrate, to create the holes, produces the silicon mold. Two heating elements located on the top and bottom of the layer of polycarbonate and silicon mold helps achieve uniform heating of the polycarbonate. Applying heat (above $T_g$ of polycarbonate) and pressure to the silicon mold and polycarbonate produces microlenses posts of various heights with the convex spherical lens at the top.

## Ink-jet

Spherical microlenses can be made by generating spherical droplets of a silica based inorganic-organic material from a nozzle, which land on a substrate and form hemispheres [17]. The drops form in a dust free environment from dispensers with different nozzle diameters. Each drop of the silica based material form one microlens on a glass substrate, which moves in x, y and z coordinates as the nozzle remains stationary. UV radiation curing or oven baking hardens the silica based hemispheres into solid microlenses. Larger microlenses can be formed by incorporating more than one droplet of silica based material into each lens.

## UV Proximity Printing

Spherical microlenses can be fabricated from photoresist by UV proximity printing [18]. Laser writing a series of apertures into plastic produces a plastic photolithography mask. Spinning a negative photoresist on a polycarbonate substrate prepares the plastic

mask and photoresist-coated substrate for exposure in a mask aligner. Instead of utilizing the soft, hard contact or proximity exposure settings of the mask aligner, pieces of glass with different thicknesses are individually placed between the photoresist and the mask to create a quantifiable gap. This gap causes the UV radiation to diffract away from the edge of the circular aperture and slightly expose the photoresist outside the edge of the aperture. The pattern exposed on the photoresist is the intensity distribution of the near field diffraction pattern of the UV radiation traveling from the mask to the substrate through the aperture array. As the distance of the glass gap increases, the diffraction effect is more prominent. When the photoresist is developed after UV exposure, the shape of the photoresist structure that remains on the substrate depends on the intensity distribution at the surface of the photoresist from the diffraction from the circular aperture.

## Deep Lithography with Protons

The bombardment of a PMMA substrate with protons through a mask and subsequent injection of a monomer cause spherical microlenses to form out of the PMMA [19]. A proton beam is projected through a metallic mask with circular apertures onto a PMMA substrate, entering the PMMA and breaking apart some of the polymer chains. This causes the molecular weight of the polymer to decrease down to the penetration depth of the PMMA. The PMMA now contains cylindrical posts of irradiated material. The PMMA sample is put into a vacuum chamber, which is injected with an MMA monomer through a syringe. The injection of the monomer causes the irradiated PMMA to expand

in volume. The volume expansion takes the shape of a hemisphere because of the circular pattern of the irradiated zone at its surface.

## Shadow Mask Deposition

Shadow masked deposition can be accomplished by incorporating holes, slits, meshes and wire grids into a masking layer that rests on a substrate in a deposition system [20]. The material travels through the various apertures and forms a 3-dimensional structure on the substrate depending on the aperture shape and deposition conditions. Both convex and concave microlenses can be produced by this method. Shadow masks can be used to create parabolic microlenses from ZnS, $MgF_2$ and $Na_3AlF_6$ [21]. A pulsed $CO_2$ laser focuses onto the target material, which is mounted on an x-y stage. The deposited species flow from the target through the circular apertures of the shadow mask, which is suspended above the stationary substrate. The deposited materials possess high index contrast for possible enhanced lateral mode confinement in VCSELs. A method for producing non-planar semiconductor layers has been developed by Peake *et al* [22] that uses epitaxial deposition of curved layers of GaAs and AlGaAs via metalorganic chemical vapor deposition (MOCVD) through a shadow mask. These non-planar semiconductor layers could also produce the final layers of a VCSEL's Bragg mirror to enhance the spatial mode properties of the laser.

# CHAPTER IV

# THE MICROLENS PROBLEM

This study was conducted to develop a method of depositing microlenses, consisting of one layer or many layers of dielectric materials, where the thicknesses and curvatures of the microlenses could be controlled. All aspects of microlens formation as well as subsequent device processing steps had to be in accordance with resources available in the AFRL laboratory for optoelectronic device fabrication. The dielectric materials used for deposition of microlenses had to be readily attainable for use in common thin-film deposition systems and have a range of refractive indices. The materials used also had to be able to be integrated into standard processing techniques, such as dry etching for material removal. Finally, the materials had to have good adherence to semiconductor and dielectric substrates for mechanical stability. The deposition methods had to be using systems already present for typical thin-film deposition, since these systems are time and cost-efficient. The shadow mask fabrication technique had to easily accommodate design changes, produce shadow masks that were reusable and be time and cost-efficient.

Methods offering controlled deposition of single and multi-layer dielectric microlenses, that meet all of the previously mentioned requirements, have not been previously demonstrated. The main problem with most of the methods described in Chapter 3 is that they produce hemispheres of only one type of material. The methods

that depend on the surface tension of liquid drops produce only hemispherical microlenses, and do not have the capability to produce lenses with parabolic or cylindrical shapes. The majority of the processes described previously are tailored to produce microlenses from a specific material or group of materials and lack the flexibility to easily switch to another material.

Grayscale lithography involves the variable exposure of photosensitive materials to form monolayer hemispheric shapes after development. This limits the formation of microlenses by this technique to only the materials that are photosensitive. The photosensitive layers are exposed by photomasks, which are written by e-beam technology. This is a very precise, but slow method for producing a photomask. The issue with using photomasks to transfer the hemispherical patterns into the photosensitive materials is that the photomask must be redesigned and re-fabricated using e-beam writing for each set of hemispherical dimensions desired.

Thermal reflow of photoresist produces monolayer hemispheres of photoresist by the surface tension created when photoresist posts are heated above their melting point. This process limits the range of hemisphere materials to photoresists with low melting points. The shape of the microlens is partially controlled by the heating temperature and original photoresist post diameter and thickness. However, this process requires additional processing steps to control the diameter of the microlenses, such as fashioning posts by lithography on which the posts of photoresist are melted to control the lateral flow of the melted material. The microlenses can not be subjected to heating in any of the subsequent processing or testing steps because of the temperature sensitivity of the microlens material.

Forming microlenses with a mold is a fast way to replicate a master array of microlenses for mass production. However, this process is limited to materials that have low melting points or can be suspended into a liquid solution and UV cured. The master microlenses used for producing the mold must be perfectly shaped, or else the replicated microlenses will have the same defects as the masters. A new set of master microlenses must be made and a new mold formed every time a set of hemispherical microlenses with different dimensions is desired. The microlenses that are produced from the mold can only consist of one layer since the molded material is liquid during replication. Finally, the replicated microlenses require a controlled pressing system that must incorporate either heat or UV exposure to properly form the microlenses, which is not a standard process in semiconductor device fabrication. Hot embossing of polycarbonate materials possesses similar drawbacks to those described for using molds to replicate microlenses for mass production.

Thermal reflow of photoresist followed by a dry etch to transfer the photoresist pattern into the substrate produces microlenses from the monolayer or multi-layer substrate. Usually, the substrate consists of a monolayer of semiconductor or dielectric material that forms monolayer microlenses. This process limits the substrate material only to the materials that can be etched using dry-etch chemistries. The master photoresist microlenses may not always have ideal hemispherical shapes, which would result in the defects being etched into the substrate. The biggest issue with forming microlenses with this method is that photoresist and most substrates used for dry-etching have different rates of material removal. This would result in the microlenses etched from the substrate having a different shape than the photoresist master.

Using selective wet etching to etch a microlens from a substrate requires a different wet chemistry for each different substrate material. It is limited only to the materials for which a wet etch chemistry exists. Similar to the thermal reflow and dry etch processes, the microlenses formed from this process will consist of the same layers of material that the substrate possesses, but generally they are monolayer substrates. This process requires preliminary photolithography and dry etching to produce holes in the substrate into which the microlenses will be etched. This presents a problem in future processing steps if the lens needs to be free-standing on top of the substrate. The wet etch may also be selective to specific crystal geometries, etching the substrate more in certain crystal planes and not etching in other crystal planes.

A focused ion beam (FIB) can be used to etch material away from a substrate or deposit material onto a substrate. Similar to the wet and dry etch techniques, when etching into a substrate, it can consist of multiple layers, but most are monolayers to ensure uniform etch rates and microlens profiles. Deposition multi-layers of material onto a substrate can be done, but is difficult due to programming the FIB to dwell in the same location for different amounts of time to account for different material deposition rates. The FIB source depletes with many hours of use, causing ion beam strength to fluctuate over time. This may change the deposition and etch rates, resulting in non-uniform microlenses.

Microlenses can be produced by spraying liquid droplets of microlens material onto a substrate, forming a monolayer hemisphere on the substrate due to surface tension. This method limits the possible microlens materials to those that can be suspended into a liquid solution at room temperature, and then baked or UV cured to harden them into

solid microlenses. The hole diameter of the nozzle from which the droplets are ejected affect the diameter and thickness of the microlens, meaning that several nozzles would have to be used to create microlenses with a large range of dimensions.

UV proximity printing of microlenses utilizes photosensitive materials and a photomask to create hemispherical microlens patterns from the resist. This process is limited only to photosensitive materials for the production of monolayer photoresist microlenses. Similar to grayscale lithography, the UV proximity technique uses a photomask generated by laser writing holes of different diameters into the photomask material. This process would have to be repeated for every new set of hole diameters desired for the production of microlenses with different dimensions. Using deep lithography with protons to create microlenses possesses drawbacks similar to the UV proximity printing technique, because it limits the microlens material to polymers and a metallic mask has to be remade every time a new set of microlenses with different dimensions needs to be produced.

The shadow mask methodology has been used to create microlenses and multi-layered curved surfaces for a variety of applications. The materials chosen in this study include $SiO_2$ and $SiN_x$ because they are easily attainable and have known behaviors under standard processing techniques, such as wet and dry etching. The materials described by Cusumano *et al* [21] for multi-layer microlens formation include ZnS, $MgF_2$ and $Na_3AlF_6$, which are not common materials used in device processing. Peake *et al* [22] use semiconductor materials to consecutively deposit curved layers. Semiconductor materials require a reactor for deposition with either metalorganic chemical vapor deposition (MOCVD) or molecular beam epitaxy (MBE). Semiconductor material deposition

presents problems for the affordable and simple deposition of single or multi-layered curved surfaces.

Using a shadow mask to deposit dielectric microlenses has many advantages compared to the other techniques described above and in Chapter 3. Depositing dielectric materials with sputtering and PECVD is preferable to other methods because they are typical pieces of equipment used in laboratories that perform thin-film deposition. PECVD and sputtering are also less expensive and labor-intensive than growing semiconductor materials with molecular beam epitaxy (MBE) and metalorganic chemical vapor deposition (MOCVD). Using sputtering and PECVD for deposition of dielectrics allows for a wide range of materials to be used. Some examples of dielectric materials that could be used for microlens formation include $SiO_2$, $SiN_x$ and $TiO_2$, which have refractive indices of about 1.5, 2.0 and 2.5, respectively. These dielectric materials have very good adhesion to a variety of substrates to prevent dislocation of the microlenses due to mechanical stress. The materials are also completely compatible with common semiconductor device processing techniques, including wet and dry etching and photolithography. This makes it easy to remove and re-deposit the dielectric layers if error in deposition occurs, which is not always possible with deposition of semiconductor materials.

Advantages of using a shadow mask to deposit the dielectric microlenses include the consecutive growth of curved Bragg layers of alternating dielectric materials. The deposition of different dielectric materials in the same microlens can be accomplished by simply changing the target material for sputtering or the gas chemistry for PECVD. Constructing the shadow mask by laser micromachining allows the mask to be made

from a variety of materials. Metallic and electrically insulating shadow masks can successfully be made using this technique. Since the mask is made from robust materials such as nickel and alumina, it can withstand wet etching procedures that allow it to be cleaned and reused for many depositions. The laser used for machining the shadow mask can be programmed to mill shadow mask cavities with many different geometries into each shadow mask array, allowing a complete cavity geometry study to be conducted in one deposition with the shadow mask array. The cavity geometries can be tailored to produce microlenses with different thickness and curvatures.

Microlenses produced by shadow masked deposition of dielectrics have many applications in optoelectronics and micro-optics. For example, a focal plane array of dielectric microlenses can be produced in one deposition by using a shadow mask array to deposit dielectric material onto a transparent substrate. In optoelectronics, a high refractive index dielectric microlens deposited onto the emitting surface of an LED can improve the extraction efficiency and output power of the device. An analogous technique can also be used to enhance the extraction of resonant-cavity LEDs (RC-LEDs). Similarly, a possible method for enhancing the transverse mode discrimination in vertical cavity surface emitting lasers (VCSELs) utilizes curved rather than planar top Bragg mirror layers [23].

# CHAPTER V

# SHADOW MASK DEVELOPMENT

## Shadow Mask Design

The shadow mask design consists of a circularly symmetric cavity beneath an overhang containing a circular hole in the center. A schematic cross-section of a shadow mask is depicted in Figure 5.1. The mask is mechanically attached to the substrate and held in place during deposition. Deposition inside the cavity occurs through a combination of ballistic and diffusive transport of the reactive species, forming a non-planar, non-faceted microlens structure.

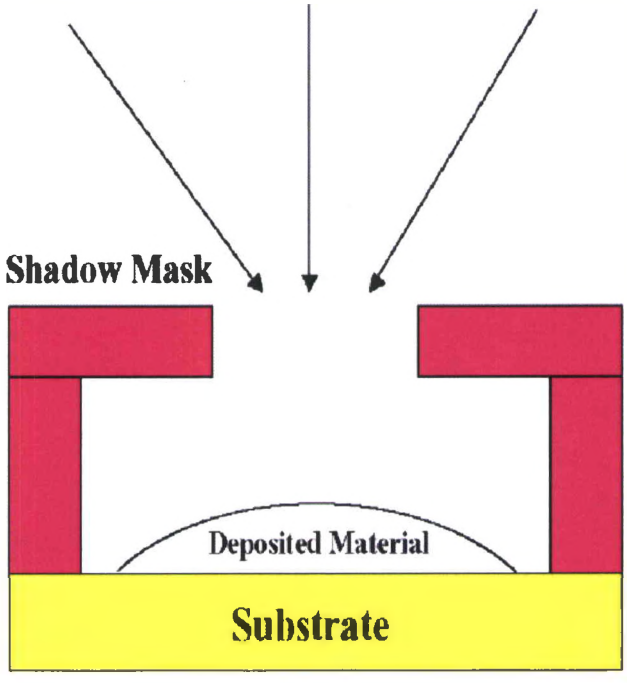


**Figure 5.1** Cross-section of the circularly symmetric shadow mask cavity

Due to the relatively large geometries in the design, we used laser micromachining to fabricate the mask [24]. For smaller geometries, deep reactive-ion etching (RIE) could be used, although this process would limit the number of materials that could be used for fabricating the mask. Since the electrical conductivity, dielectric constant and thermal conductivity of the shadow mask may play an important role in the deposition conditions, we chose two very different mask materials. Alumina and nickel were selected because they represent materials that are electrically insulating and electrically conducting, respectively. Pictures of the alumina and nickel shadow masks are shown in Figure 5.2. Attempts were also made to produce a conductive shadow mask from stainless steel, aluminum and SiC. Only nickel and alumina withstood the laser micromachining without cracking, and they provided cavity depths that were accurate to suitable deposition tolerances, as detailed later.

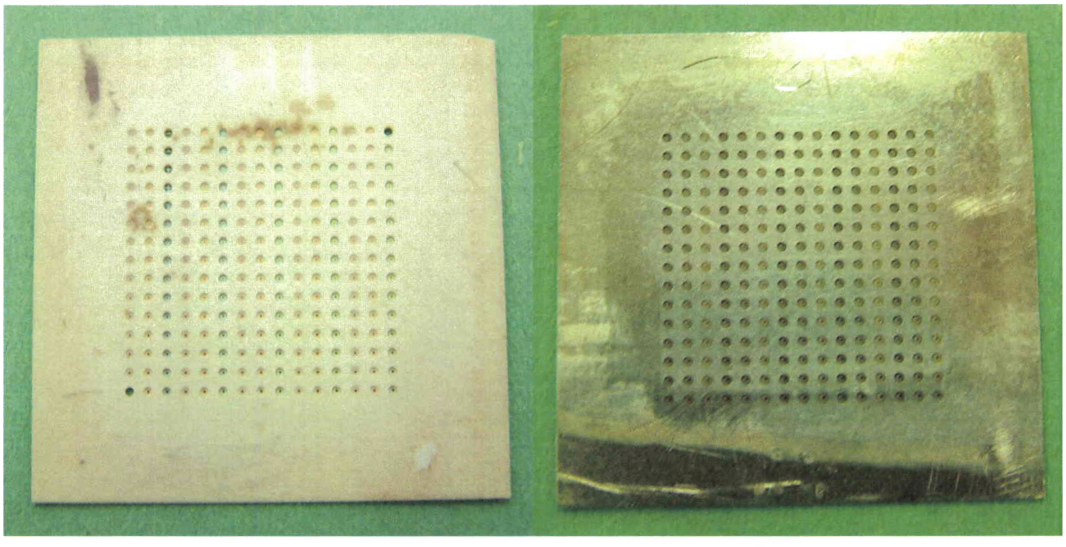

**Figure 5.2** Images of the alumina (left) and nickel (right) shadow mask arrays

The geometric parameters that were varied within the shadow mask design are shown in Figure 5.3. Each array consisted of a 25.4mm square piece of alumina or nickel with a thickness of 250μm. Within each piece of alumina and nickel, there was an array of 225 circular shadow mask cavities. An SEM (scanning electron microscope) image, taken with a FEI DualBeam Strata 235, of the top view of the nickel shadow mask is shown in Figure 5.4. Each cavity had a different combination of circular top hole diameter, spacer layer thickness and mask layer thickness. The diameter of the shadow mask cavities was held constant throughout the array at 500μm, which is denoted in Figure 5.3 as $d_1$. The spacer layer thickness is the height of the shadow mask cavity and is represented as $h_1$. The mask layer thickness, or $h_2$, is the thickness of the overhang layer. After assigning $h_1$ and $h_2$ for a specific shadow mask cavity, the remaining parameter $h_3$ is then fixed and given by the relation $h_3 = substrate\ thickness - h_1 - h_2$. The diameter of the circular opening in the mask layer ($d_2$) was varied in increments of 10μm, from 10μm to 150μm. Table 5.1 shows the range of values of $h_1$ and $h_2$ for the alumina and nickel shadow masks.

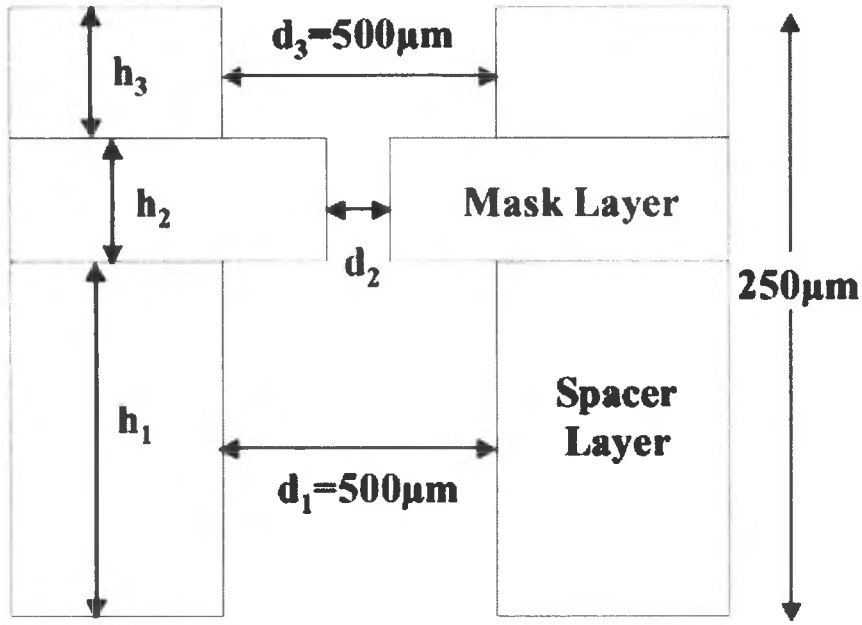


**Figure 5.3** Shadow mask cross-section detailing the key geometric parameters influencing curved layer deposition. The mask design is circularly symmetric about the center of the top hole of the cavity, or $d_2$.

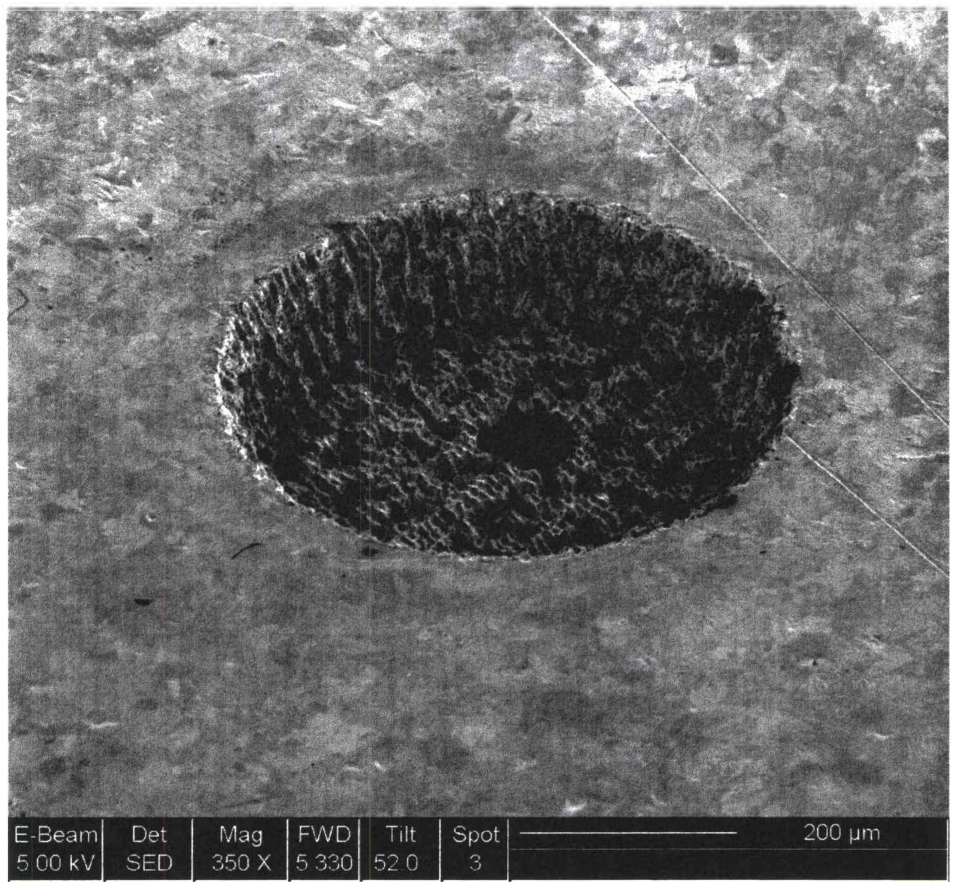


**Figure 5.4** A bottom view of a laser micromachined nickel shadow mask cavity taken by SEM. The diameter of the circularly symmetric cavity is $d_1$, the diameter of the hole in the center of the cavity is $d_2$ and the steep sidewall of the cavity is $h_1$.

**Table 5.1** Mask and spacer layer thickness values for alumina and nickel

| Parameter | Alumina | Nickel |
|---|---|---|
| $h_1$ ($\mu$m) | 79-203 | 45-109 |
| $h_2$ ($\mu$m) | 22-101 | 98-128 |

## Deposition Methods

Three techniques were used to deposit non-planar layers with the alumina and nickel shadow masks. RF-sputtering was used to create ballistic deposition from a $SiO_2$ target through the circular shadow mask aperture and onto a silicon substrate. The shadow mask is secured to the silicon substrate by pins anchored to an aluminum holder. An image of the shadow mask, silicon substrate and aluminum holder is shown in Figure 5.5. The holder is placed in the center of the rotating platen inside the sputtering chamber so that the shadow masked substrate is in the approximate center of rotation. Reactive RF-sputtering of $SiN_x$ was deposited using Ar-$N_2$ plasma gases and a Si target. This deposition method also utilized the rotating platen, which in turn rotated the holder, substrate and shadow mask setup. Both sputtering methods were conducted at room temperature with a Denton Discovery 18 system.

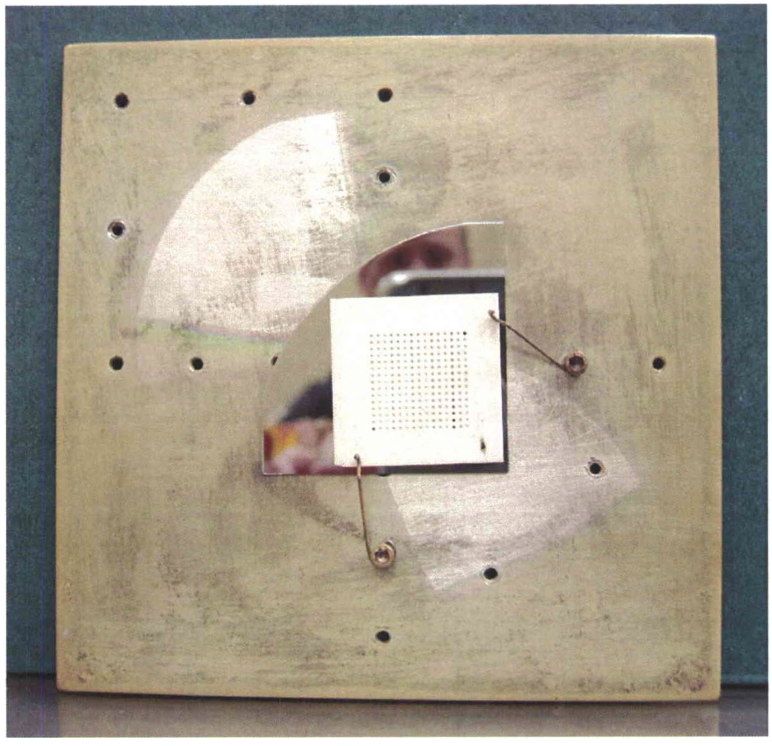

**Figure 5.5** Image of the aluminum holder setup, which has pins that secure the shadow mask and silicon substrate to the holder.

PECVD was used to produce non-planar layers of $SiO_2$ by depositing through the shadow mask to the substrate, which is anchored to the aluminum holder and placed on a stationary platen in the PECVD chamber. The PECVD was conducted with a Plasmatherm (Unaxis) 790 tool at a temperature of 300C. The deposition of $SiO_2$ by PECVD utilized silane ($SiH_4$) diluted in helium (5% $SiH_4$ in He) and a large excess of nitrous oxide ($N_2O$) as process gases. In this deposition, the shadow mask was anchored to the substrate by means of the aluminum holder plate assembly shown in Figure 5.5. The entire assembly was placed near the center of the deposition chamber. The PECVD tool routinely deposits material onto sample substrates with $< \pm$ 2% thickness variation

across the 11-inch platen. The shadow mask assembly, therefore, occupies a small region within this space.

## Characterization of the Non-planar Layers

The non-planar layers deposited by sputtering and PECVD were analyzed to determine their relative curvatures and the rates of deposition through the alumina and nickel shadow masks for each method. The shadow mask deposited layers were measured with a Tencor P10 stylus profilometer and a Zygo New View 5000 white light interferometer. At first, the interferometer produced images of the non-planar layers that were inverted in the center. Figure 5.6 shows a Zygo image illustrating this phenomenon. The non-planar dielectric layers were transparent at the point of maximum thickness; therefore, the light reaching the interferometer was reflecting off of the substrate at the center of the layer, causing that part of the image to appear concave. The non-planar layers were then coated with a very thin layer (~300Å) of Au by the Denton Discovery 18 sputtering system to create a reflecting surface on top of the dielectric layer. A Zygo image of a gold-coated non-planar layer is shown in Figure 5.7. The layer of Au was thick enough to make the surface of the dielectric reflective, yet it did not change the thickness profile of the non-planar layer. A comparison of three non-planar layers that were measured by profilometer, then coated with Au and again measured with the profilometer and Zygo shows that the curvature does not change significantly with Au coating or measurement technique. The data from this comparison is presented in Appendix A.

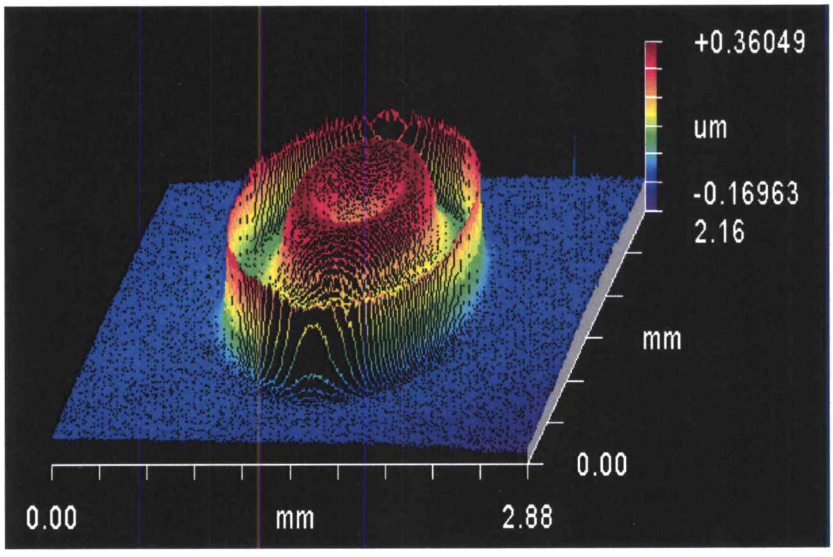


**Figure 5.6** Zygo image of a non-planar dielectric layer, which is transparent to white light in the center of maximum thickness.

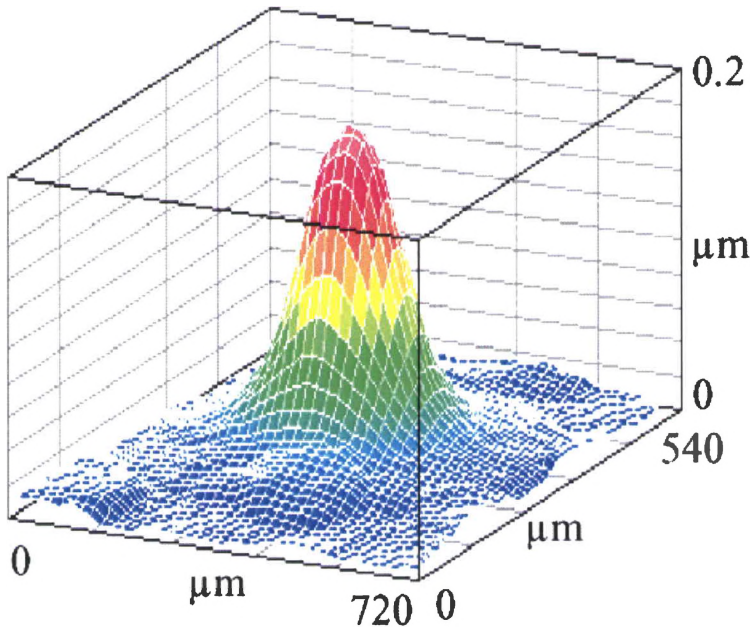


**Figure 5.7** Zygo image of Au-coated non-planar dielectric layer

Two-dimensional interferometer profile data was collected through the center of the curvature, which was the position of maximum thickness, of the non-planar layers. Similarly, single line scans were taken with the profilometer over the center of each non-planar layer to produce a 2D profile. All of the 2D profiles were then fit to the following parabolic equation:

$$t = t_o\left[1-\left(\frac{r}{r_o}\right)^2\right].$$

Here $t$ is the thickness of the layer along the radial direction, $t_o$ is the thickness at the center of the curvature and $r_o$ is half the width of the lineshape (i.e. where the lineshape crosses the radial axis at $t = 0$). Figure 5.8 shows an example of a non-planar layer fit to this equation and the extracted values of $t_o$ and $r_o$. Each non-planar layer was individually fit to the parabolic curve equation within $r = \pm$ 50μm about the center of the peak. In this range of interest, the parabolic fit given by the above equation described the profile of the non-planar layer more accurately than a spherical lineshape. Hence, we conclude that the shadow mask method produces aspherical microlenses. *Note that if $r_o$ is small, the base of the parabola will be narrower and the non-planar layer will have more curvature. If $r_o$ is large, the microlens will have less curvature.*

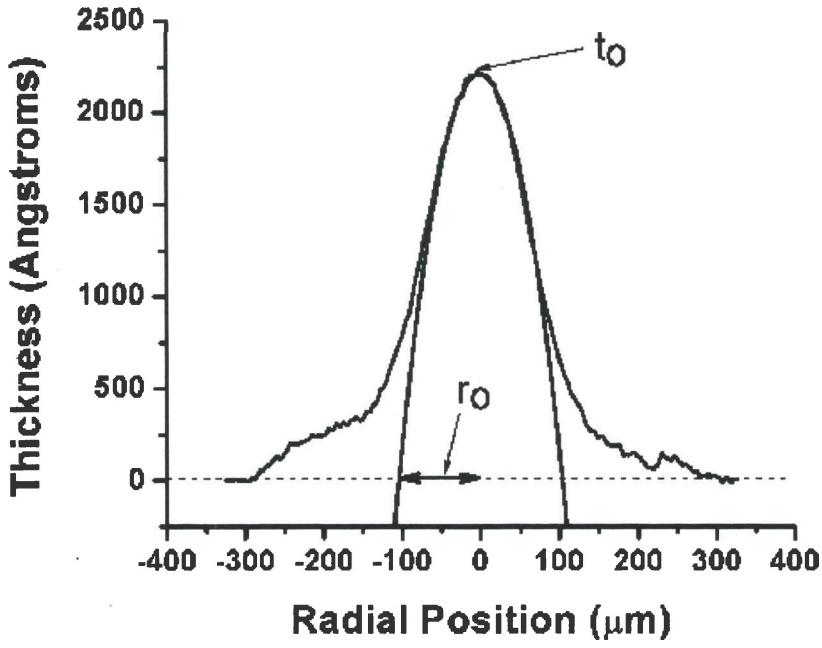


**Figure 5.8** 2D profile and parabolic fit of non-planar layer. The values of the parameters extracted from the fit are $t_o$ = 2210.6Å and $r_o$ = 104.0μm.

Results of Shadow Mask Geometry

Clear relationships between shadow mask geometry, microlens curvature and cavity deposition rate were observed. This data is presented in Appendix A. As the top hole diameter ($d_2$ in Figure 5.3) was increased, with all other parameters held constant, $r_o$ was found to increase. Therefore, the curvature of the microlenses, within the range of interest of $r = \pm$ 50μm surrounding the center of the peak, decreased as $d_2$ was increased. An example of this trend is $SiO_2$ RF-sputtered for 87 minutes through the alumina shadow mask, as shown in Figure 5.9. *For LED or laser applications where curvature is the most important characteristic of the microlens, the top hole diameter ($d_2$) of the shadow mask cavity should be made as small as possible.*

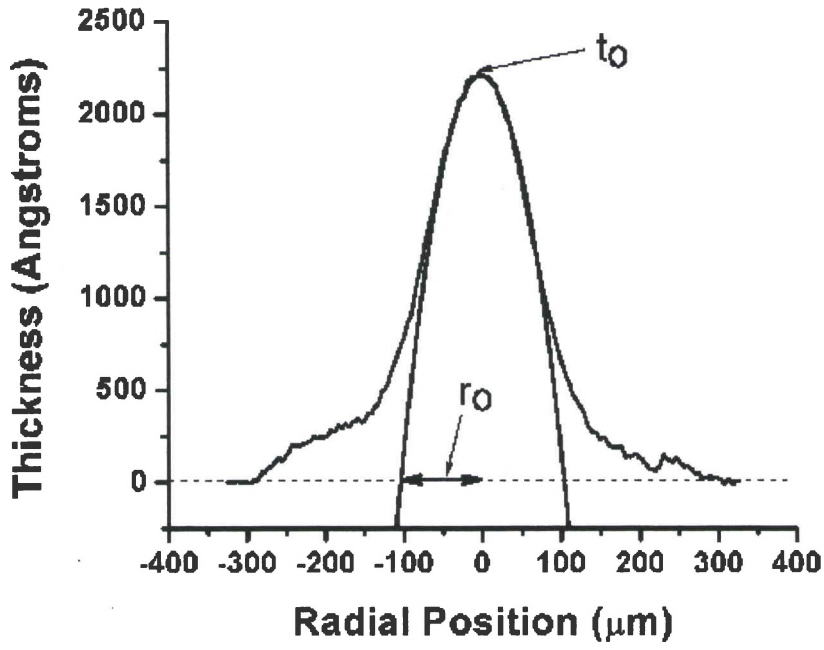


**Figure 5.8** 2D profile and parabolic fit of non-planar layer. The values of the parameters extracted from the fit are $t_o$ = 2210.6Å and $r_o$ = 104.0μm.

Results of Shadow Mask Geometry

Clear relationships between shadow mask geometry, microlens curvature and cavity deposition rate were observed. This data is presented in Appendix A. As the top hole diameter ($d_2$ in Figure 5.3) was increased, with all other parameters held constant, $r_o$ was found to increase. Therefore, the curvature of the microlenses, within the range of interest of $r = \pm$ 50μm surrounding the center of the peak, decreased as $d_2$ was increased. An example of this trend is $SiO_2$ RF-sputtered for 87 minutes through the alumina shadow mask, as shown in Figure 5.9. *For LED or laser applications where curvature is the most important characteristic of the microlens, the top hole diameter ($d_2$) of the shadow mask cavity should be made as small as possible.*

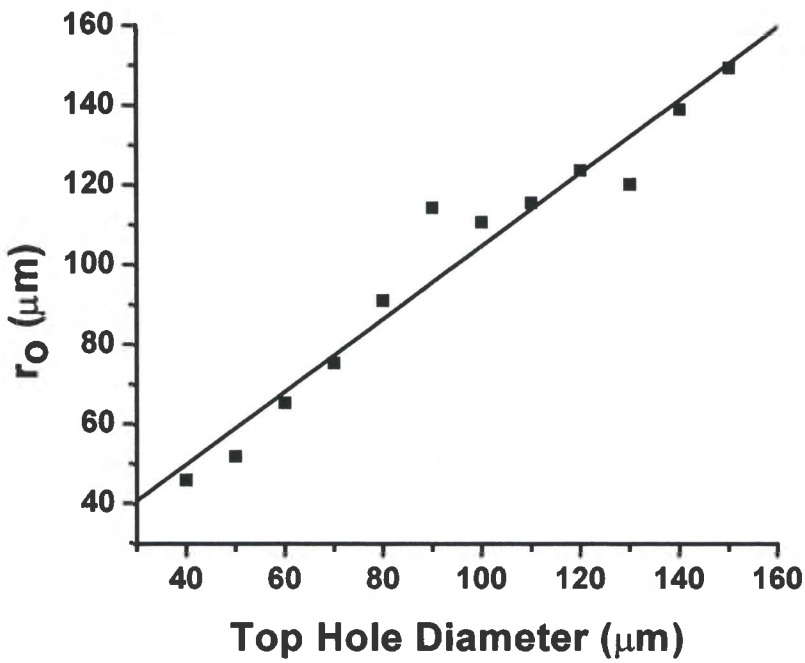


**Figure 5.9** $r_o$ vs. $d_2$ for $SiO_2$ RF-sputtered for 87 minutes through the alumina shadow mask with fixed mask parameters $h_1$ = 79μm and $h_2$ = 96μm.

The relationship between the top hole diameter ($d_2$) and curvature is due to the "shadowing" effect of the mask layer, which is controlled by changing the ratio of $d_2$ to the cavity diameter ($d_1$). The diameter of the limiting aperture ($d_2$) affects the extent to which the mask layer extends over the cavity, thus altering the path of the material flowing into the cavity. When $d_2$ is smallest, the mask layer covers more of the cavity, thus "focusing" the material directly under the top hole and creating microlenses with the most curvature. When $d_2$ is larger, the shadowing effect diminishes, allowing the material to travel to the substrate unimpeded by the mask layer, resulting in flatter layers.

The rate of deposition inside the cavity was measured by dividing the thickness at the peak of the microlens by the deposition time. The amount of material that flows inside

the cavity is limited by the opening $d_2$. This caused the rate of deposition inside the cavity to increase as $d_2$ was increased, while the mask and spacer layer thicknesses were held constant. An analogous example of this trend was the increase in the thickness of the material deposited inside the cavity compared to the thickness on the bare substrate, or percent deposited inside the cavity, when $d_2$ was increased. Figure 5.10 shows this dependence for a 30 minute deposition of $SiO_2$ by PECVD through the nickel shadow mask. It is apparent from Figure 5.10 that below top hole diameters of 70$\mu$m, the cavity deposition rate and percent deposited inside the cavity were too small to detect any recognizable deposition on the substrate below the cavities. For $d_2$ below 40$\mu$m, no deposited material was thick enough to be measured for each of the deposition methods performed for times ranging from 30 to 87 minutes. Figures 5.9 and 5.10 illustrate the tradeoff between curvature and deposition rate. *While a small $d_2$ will give the maximum curvature, it is achieved at the expense of a slower deposition rate.*

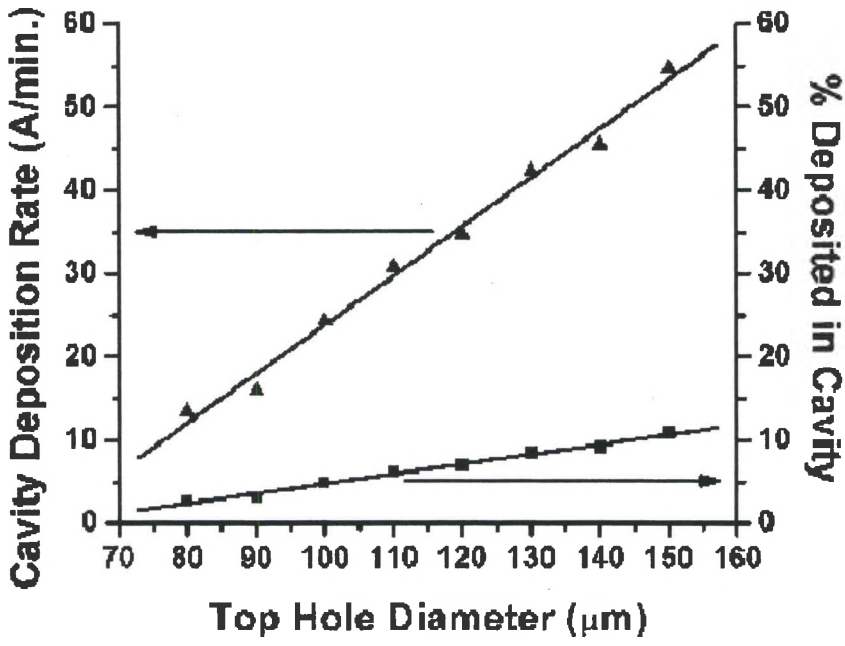


**Figure 5.10** Cavity deposition rate (triangles) and % deposited inside the cavity (squares) vs. $d_2$ for a 30 minute deposition of $SiO_2$ by PECVD through the nickel shadow mask with fixed mask parameters $h_1$ = 49μm and $h_2$ = 106μm.

Changes in the height of the cavity, or the spacer layer thickness ($h_1$ in Figure 5.3), also had an important effect on the curvature of the microlenses and the cavity deposition rates. In this comparison, the top hole diameter ($d_2$) and mask layer thickness ($h_2$) were held constant as the spacer layer thickness ($h_1$) was increased. The overall volume inside the cavity was increased while the same amount of material was allowed to enter the cavity. As $h_1$ was increased, $r_o$ also increased, which allowed the deposited species more vertical distance to diffuse out toward the edge of the circular cavity. This caused the deposited material to be spread more evenly over the substrate, thus decreasing the curvature of the microlens. Figure 5.11 shows this trend exemplified by a 30 minute deposition of $SiO_2$ by PECVD through the alumina shadow mask. When $h_1$ was

increased, the deposition rate inside the cavity was found to decrease. If the lateral diffusion of the material extended as the cavity height was increased, the maximum thickness of the microlens would be less than that for a microlens formed in a cavity with a smaller $h_1$. The same idea can be applied to the percent of material deposited inside the cavity compared to the thickness on the bare substrate. Figure 5.12 illustrates this dependence with the case of $SiN_x$ reactive RF-sputtered for 68 minutes through the nickel shadow mask. *To create microlenses with the most curvature, highest cavity deposition rate and highest percent deposited inside the cavity, the height of the shadow mask cavity ($h_1$) should be decreased.*

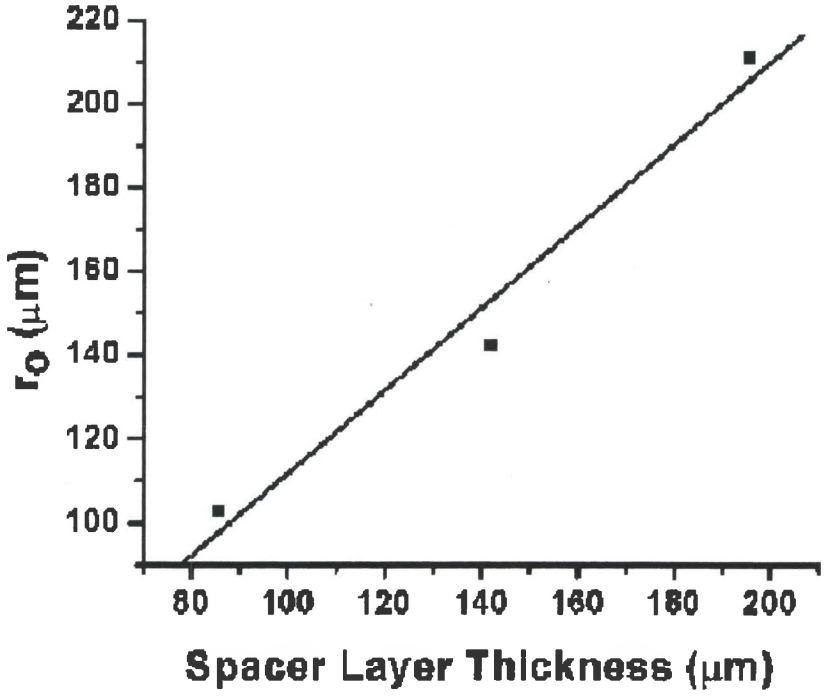


**Figure 5.11** $r_o$ vs. $h_1$ for a 30 minute deposition of $SiO_2$ by PECVD through the alumina shadow mask with fixed mask parameters $d_2$ = 140μm and $h_2$ = 33μm.

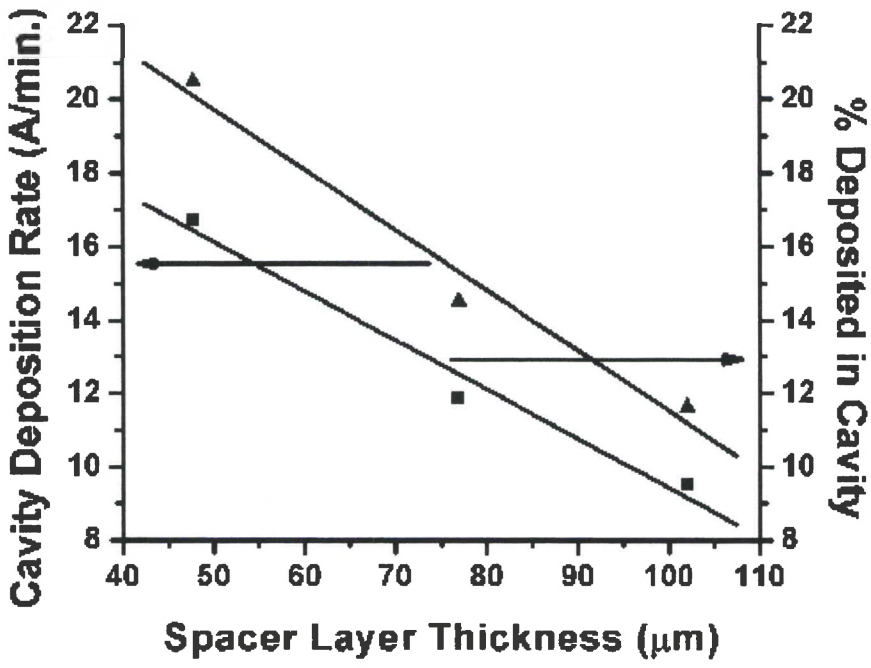


**Figure 5.12** Cavity deposition rate (triangles) and % deposited inside the cavity (squares) vs. $h_1$ for a 68 minute deposition of $SiN_x$ reactive RF-sputtered through the nickel shadow mask with fixed mask parameters $d_2$ = 140μm and $h_2$ = 105μm.

Results of Alumina vs. Nickel Shadow Masks

To compare the microlenses deposited through the alumina and nickel shadow masks by the three deposition methods directly, the shadow masks were fabricated with cavities having similar geometrical parameters. Table 5.2 shows the values for the dimensions of the alumina and nickel shadow mask cavities that were used for comparison. The geometries are essentially the same except for a 9μm difference between the mask layer thicknesses ($h_2$) of the alumina and nickel shadow masks. The small deviation in $h_2$ did not have an effect on the microlens curvature, cavity deposition rate or percent deposited inside the cavity. This conclusion is based on measurements in which no consistent patterns in microlens curvature, cavity deposition rate or percent deposited inside the

cavity were observed from microlenses formed by shadow mask cavities with variations in $h_2$ (while $d_2$ and $h_1$ were held constant).

**Table 5.2** $d_2$, $h_1$ and $h_2$ values of similar nickel and alumina shadow mask cavities

| Parameter | Alumina | Nickel |
|---|---|---|
| $d_2$ ($\mu$m) | 150 | 150 |
| $h_1$ ($\mu$m) | 79 | 77 |
| $h_2$ ($\mu$m) | 96 | 105 |

Microlenses produced by cavities with corresponding geometries were analyzed for differences in curvature, cavity deposition rate and percent deposited inside the cavity caused by changing the shadow mask material from alumina (dielectric) to nickel (conductor). All other deposition parameters, such as temperature, pressure, material species and deposition times, were kept constant. The data presented in Table 5.3 shows that, for each deposition method, the $r_o$ values were smaller for the microlenses produced by the alumina shadow mask than the nickel shadow mask. Also, the cavity deposition rate and percent deposited inside the cavity were greater for the microlenses produced by the alumina shadow mask than the nickel shadow mask. These differences could be caused by changes in the temperature gradient, plasma density, sticking coefficient and electric field in the vicinity of the shadow mask cavity, which could affect the material flux and surface diffusion of the deposited material.

**Table 5.3** $r_o$, cavity deposition rate and % deposited inside the cavity for matching alumina and nickel shadow mask cavities

| Measured/Fit Parameter | Method/ Material | Alumina | Nickel |
|---|---|---|---|
| | | | |
| $r_o$ | PECVD/ | 120 | 137 |
| ($\mu$m) | $SiO_2$ | | |
| | RF Sputter/ | 139 | 197 |
| | $SiO_2$ | | |
| | Reactive RF Sputter/ | 147 | 175 |
| | SiNx | | |
| | | | |
| Cavity | PECVD/ | 44 | 22 |
| Deposition | $SiO_2$ | | |
| Rate | RF Sputter/ | 16 | 10 |
| (A/min.) | $SiO_2$ | | |
| | Reactive RF Sputter/ | 25 | 13 |
| | SiNx | | |
| | | | |
| % Deposited | PECVD/ | 9 | 4 |
| In Cavity | $SiO_2$ | | |
| | RF Sputter/ | 23 | 15 |
| | $SiO_2$ | | |
| | Reactive RF Sputter/ | 20 | 10 |
| | SiNx | | |

The data presented in Table 5.3 shows that, for PECVD of $SiO_2$, the $r_o$ values were smaller for the microlenses produced by the alumina shadow mask than the nickel shadow mask. The alumina shadow mask cavity with geometrical parameters that matched the nickel produced microlenses with more curvature. To investigate this in more detail, a numerical simulation was performed to calculate the DC electric field in a two-electrode deposition chamber, similar to the PECVD system, with an alumina or nickel shadow mask placed on the substrate and the bottom electrode [25]. An illustration of the PECVD chamber and shadow mask setup used in the simulation is shown in Figure 5.13. The substrate consisted of

a layer of silicon and the metal electrodes were two plates of aluminum. The values for the density, conductivity and relative permittivity of each material utilized in the simulation are shown in Table 5.4.

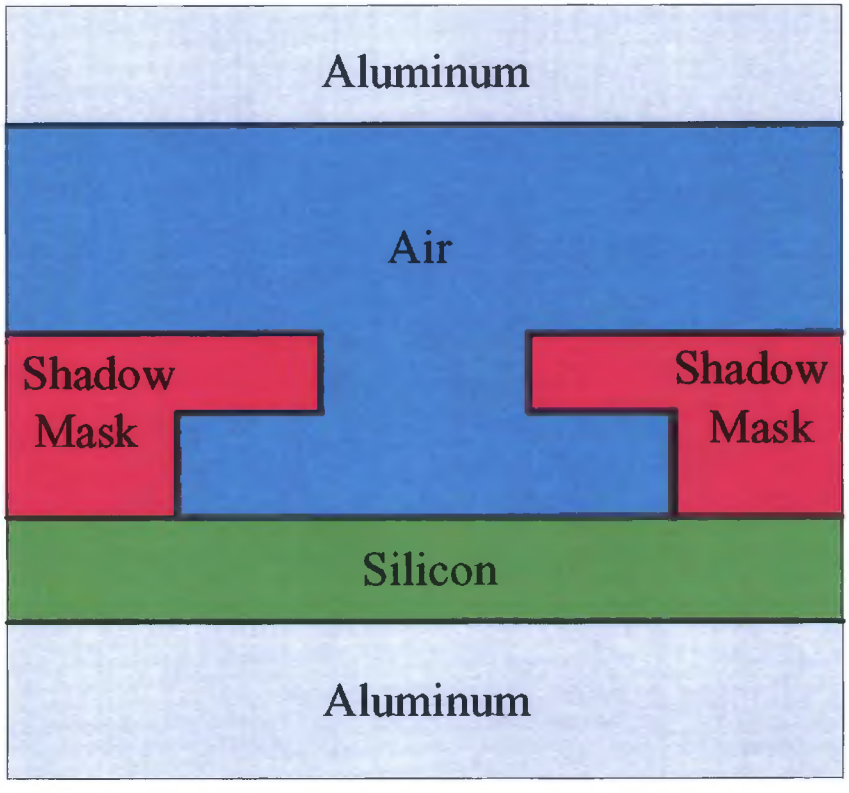


**Figure 5.13** PECVD chamber setup for simulation

**Table 5.4** Material parameters for numerical simulation

| Material | Density kg/(m^3) | Conductivity 1/(ohm*m) | Relative Permittivity |
|---|---|---|---|
| | | | |
| Aluminum | 2700 | 3.77E+07 | 1 |
| Silicon | 2329 | 3.13E-04 | 11.7 |
| Air | 1.614 | 1.00E-04 | 1 |
| Alumina | 3690 | 1.00E-12 | 9.6 |
| Nickel | 8908 | 1.46E+07 | 1 |

Figure 5.14(a) shows the simulated electric field (direction and magnitude) within an alumina shadow mask in the PECVD chamber. Figure 5.14(b) shows the same simulation with a nickel shadow mask. The field arrows in Figure 14 are not indicative of the simulated electric field strength (the field strength is color-coded); they are all unit length to illustrate only the field direction. It can be seen that, in the simulation, the electric field within the alumina shadow mask travels straight down through the top hole of the cavity to the surface of the substrate, except next to the vertical walls of the mask layer. In contrast, the electric field within the nickel shadow mask immediately diverges away from the center of the hole of the cavity toward the walls of the mask layer and travels further underneath the overhang of the mask layer to the substrate. If one views the electric field lines inside the shadow mask cavities as possible indicators of the material flux, then the deposition of material would concentrate directly under the top hole of the alumina shadow mask cavity, while the nickel shadow mask deposition would be spread out underneath the overhang of the mask layer. The nickel shadow mask microlenses would have less curvature than those produced by the alumina. The experimental data for PECVD of $SiO_2$ presented earlier supports this theory, however, the simulation does not take into account all of the factors that effect the deposition. The simulation does not explain the similar pattern of results also found for RF-sputtering of $SiO_2$ and reactive RF-sputtering of $SiN_x$.

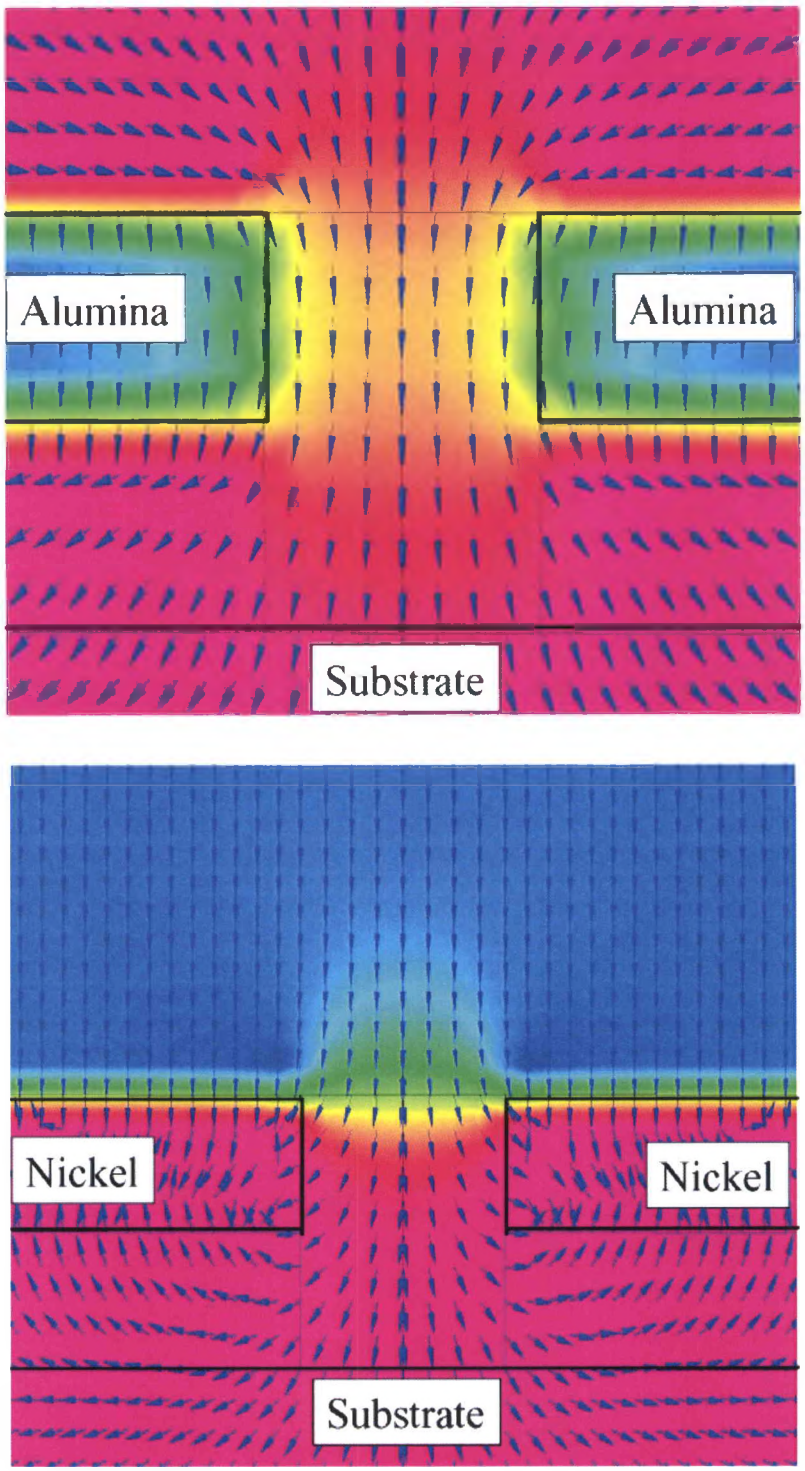


**Figure 5.14** Simulated electric field distribution using (a) the alumina shadow mask and (b) the nickel shadow mask

The deposition rate inside the cavity and percent deposited inside the cavity is greater for the alumina mask than the nickel shadow mask for PECVD of $SiO_2$. Table 5.3 shows the comparison between these parameters for the alumina and nickel shadow masks. Figures 5.15(a) and 5.15(b) show the result of the simulation depicted in Figures 5.14(a) and 5.14(b) on the same color-coded scale, but they have been modified to show the electric field strength contour lines of the dielectric and conducting shadow masks instead of the electric field direction. In the simulation, the electric field is concentrated within the alumina shadow mask, with the contour lines stretching from the top hole of the cavity up toward the top electrode of the PECVD chamber and down to the substrate. In contrast, the majority of the field strength surrounding the nickel shadow mask is concentrated in the air between the top surface of the nickel shadow mask and the top electrode of the deposition system. The field strength contour lines do not stretch from the top hole of the cavity to the substrate. If the electric field strength in the proximity of the shadow mask cavity from its circular aperture to the substrate is a possible indicator of the amount of material that can travel into the cavity and onto the substrate, the smaller electric field strength of the nickel shadow mask in this vicinity would allow less material into the cavity and less deposition onto the substrate. This would result in lower cavity deposition rates and less percentage of $SiO_2$ deposited by PECVD inside the cavity for the nickel shadow mask than alumina. The results presented in Table 3 follow this conclusion, but again, the simulation is not complete because it does not include many factors that effect the deposition. Therefore, this theory can not be considered the definitive explanation for the trends apparent from the data for PECVD of $SiO_2$.

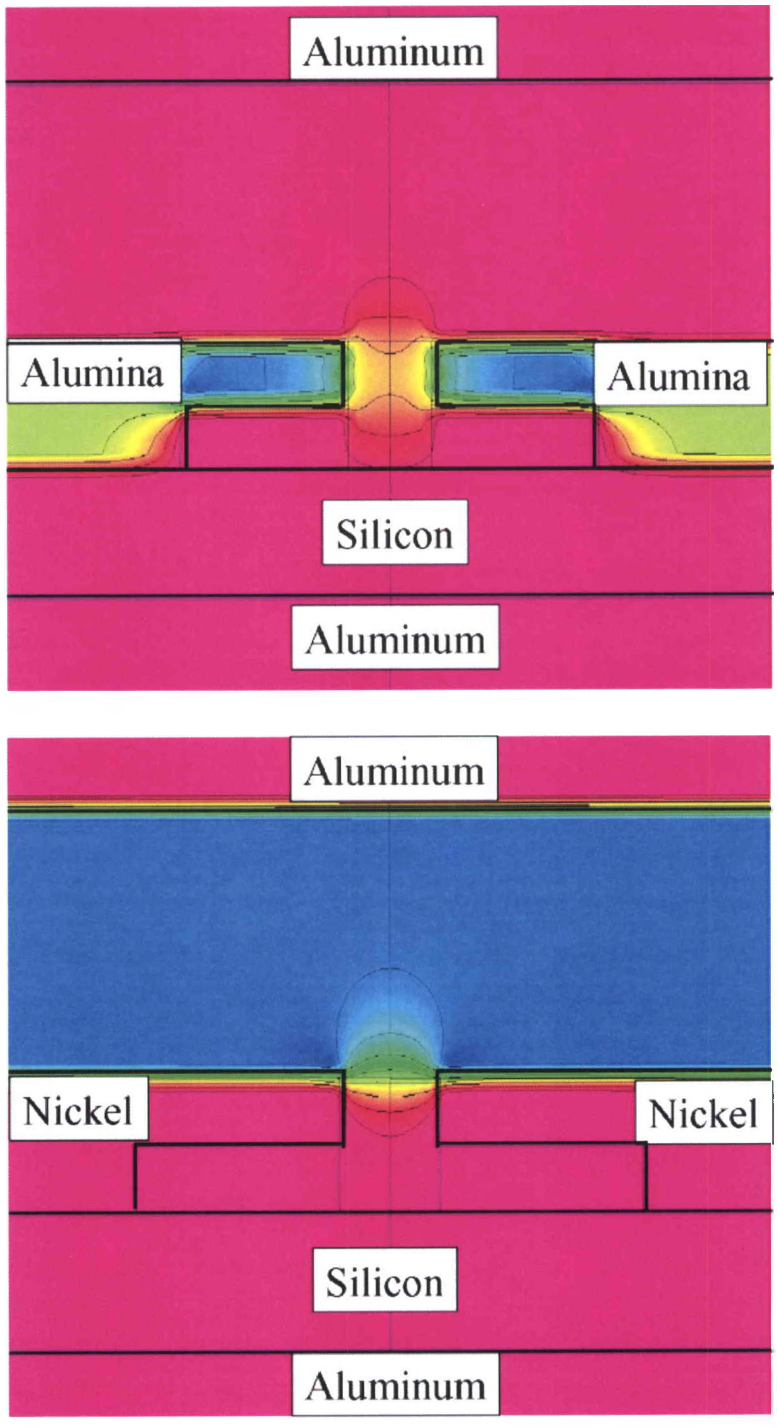


**Figure 5.15** Electric field contour lines using (a) the alumina shadow mask and (b) the nickel shadow mask

## Results of Deposition Method

Data was collected from the microlenses produced from the alumina and nickel shadow masks with similar cavity geometries by depositing $SiO_2$ via PECVD or RF-sputtering, and $SiN_x$ by reactive RF-sputtering. The three deposition methods were compared based on which methods produced microlenses with the most curvature and the highest percent of material deposited inside the cavity. The percent deposited inside the cavity compared to deposition on a bare substrate was considered to determine which method consumed the least amount of target material and process gases. These qualities would create an aspheric microlens with more refractive power that could be deposited efficiently. Table 5.3 shows the values for $r_o$, deposition rate inside the cavity and percent deposited inside the cavity for microlenses formed by the matching shadow mask cavities of alumina and nickel. For both alumina and nickel shadow masks, $SiO_2$ microlenses formed by PECVD had the lowest $r_o$ values, thus the most curvature. Therefore, for producing aspheric microlenses with the most curvature, the best choice would be PECVD of $SiO_2$. Figure 5.16 is the experimental data that shows the relationship between curvature and deposition method for microlenses produced by both alumina and nickel shadow masks. The deposition method with the highest percent of material deposited inside the shadow mask cavity was RF-sputtered $SiO_2$, and the lowest was PECVD of $SiO_2$. Figure 5.17 illustrates this data for the alumina and nickel shadow masks. For process efficiency, the best deposition method would be RF-sputtered $SiO_2$.

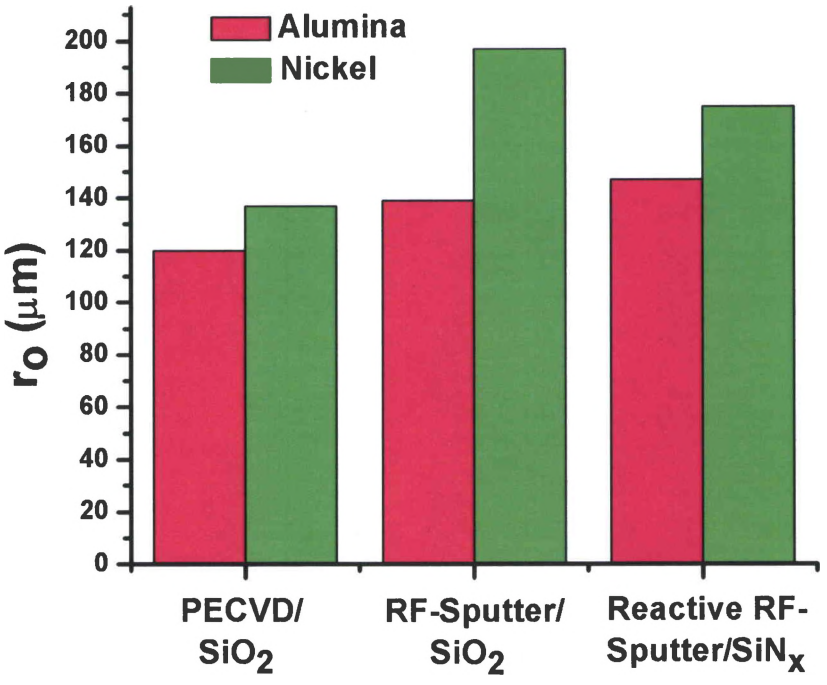


**Figure 5.16** $r_o$ for the microlenses formed by the three deposition methods using alumina and nickel shadow masks.

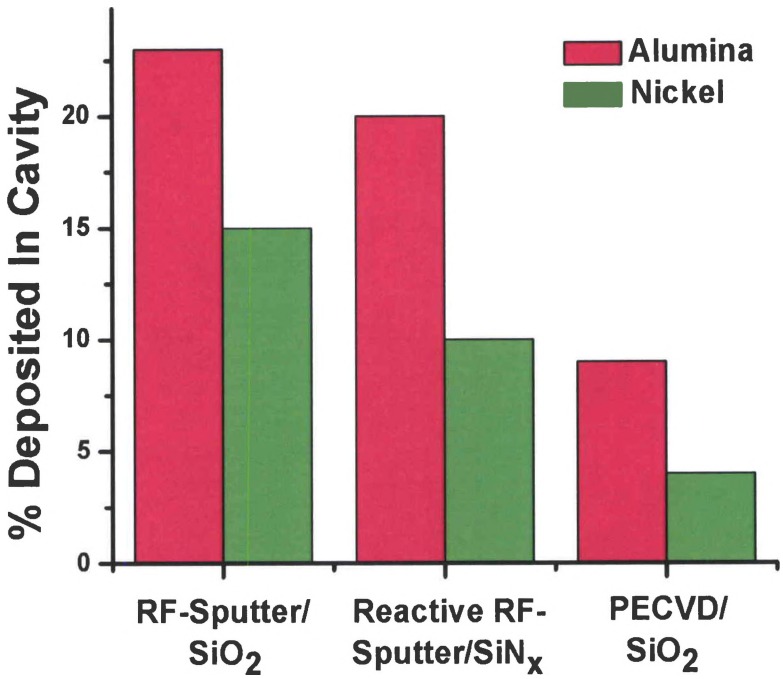


**Figure 5.17** Percent deposited inside the cavity for microlenses formed by the three deposition methods using alumina and nickel shadow masks.

# CHAPTER VI

# ENCAPSULATED LED DESIGN, FABRICATION AND TESTING

## LED Epitaxy

A PIN LED structure was grown by molecular beam epitaxy (MBE) to be used as the substrate on which non-planar dielectric encapsulations were grown. A 3" diameter $n^+$-doped GaAs wafer from AXT, Inc. was used as the substrate for MBE. A 2000Å GaAs layer n-doped with silicon was grown on the substrate at a temperature of 640°C. The quantum well structure consisted of 100Å of GaAs barrier layers surrounding ~60Å of InGaAs ($In_{0.18}Ga_{0.82}As$) quantum well growth that repeated three times, with a final 100Å GaAs barrier layer to finish the active region. The quantum well structure was grown at a temperature of 580°C. The oven temperature was then heated back to 640°C and a 100Å layer of GaAs was grown as an un-doped spacer material. To help confine the current to the center of each LED device, a 532Å GaAs/AlGaAs ($Al_{0.98}Ga_{0.02}As$ as a digital alloy layer) superlattice with carbon p-doping was grown, which could be oxidized in an oxidation furnace after the LEDs are etched into individual structures. However, no oxidation of the GaAs/AlGaAs layer was conducted for this experiment. To finish the LED structure, an un-doped 100Å GaAs layer and a 1500Å highly p-doped with C GaAs layer were grown

The exact thicknesses of the InGaAs quantum wells were not known. The time of deposition was adjusted in MBE calibration runs to pinpoint the thickness of the InGaAs quantum wells to emit at 975nm in the photoluminescence spectrum. Figure 6.1 shows the spectrum of one of the processed LEDs taken with a Hewlett Packard 70951B optical spectrum analyzer (OSA) when injected with current. The InGaAs quantum wells emit at a sharp peak centered at 983nm, which was close to the target wavelength of 975nm. The broader peak was the GaAs material in the LED structure emitting at a wavelength centered at approximately 885nm. The InGaAs quantum wells emit at a power approximately 1.5 times greater than the GaAs material in the LED structure. In a PIN LED, power emitted from the active region should be greater than the emission coming from any other material in the LED so that the intended wavelength will be prominent in the spectrum.

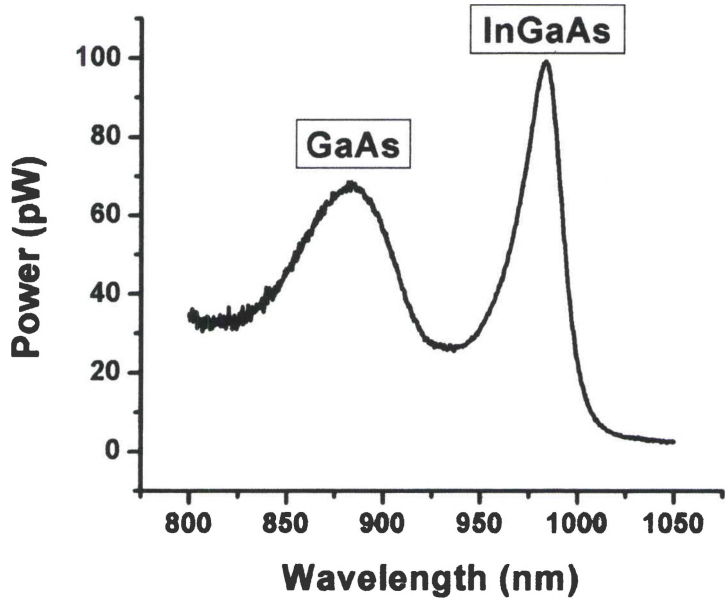


**Figure 6.1** Spectrum of the current-injected LED grown by MBE

## LED Shadow Mask Design

Using the results found from the shadow mask development study described in Chapter V, a new shadow mask was designed that incorporated the optimized geometrical parameters and shadow mask material for producing curved encapsulations for LEDs. Alumina was chosen as the mask material because it produced microlenses with more curvature, higher deposition rates and better process efficiency than the nickel shadow mask with similar cavity geometries. When designing the top hole diameter ($d_2$) parameter range for the LEDs, there was a tradeoff of higher deposition rates but less curvature as $d_2$ was increased. Therefore, the range of $d_2$ was chosen to be 70-130$\mu$m in increments of 10$\mu$m, which is within the range of 10-150$\mu$m from the original shadow mask. The diameter of the LED shadow mask cavities ($d_1$) was the same as the original shadow mask at 500$\mu$m. The mask layer thickness ($h_2$) remained constant throughout the LED shadow mask at 39$\mu$m.

The choice of values for the spacer layer thickness ($h_1$) was clear since the curvature and deposition rates increased as $h_1$ was decreased. The range of spacer layer thickness values of the LED shadow mask was chosen to be as small as possible from 9$\mu$m to 73$\mu$m in approximate increments of 10$\mu$m. The total thickness of the pre-machined 25.44mm square piece of alumina was reduced from 250$\mu$m to 135$\mu$m to aid in machining the $h_1$ and $h_3$ hole depths. The $h_1$ parameter was designed to be shallower for the LED shadow mask than the original shadow mask, and because $h_3$ is given by the relation $h_3 = \textit{substrate thickness} - h_1 - h_2$, $h_3$ would have to be machined much deeper for a piece of alumina with a thickness of 250$\mu$m. Since shallow hole depths are more

accurately machined to their designed thickness than deeper holes, the need to machine deep holes was eliminated by reducing the total thickness of the alumina.

The LED shadow mask was fabricated from a 135$\mu$m thick, 25.4mm square piece of alumina. The array of shadow mask cavities consisted of twelve identical blocks arranged in a four row, three column array. The repeated block had a pattern of 49 shadow mask cavities with seven rows and seven columns. Each of the seven columns possessed different top hole diameters ($d_2$) from 70$\mu$m to 130$\mu$m. Each of the seven rows had different spacer layer thicknesses ($h_1$) from 9$\mu$m to 73$\mu$m. The columns of shadow mask cavities were spaced 1,000$\mu$m apart from center-to-center to allow for an LED with no encapsulation to be fabricated next to each encapsulated LED. This would give a direct comparison between a bare LED and an encapsulated LED that are both made on an LED structure that has minimal differences in layer epitaxy due to location on the original 3" diameter wafer growth. The LED shadow mask also possessed five rectangular holes located between the twelve blocks that would deposit a line of dielectric material onto the LED substrate. These lines would aid in alignment to the mask set used for lithographically processing the LEDs, which is the next step in LED fabrication.

## Lithography Mask and Processing

The MBE-grown LED substrate was fabricated into individual devices with a set of masks utilizing photolithography techniques that are typical of semiconductor device fabrication. The mask set was designed with features that correspond to the location of the microlenses deposited with the LED shadow mask. A picture of four blocks of the lithography mask set with all steps combined is shown in Figure 6.2. The masks features

included negative and positive space patterns that are exposed into the photoresist and developed for etching, metal contacts or alignment marks. The general steps required to process the LEDs involved depositing the microlenses; lithography and RIE to form the dielectric into posts of different diameters; patterning the alignment metal; top p-Ohmic metal contact formation; mesa etch for device isolation and bottom n-Ohmic metal contact formation.

**Figure 6.2** Image showing four blocks of LED mask set in which all four mask designs are combined into one image.

The dielectric microlenses were deposited onto the LED structure using the LED shadow mask described in the previous section. The deposition was accomplished with a 100 minute PECVD deposition of $SiN_x$ onto a quarter wafer of the original 3" diameter MBE-grown LED structure. The shadow mask was oriented onto the LED substrate with one corner aligned to the corner of the quarter wafer. The microlenses were deposited in the center of the quarter wafer to allow for a 2mm photoresist edge bead removal. To compare the emission from the LED with the thickest microlens deposited with this technique to the emission from an LED with a planar dielectric layer deposited at that same thickness, a quarter wafer from the MBE-grown LED structure was coated with $SiN_x$ by PECVD. The microlens formed by the shadow mask cavity with a top hole diameter ($d_2$) of 130$\mu$m and a spacer layer thickness ($h_1$) of 9$\mu$m had a maximum thickness of 4540Å. The $SiN_x$ layer deposited by PECVD without a shadow mask had a comparable thickness of 4700Å measured by the profilometer. After the planar dielectric deposition, a process to remove the photoresist edge bead was performed on the wafer.

The edge bead removal process for the two quarter wafers began by spin-coating the wafer with 1813 resist for 30 seconds at 4000 rpm. The resist was baked on a hot plate at 110°C for 75 seconds. Aluminum foil was cut to cover most of the wafer except a 2mm gap around each edge. When coating a quarter wafer with photoresist, the thickness of the resist became significantly thicker around the 2mm perimeter. By covering all but the outside edge of the resist coated wafer with the aluminum foil, exposing for 60 seconds with a Karl Suss MJB-3 mask aligner system and spin developing the exposed resist for 30 seconds with AZ-351 developer followed by a 30 second DI water rinse, the edge bead was removed. By removing the thick edge bead, the lithography masks used in

future steps will lie flat on the photoresist coating, preventing diffraction of light from the mask pattern through an air gap caused by the edge bead raising the mask off of the center of the quarter wafer.

After edge bead removal, the two wafers coated with 1813 photoresist were patterned with the Dielectric Etch Mask #1. This mask possessed clear field everywhere except for solid circles of different diameters to mask off the center of each deposited $SiN_x$ microlens and three sets of alignment marks. The alignment marks consisted of two solid connecting lines spanning the outside edges of two adjacent sides of the whole device pattern that form a right angle, five solid rectangles to mask off the alignment lines of $SiN_x$ deposited by the LED shadow mask and one set of smaller alignment marks. The small alignment marks consisted of squares, plus signs and numbers to help the fine alignment (in future lithography steps) of the mask to the alignment marks already existing on the wafers. Each of the twelve blocks of microlenses deposited onto the LED substrate by the LED shadow mask corresponded to a different solid circle diameter in the Dielectric Etch Mask #1, ranging from 10$\mu$m to 120$\mu$m. Figure 6.3 shows the composite of the device features contained in the four lithography masks. The dark field solid circles that mask off the center of each deposited microlens are represented as the red circle in the device on the right in Figure 6.3.

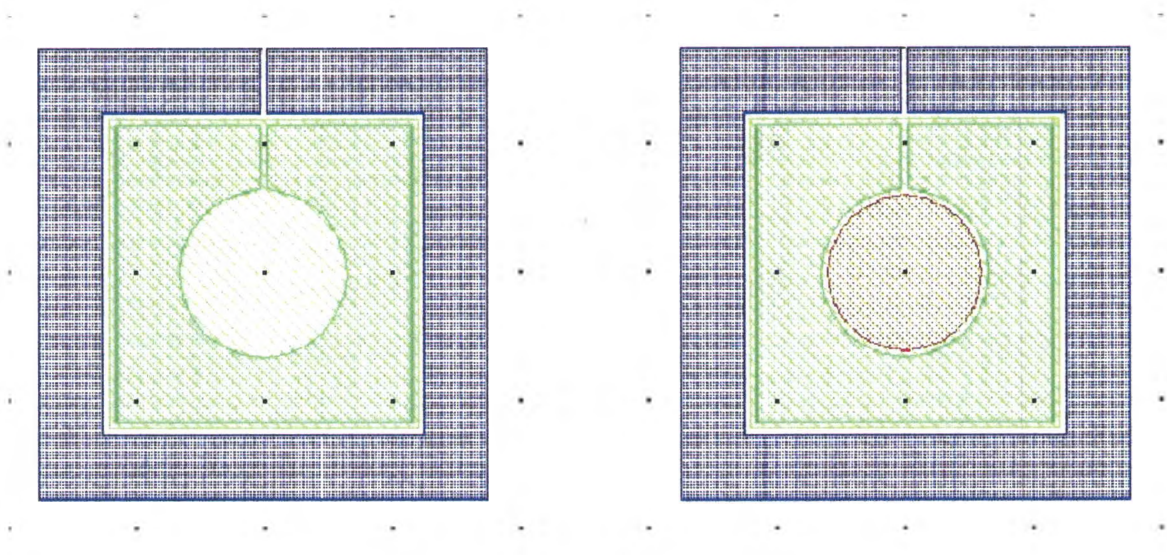

**Figure 6.3** Layout of the device features of the combined four lithography masks. The device pattern on the right will have a lens, and the device on the left will be bare. The red circle is the dielectric encapsulation post, the green square is the top p-Ohmic metal contact and the blue square is the bottom n-Ohmic metal contact.

Once the solid circles were aligned visually over the center of each microlens and the five rectangular lines were covering the deposited dielectric lines, the photoresist was exposed with the mask aligner for 14 seconds. In the case of the wafer with the planar dielectric layer, Mask #1 was positioned in the approximate center of the wafer (since there were no deposited features useful for mask alignment) and exposed with the mask aligner for 14 seconds. After this step, the wafer containing a planar dielectric layer was processed using the same techniques as the wafer with the lensed dielectric layers. The exposed photoresist was developed for 35 seconds with AZ-351 developer and rinsed with DI water for 30 seconds. This step left posts of photoresist over the center of the dielectric microlenses and five photoresist mesas over the dielectric lines for the wafer where the dielectric was deposited through the LED shadow mask. A freon-23/$O_2$ RIE

etch was performed at an RIE power of 100W with a Plasmatherm Dual Chamber system for 35 minutes to remove all excess $SiN_x$ on both wafers that was not covered by the photoresist posts or mesas. After the etch, the photoresist posts and mesas were removed by spraying the spinning wafers with an acetone gun for 10 seconds, then spraying the wafers with bottles of acetone, methanol and isopropanol (AMI) for 30 seconds each. Any remaining photoresist was removed by soaking the wafers in 90°C 1165 photoresist stripper for 5 minutes. The wafers were then cleaned of all particulates with a four minute process in a LFE barrel etcher that uses $O_2$ plasma.

The next step in lithography involved a double photoresist layer to pattern the top p-Ohmic metal contacts, two more sets of small alignment marks and lettering and numbering for device identification when viewed with a microscope. The first photoresist layer was SF-11 spun on the quarter wafers for 30 seconds at 4000 rpm and baked on a 270°C hot plate for 5 minutes. The SF-11 photoresist layer was then exposed with the deep-UV (DUV) system for 25 seconds to break some of the bonds in the photoresist and allow for undercut developing. To form the second layer of photoresist, the wafers were spin-coated with 1813 photoresist for 30 seconds at 4000 rpm and baked on a 110°C hot plate for 75 seconds. The aluminum foil edge bead mask was used to remove the edge bead from the two layers of photoresist. The photoresist around the edge of the aluminum mask was exposed with the mask aligner for 65 seconds, spin developed with AZ-351 developer for 30 seconds and DI water rinsed for 30 seconds.

The top p-Ohmic metal contact is shown in Figure 6.3 as the green square with a circular cutout in the center for encapsulated and bare LED emission. The P-Metal Mask #2 consisted of dark field everywhere except for clear areas corresponding to the top

contact patterns, two right-angled lines, five rectangular alignment marks, three sets of small alignment marks and the lettering and numbering. The inside circular diameters of the clear field top contact area of Mask #2 were 5$\mu$m wider along the perimeter (thus a larger diameter by 10$\mu$m) than their corresponding dielectric posts to allow for space between the edge of the dielectric post and the metal contact. Once Mask #2 was aligned using the two right-angled lines and five rectangular marks for coarse alignment and the first set of small alignment marks patterned by Mask #1 for fine alignment, the top 1813 layer of photoresist was exposed in the mask aligner for 16 seconds. The exposed 1813 resist was spin developed with AZ-351 developer for 30 seconds and DI water rinsed for 30 seconds.

The photoresist structures that remained were the dark field areas of Mask #2 transferred into 1813 resist with the SF-11 layer underneath that was, except for a slight amount of exposure through the 1813 layer, unexposed. To create a hardened crust on top of the remaining 1813 resist patterns and expose the newly revealed layer of SF-11 resist using the remaining 1813 resist as the mask, the wafers were exposed in the DUV system for 230 seconds. The wafers were then immersed in a bucket of NANO PMGI 101 developer for 90 seconds to fully develop the exposed SF-11 (NANO PMGI 101 developer attacks 1813 resist slowly) and provide undercut between the SF-11 and 1813 photoresist layers for successful metal lift-off.

The wafers were cleaned with a 1:10 BOE/DIW dip for 20 seconds and then coated with 200Å Ti and 2000Å Au by metal evaporation to form the top p-Ohmic contact metal. The patterns described by the clear field of Mask #2 were created in the areas on the metal-coated wafer where the patterns in the 1813 and SF-11 resists had been exposed

and developed away to reveal bare substrate. To remove the p-metal deposited on top of the masked photoresist, a lift-off procedure was conducted that began with pooling acetone on the wafer while it was suctioned onto the spinner chuck. This loosened the unexposed photoresist on the areas of the wafers where the photoresist had been masked off by the dark field of Mask #2. When the wafers were sprayed with the acetone gun while spinning, the loosened 1813 photoresist (and metal coating) was removed, leaving metal only on the bare substrate in the shape of the clear field patterns in Mask #2. The wafers were cleaned of all remaining unexposed photoresist and metal using the AMI solvent cleaning process, the heated 1165 stripper for 5 minutes and a 4 minute LFE $O_2$ etch.

The current injected into the LED from the top p-Ohmic contact was isolated to each device by physically etching away the area of LED substrate surrounding each top contact. The etch was timed to ensure that the depth of the etch went past the active layer of the surrounding LED material and into the n-doped GaAs material deposited onto the GaAs substrate during MBE. This physical isolation of each active layer underneath the top contact helped prevent current spreading to the area outside of the device, so that the current injected into the top contact can be available for electron-hole recombination in that device.

The process to accomplish the LED device isolation etch began by spin coating 1813 resist on the wafers for 30 seconds at 4000 rpm. Then the edge bead removal process, as described above, was completed. The Mesa Etch Mask #3 consisted of clear field everywhere except for solid squares that cover the area over the top p-Ohmic contacts, including the encircled bare and encapsulated LED areas, and a dark field pattern of the

second set of small alignment marks. The mask was coarsely aligned so that the solid squares covered the top p-metal contacts and finely aligned so that the small set of alignment marks covered the second set of marks patterned by Mask #2. The mask and wafers were exposed in the mask aligner for 14 seconds. The wafers were spin developed for 30 seconds with AZ-351 developer, rinsed with DI water for 30 seconds and cleaned with the LFE $O_2$ etch for 4 minutes. The wafers were then mounted to a sapphire carrier with a small drop of diffusion pump oil to adhere the wafers to the carrier and provide good thermal contact to sapphire, which was backside helium cooled to 10°C. The wafers were placed in a Plasmatherm RIE/ICP (inductively-coupled plasma) chamber and a $BCl_3/Cl_2$ etch with 100W RIE power and 600W ICP power was conducted for 70 seconds. After the etch, the photoresist squares were removed with a 5 minute soak in heated 1165 stripper.

To form the bottom n-Ohmic metal contacts, a process was performed that is very similar to that completed for the top p-Ohmic metal contacts. One difference between the two processes was that the 1813 photoresist layer was exposed with the N-Metal Mask #4 instead of the P-Metal Mask #2. Mask #4 consisted of dark field everywhere except the clear bottom contact patterns around the square top contacts and etched mesas, which is shown as the blue areas in Figure 6.3, two right-angled lines and third set of small alignment marks. The other difference was that the metal evaporated onto the photoresist pattern was n-Ohmic instead of p-Ohmic. The n-Ohmic metal consisted of 50Å Ni, 170Å Ge, 330Å Au, 150Å Ni and 3000Å Au. After the n-metal was lifted off with the same process as described for the p-metal lift-off, the wafer was placed in a Steag SHS-100 rapid thermal annealer (RTA) and heated to 410°C for 15 seconds while a 5% $H_2$ and

95% Ar forming gas was flowing through the chamber. The heating facilitated the slight mixing of the metals and the semiconductor to form an Ohmic contact instead of a Schottky contact. Figure 6.4 shows SEM images of finished LEDs with both top and bottom contacts and lensed dielectric post encapsulations that show up in the SEM pictures as dark black circles. The image on the right of Figure 6.4 shows two sets of LEDs for testing where one has an emission area covered by the lensed dielectric post and its neighbor emits from the bare LED surface.

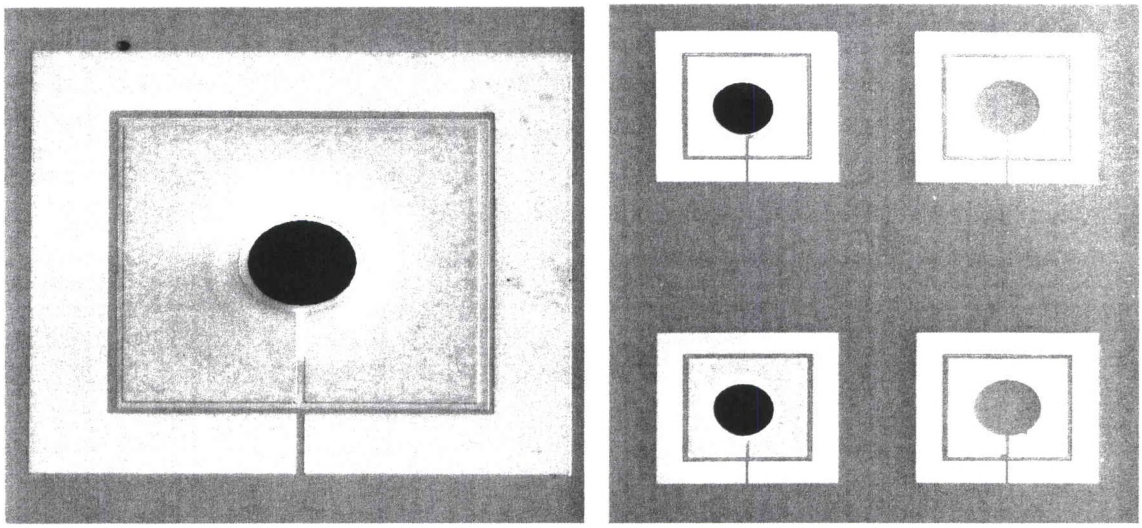

**Figure 6.4** SEM images of the LEDs after processing. On the left is an LED with a lensed dielectric post encapsulation, and the right image shows two sets of side-by-side LEDs with and without lensed dielectric encapsulations.

## Testing

The LEDs encapsulated with the aspheric microlenses should possess greater extraction efficiency when emitting from a point source than the bare LEDs, while the LEDs with planar dielectric posts should have extraction efficiencies somewhere between the encapsulated and bare LEDs, as detailed in the calculation in Chapter II. The emission patterns from encapsulated and planar dielectric post LEDs, as well as their neighboring bare LEDs were compared to verify this theory using a test station with needle probes to provide current and a camera which recorded the intensity of emission from the circular area outlined by the top contact. The wafer was held to a metal platen by a vacuum. A microscope, illuminated by a lamp, was used to aid in the adjustment of the position of the platen and LED wafer to the center of the camera's field of view. The microscope was also used to adjust the height of the camera to bring the LED surface into focus. The camera was a Spiricon SP-980M equipped with a silicon detector. No dynamic gain adjustments of the camera were conducted, allowing for direct comparison of the emission intensity coming from different LEDs. The Spiricon LBA-PC computer program processed the data coming from the camera into real-time images of the emission or single shots while averaging or summing frames. The Spiricon LBA-PC program was set to average 16 frames of the LED emission pattern coming from the camera into a single shot image. From that image, a digital circular aperture was placed in the same position as the inside circular diameter of the top contact to count the detected pixel intensity coming from only that part of the LED. The pixel intensity inside the aperture was compared for encapsulated and planar dielectric post LEDs and their neighboring bare LEDs.

For this comparison, LEDs were measured from the blocks of devices where the lensed and planar dielectric posts had 10, 30, 50, 70, 90 and 110$\mu$m diameters. Within each block, the measured devices were the encapsulated LEDs with microlenses that were formed from shadow mask cavities with 130$\mu$m top hole diameters ($d_2$) and spacer layer thicknesses ($h_1$) from 9$\mu$m to 73$\mu$m, and their bare neighbors. This group of lensed dielectric posts moves from lenses with more curvature ($h_1$ = 9$\mu$m) to less curvature ($h_1$ = 73$\mu$m). This comparison was conducted to see if the curvature of the aspheric encapsulation has an effect on emission intensity. The planar dielectric post LEDs that were measured corresponded to the same location within each block as the encapsulated LEDs. However, within each block, they should all have the same emission intensities since they have planar posts of the same thickness.

One needle probe provided the current to the top p-Ohmic contact, while the other probe acted as the ground to the n-Ohmic contact. However, emission was not detected from the LED in this configuration, possibly because the n-metal was not in good contact with the n-material below the active layer of the LED. Therefore, the backside of the wafer was evaporated with the same n-metal combination as described in the Lithography Mask and Processing section and annealed in the RTA. The metal platen holding the wafer was set as the ground contact. The backside n-metal contact allowed for certain contact with the n-doped layers below the active layer, and virtually every LED tested at an injection current of 40mA emitted light. The LEDs from the blocks of devices with 90 and 110$\mu$m diameter lensed and planar dielectric posts emitted light that saturated the camera's pixels and a 1.0 neutral density (ND) filter had to be placed in front of the camera.

## Results of Encapsulated LED

The sets of LEDs mentioned in the Testing section were tested and compared for patterns in emission intensity. The data from these measurements can be found in Appendix B. The first pattern apparent from testing the LEDs was that the emission intensity detected from the lensed, planar dielectric and bare LEDs all increased as the device location neared the center of the MBE-grown wafer. This was particularly true for the bare LEDs, where the emission intensity should be the same from any point on the wafer. This trend may be caused by slightly different layer chemistries or thicknesses grown by MBE as a function of distance away from the center of the wafer. Slight differences in carbon p-doping as a function of radial distance away from the center of the MBE-grown wafer have also been observed, which may play a role in the non-uniform bare LED emission intensity.

As predicted by the theoretical calculation of LED emission from a point source in Chapter II, the addition of both the lensed and planar dielectric layers caused the detected emission intensity to increase compared to emission from their neighboring bare LEDs. Figure 6.5 shows the increased emission detected by the Spiricon camera from an LED with a dielectric lens encapsulation (right) compared to its neighboring bare LED (left). This increase was quantified using the percent increase formula, which is expressed as

$$\%Increase = \frac{Lensed\ /\ Planar - Bare}{Bare}.$$

The percent increase formula calculates the amount, measured in percent, that the lensed or planar dielectric layers increased the emission of the LED compared to the bare LED. It was assumed that the increase in detected emission intensity was caused by changes in

the extraction efficiency due to adding dielectric layers onto the LED surface, thus reducing total internal reflection (TIR) at the LED/dielectric surface. The composition or geometry of the quantum wells or surrounding layers of the LEDs were not altered, therefore, the injection and recombination efficiencies would not change. Also, the current injected into the LEDs remained constant at 40mA throughout testing, preventing increased emission detected as a result of increased current densities in the LEDs.

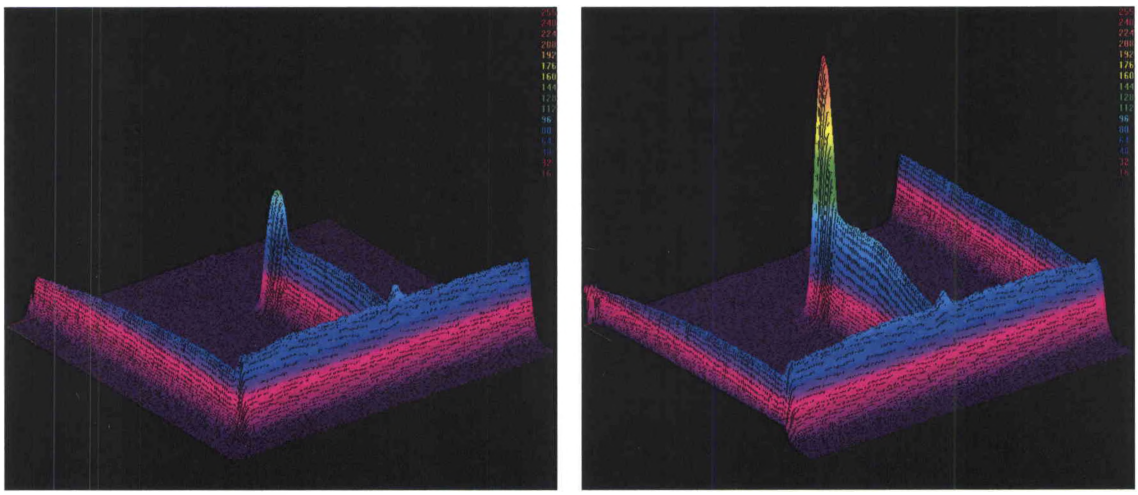

**Figure 6.5** Increased emission as a result of adding a dielectric lens to an LED (right) compared to its neighboring bare LED (left). The square emission area around and leading up to the circular emission area is bare LED substrate not covered by the top metal contact.

The radius of curvature of the dielectric lens had an overall effect on the percent increase of emission of the lensed LEDs compared to their neighboring bare LEDs. For each group of LEDs tested with the same diameter lensed dielectric posts that were formed from shadow mask cavities with the same top hole diameter ($d_2$), the emission

intensity increased as the curvature of the lenses was increased. Figure 6.6 shows that for each dielectric post diameter tested, the overall percent increase of emission decreased due to increases in spacer layer thickness ($h_1$). The increase of curvature of the encapsulations may be bringing their shape closer to the ideal spherical shaped dome that maximizes the extraction efficiency of an LED, thus causing the extraction efficiency and detected emission to increase.

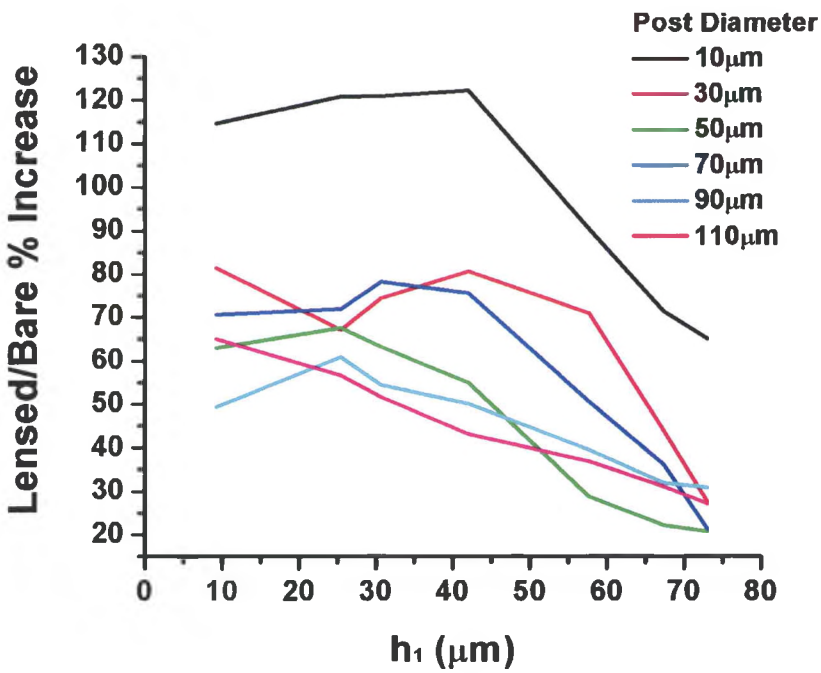


**Figure 6.6** Percent increase of emission of lensed/bare LEDs vs. spacer layer thickness ($h_1$) for each dielectric post diameter.

The extraction efficiency of an LED with an aspheric dielectric encapsulation should be greater than an LED with a planar dielectric post, according to the calculation for a point source presented in Chapter II. Emission intensities from LEDs with aspheric

dielectric posts with a thickness of 4500Å were compared to the emission from LEDs with planar dielectric posts with a similar thickness of 4700Å. Out of the six sets of LEDs tested with different post diameters, three of the LEDs with lensed dielectric posts had greater percent increase of emission compared to their bare LED neighbors than the percent increase for LEDs with planar dielectric posts. The data for this comparison is plotted in Figure 6.7. The LEDs with lensed dielectric posts with diameters of 30, 50 and 70$\mu$m had greater percent increase of emission than the LEDs with planar dielectric posts. For LEDs with 10, 90 and 110$\mu$m dielectric posts, the LEDs with planar posts had greater percent increase of emission than the LEDs with lensed posts. The data for the lensed dielectric/bare percent increase of emission decreases overall with increases in dielectric post diameter, while the planar dielectric/bare percent increase of emission shows a nonlinear relationship with dielectric post diameter.

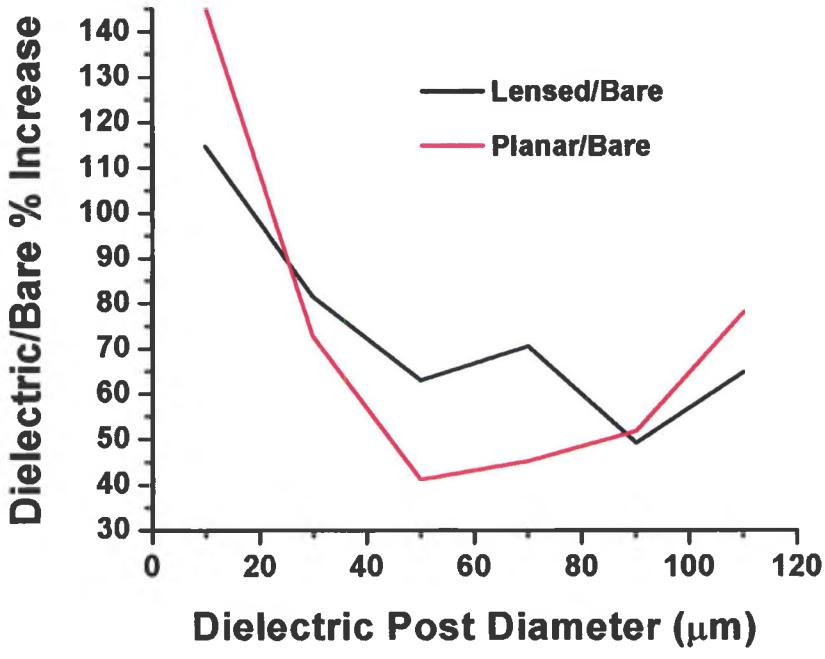


**Figure 6.7** Dielectric/Bare percent increase of emission vs. dielectric post diameter for lensed dielectric posts with the same thickness as the planar dielectric posts.

An important point to note, however, is that the LEDs that were tested for this comparison can not be considered as point sources. Oxidation of AlGaAs current confinement layers of the LEDs, after device isolation by mesa etch, is one method that could be used to make such a comparison to theory more viable. If the oxidation layer was oxidized almost completely to the center of each device, the emission area would have been reduced almost down to a point. However, since the oxidation was not performed, the LEDs emit from an extended source that covers the entire active layer isolated to each device by the mesa etch. This is clearly illustrated by the emission of the LEDs shown in Figure 6.5, which have emission coming from the areas of each device

not covered by the top contact. As a topic for future research, the oxidation of the LEDs may cause them to behave more like the theoretical predictions dictated by the point source calculations in Chapter II, meaning that the LEDs with lensed dielectric posts would have higher percent increase of emission than LEDs with planar dielectric posts, despite the dielectric post diameter.

The data presented in Figure 6.7 for the percent increase of emission of LEDs with lensed dielectric posts shows that it has a somewhat linear relationship with dielectric post diameter. This could indicate that the extraction efficiency decreases with increases in dielectric post diameter, which is also the diameter of the opening in the top metal contact that forms the aperture from which light is permitted to escape from the extended source. To investigate the dependency of extraction efficiency of an extended source LED as a function of emitting aperture radius, a calculation was performed that approximated the parabolic surface of the non-planar dielectric as hemispheric. This calculation is outlined in detail in Appendix B. The results of the calculation are shown in Figure 6.8, which used a $SiN_x$ hemispherical lens with a radius of curvature of 50$\mu$m and an index of refraction of 2.0 as the dielectric encapsulation. The graph shows that the ratio of the extraction efficiency of the encapsulated LED to that of a bare LED begins to decrease at an emitting aperture radius of about 25$\mu$m and steadily decreases down to a factor of about 1.7 extraction efficiency improvement as the emitting aperture radius is increased to 50$\mu$m. This example calculation shows that the extraction efficiency improvement created by the addition of a hemispheric dielectric encapsulation to an extended source LED does decrease as the emitting aperture is increased. Although the LEDs tested in the experimental data possess aspheric dielectric encapsulations, the

results seen in Figure 6.7 can at least be partially explained by the theory presented in the hemispherically encapsulated, extended source LED calculation.

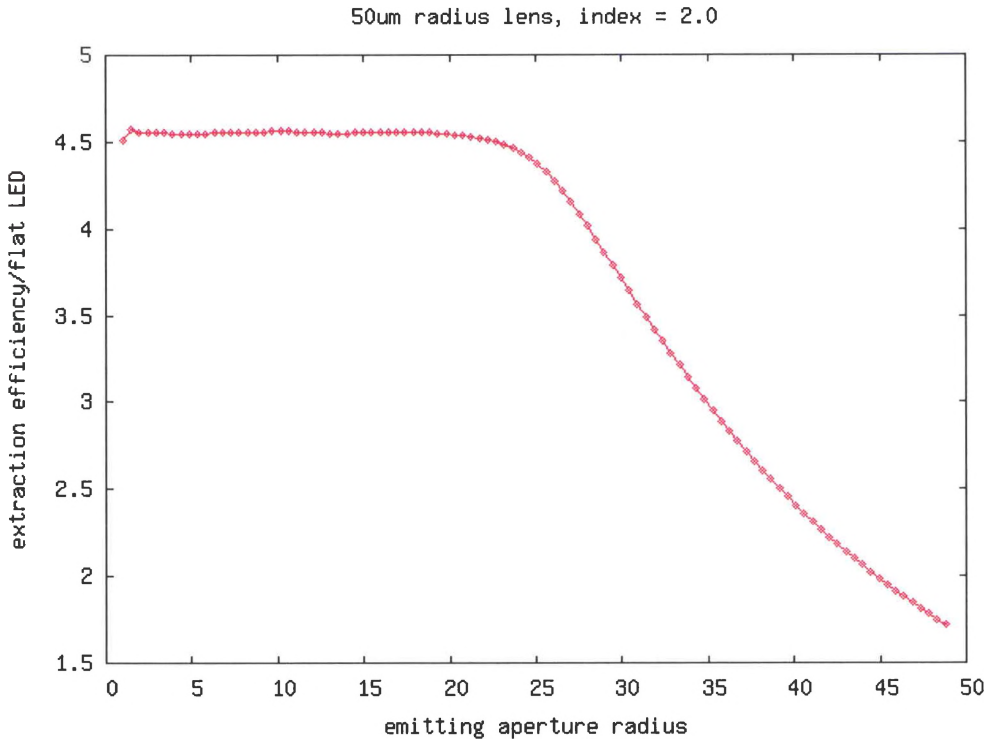


**Figure 6.8** Ratio of extraction efficiency of LED with hemispheric encapsulation compared to a bare LED vs. the emitting aperture radius. This example calculation was performed using a 50$\mu$m radius of curvature hemispherical lens of $SiN_x$ (refractive index = 2.0).

5. Increasing the diameter of the top hole of the shadow mask cavity increased the thickness, but decreased the curvature, of the deposited aspheric dielectric microlenses.
6. Fabricating the shadow mask arrays from alumina instead of nickel created microlenses with greater curvatures and thicknesses. A simulation of deposition inside a PECVD chamber was performed that partially explained this phenomenon.
7. $SiO_2$ deposited by PECVD produced microlenses with the most curvature compared to RF-sputtering of $SiO_2$ and reactive RF-sputtering of $SiN_x$.
8. The method of deposition that produced microlenses with the highest process efficiency was RF-sputtering of $SiO_2$, while the method with the lowest process efficiency was PECVD of $SiO_2$.
9. Three out of six LEDs with aspheric dielectric encapsulations possessed greater output power when compared to LEDs with planar dielectric layers with similar thicknesses to the aspheric encapsulations.

## Summary of Contributions

The results of the LED encapsulation study contribute new knowledge to the subject of LED extraction efficiency. Encapsulating LEDs with aspheric dielectric layers increased the extraction efficiency of the devices. The curvature of the aspheric dielectric layer used to encapsulate the LED has a clear effect on the LED extraction efficiency. The diameters of the emitting apertures of the extended source LEDs changed the emitted power, thus the extraction efficiencies, of the LEDs when compared to their neighboring bare LEDs. A simulation contributed to the theoretical knowledge of the extraction

efficiencies of hemispherically encapsulated, extended source LEDs with respect to the emitting aperture diameter.

The shadow mask development study contributed valuable knowledge by pioneering the manufacturing of shadow mask arrays with laser micromachining. The results of this study can be used in the future to tailor microlenses with specified thicknesses and curvatures. The effects of altering the spacer layer thickness and top hole diameter of the shadow mask cavity used for dielectric deposition have been clearly presented in this report. Switching shadow mask material from electrically insulating alumina to electrically conductive nickel has shown that the alumina shadow mask is the superior material choice. Finally, this study has created a database of knowledge regarding the use of sputtering and PECVD to deposit $SiN_x$ and $SiO_2$. This knowledge can be exploited when choosing a deposition method that will provide the desired results, such as highest microlens curvature or best process efficiency.

## Future Research

1. In a future shadow mask study, the shadow mask cavity diameter ($d_1$) could be varied, with all other mask geometrical parameters kept constant. This parameter could have an effect on the curvature, diameter and thickness of the deposited microlenses.
2. The AlGaAs current confinement layer in the LEDs grown by MBE for this study could by oxidized to confine the current, thus the emission, to a small area in the center of each device. The emission intensity of encapsulated LEDs compared to their

neighboring bare LEDs could be measured to determine if the devices follow the theoretical predictions for extraction efficiency of point source LEDs more closely.

3. RC-LEDs could be coated with monolayer aspheric dielectric encapsulations to investigate the possible improvement of light extraction from these devices.

4. $TiO_2$, a high refractive index material of 2.5, could be studied for the characteristics displayed in the microlenses deposited from this material during shadow mask deposition. This material could be utilized as the high index material in a high index contrast Bragg mirror stack.

5. The knowledge gained from this study can be exploited to deposit aspheric alternating dielectric Bragg layers on top of an unfinished VCSEL semiconductor top mirror stack. The deposition rates according to mask geometry, deposition method and mask material are known, which are of great importance when depositing multi-layer curved dielectric layers with required quarter-wave center thicknesses. The radial detuning of the thickness of the alternating dielectric layers could enhance the spatial mode properties of the VCSEL.

## REFERENCES


1. Jun Yao, Jingqin Su, Jinglei Du, Yixiao Zhang, Fuhua Gao, Feng Gao, Yongkang Guo and Zheng Cui, "Coding gray-tone mask for refractive microlens fabrication," *Microelectronic Engineering* **53**, 531-534 (2000).
2. A.H.O. Karkkainen, J.T. Rantala and M.R. Descour, "Fabrication of micro-optical structures by applying negative tone hybrid glass materials and greyscale lithography," *Electronics Letters* **38** (1), 23-24 (2002).
3. M. He, X.-C. Yuan, N.Q. Ngo, J. Bu and V. Kudryashov, "Simple reflow technique for fabrication of a microlens array in solgel glass," *Optics Letters* **28** (9), 731-733 (2003).
4. Zoran D. Popovic, Robert A. Sprague and G.A. Neville Connell, "Technique for monolithic fabrication of microlens arrays," *Applied Optics* **27** (7), 1281-1284 (1988).
5. Sung-Keun Lee, Kwang-Cheol Lee and Seung S. Lee, "A simple method for microlens fabrication by the modified LIGA process," *Journal of Micromechanics and Microengineering* **12**, 334-340 (2002).
6. Su-dong Moon, Namsuk Lee and Shinill Kang, "Fabrication of a microlens array using micro-compression molding with an electroformed mold insert," *Journal of Micromechanics and Microengineering* **13**, 98-103 (2003).

7. Seok-min Kim and Shinill Kang, "Replication qualities and optical properties of UV-moulded mirolens arrays," *Journal of Physics D: Applied Physics* **36**, 2451-2456 (2003).

8. Madanagopal V. Kunnavakkam, F. M. Houlihan, M. Schlax, J.A. Liddle, P. Kolodner, O. Nalamasu and J.A. Rogers, "Low-cost, low-loss microlens arrays fabricated by soft-lithography replication process," *Applied Physics Letters* **82** (8), 1152-1154 (2003).

9. Weixing Yu and X.-C. Yuan, "A simple method for fabrication of thick sol-gel microlens as a single-mode fiber coupler," *IEEE Photonics Technology Letters* **15** (10), 1410-1412 (2003).

10. Si-Hyun Park, Heonsu Jeon, Youn-Joon Sung and Geun-Young Yeom, "Refractive sapphire microlenses fabricated by chlorine-based inductively coupled plasma etching," *Applied Optics* **40** (22), 3698-3702 (2001).

11. T.N. Oder, J. Shakya, J.Y. Lin and H.X. Jiang, "Nitride microlens arrays for blue and ultraviolet wavelength applications," *Applied Physics Letters* **82** (21), 3692-3694 (2003).

12. Yu-Sik Kim, Jaehoon Kim, Joong-Seon Choe, Young-Geun Roh, Heonsu Jeon and J.C. Woo, "Semiconductor microlenses fabricated by one-step wet etching," *IEEE Photonics Technology Letters* **12** (5), 507-509 (2000).

13. Eun-Hyun Park and Young-Se Kwon, "Chemical etching of InGaAsP/InP using HBr-$H_3PO_4$-$K_2Cr_2O_7$ and its application to microlens array," *Conference Proceedings of the IEEE 2000 International Conference on Indium Phosphide and Related Materials*, 190-192 (2000).

14. Yong-Qi Fu, Ngoi Kok and Ann Bryan, "Microfabrication of microlens array by focused ion beam technology," *Microelectronic Engineering* **54**, 211-221 (2000).

15. N.S. Ong, Y.H. Koh and Y.Q. Fu, "Microlens array produced using hot embossing process," *Microelectronic Engineering* **60**, 365-379 (2002).

16. X.-J. Shen, Li-Wei Pan and Liwei Lin, "Microplastic embossing process: experimental and theoretical characterizations," *Sensors and Actuators A* **97-98**, 428-433 (2002).

17. R. Danzebrink and M.A. Aegerter, "Deposition of optical microlens arrays by ink-jet processes," *Thin Solid Films* **392**, 223-225 (2001).

18. Lin Che-Ping, Yang Hsiharng and Chao Ching-Kong, "A new microlens array fabrication method using UV proximity printing," *Journal of Micromechanics and Microengineering* **13**, 748-757 (2003).

19. H. Ottevaere, B. Volckaerts, J. Lamprecht, J. Schwider, A. Hermanne, I. Veretennicoff, and H. Thienpont, "Two-dimensional plastic microlens arrays by deep lithography with protons: fabrication and characterization," *Journal of Optics A: Pure and Applied Optics* **4**, S22-S28 (2002).

20. Ruediger Grunwald, Stefan Nerreter, Uwe Griebner and Hans-Joachim Kuhn, "Design, characterization and applications of multilayer micro-optics," *Proceedings of SPIE* **4437**, 40-49 (2001).

21. Pasquale Cusumano, Giuseppe Lullo, Angelo Mangione and Claudio Arnone, "Graded reflectivity micromirror arrays," *Applied Optics* **41** (1), 143-147 (2002).

22. G.M. Peake, L. Zhang, N.Y. Li, A.M. Sarangan, C.G. Willison, R.J. Shul and S.D. Hersee, "Micromachined, reusable shadow mask for integrated optical elements

grown by metalorganic chemical vapor deposition," *Journal of Vacuum Science and Technology B* **17** (5), 2070-2073 (1999).

23. Andrew M. Sarangan and Gregory M. Peake, "Enhancement of lateral mode discrimination in broad-area VCSELs using curved Bragg mirrors," *IEEE Journal of Lightwave Technology* **22**, 543-549 (2004).
24. The shadow masks detailed in this paper were created with laser micromachine fabrication by Mound Laser & Photonics Center, Inc., Miamisburg, OH; http://www.mlpc.com.
25. The numerical simulation was performed using a program developed by the Computational Fluid Dynamics Research Corporation (CFDRC).

# APPENDICES

## Appendix A

The results presented in Chapter V were taken from curve fittings performed on the 2D profiles of many deposited microlenses. An example of a curve fit, performed on a similar microlens to the one depicted in Figure 5.8, is shown in Figure A.1. This curve fit is different than the one shown in Figure 5.8 because that one was simplified for easier comprehension of the results. The actual curve fitting equation is

$$t = t_o\left[1-\left(\frac{dr-r}{dr-r_o}\right)^2\right].$$

Here $t_o$ represents the maximum thickness of the parabola fit to the 2D microlens profile. Where the fraction inside the parentheses in the equation in Chapter V was $(r/r_o)$, in actuality it is $(dr\text{-}r)/(dr\text{-}r_o)$. In this equation, $dr$ is the radial position along the scan length where the parabola fit to the 2D profile is at maximum height and $r_o$ is the radial position along the scan length where the parabolic fit crosses the radial axis at $t = 0$. For the figure in Chapter V, the center of microlens thickness was placed at $r = 0$, and $r_o$ from Figure 5.8 equals $(dr\text{-}r_o)$ in Figure A.1.

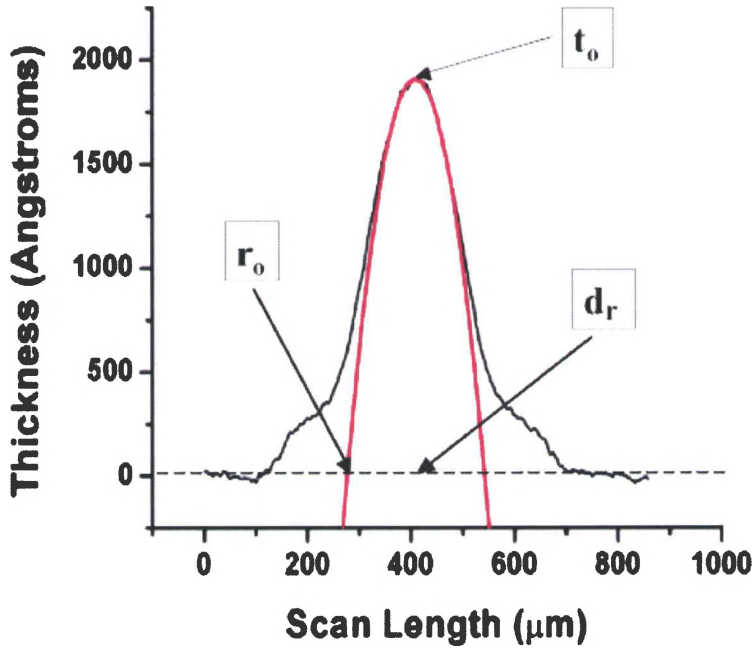


**Figure A.1** Image of curve fit of microlens to generate microlens characteristic data.

The data presented in Table A.1 shows the comparison of the fit data taken from the 2D profile of a microlens measured with a profilometer, then coated with 314Å Au and re-measured with the profilometer and the Zygo interferometer. The table shows three examples of microlenses measured with the three different techniques. The table lists the measuring tool, Au thickness, shadow mask geometric parameters with which the microlens was deposited, deposition time, maximum deposition height, step height (thickness deposited on the bare substrate), cavity deposition rate, % deposited inside the cavity, *dr*, $r_o$, ($dr$-$r_o$) and *R^2*. The cavity deposition rate is the maximum deposition height divided by the deposition time. The percent deposited inside the cavity is

$$\% = \left( \frac{Dep.Height}{StepHeight} \right) \times 100 .$$

The $R\hat{}2$ factor is a statistical measure of how well a regression line approximates real data points. An $R\hat{}2$ factor of 1.0 (100%) indicates a perfect fit. The formula for $R$ is

$$R(r,t) = \frac{[Cov(r,t)]}{[StdDev(r) \times StdDev(t)]}.$$

In this equation, *Cov(r,t)* is the covariance, which is a statistical measure of correlation of the fluctuations of two different quantities. *StdDev(r)* and *StdDev(t)* are the standard deviations, which are a statistical measure of the distance a quantity is likely to lie from its average value. By looking at the $(dr\text{-}r_o)$ and $R\hat{}2$ values presented in Table A.1, it is clear that the $(dr\text{-}r_o)$ values for each microlens are very close to one another and the $R\hat{}2$ are nearly 1.0 for all nine data sets. This means that all three methods are equally useful for measuring the 2D profile of deposited microlenses.

The remaining six tables presented in Appendix A show the comparisons for each microlens measured for the deposition of $SiO_2$ by PECVD, $SiO_2$ by RF-sputtering and $SiN_x$ by reactive RF-sputtering, where all of the deposition methods were repeated for alumina and nickel shadow masks. The data is presented in the same manner as for Table A.1. The data for each deposition is broken up into three comparisons. In the hole diameter comparison, the diameters of the top holes of the shadow mask cavities ($d_2$) are varied while the spacer layer thicknesses ($h_1$) and mask layer thicknesses ($h_2$) are held constant. In the spacer layer thickness comparison, the spacer layer thickness ($h_1$) is varied while ($d_2$) and ($h_2$) are held constant. In the mask layer thickness comparison, the mask layer thickness ($h_2$) is varied while ($h_1$) and ($d_2$) are held constant. The results from this data are discussed at length in Chapter V.

To compare the results from changing the shadow mask material from alumina to nickel and the results from the three deposition methods, the microlenses had to be formed from shadow mask cavities with similar geometries. The geometrical parameters of the cavities used for the comparisons are shown in Table 5.2. The data from the curve fits for both shadow mask materials and the three deposition methods are included in Tables A.2 – A.7. The cavity from the alumina shadow mask array is designated as M15 in Tables A.2, A.3 and A.4. The cavity from the nickel shadow mask array is designated as B15 in Tables A.5, A.6 and A.7.

**Table A.1** Comparison of profilometer and Zygo measurements with and without an Au coating

| S.M. # | Tool | Au Coat (A) | Hole Diam. (um) | Mask Thick. (um) | Spacer Thick. (um) | Time (m) | Dep. Height (A) | Step Height (A) | Cavity Dep. Rate (A/m) | % Dep. In Cavity | dr (um) | ro (um) | dr-ro (um) | R^2 |
|---|---|---|---|---|---|---|---|---|---|---|---|---|---|---|
| A12 | Prof. | 0 | 120 | 33.9 | 85.5 | 30 | 1849.16 | 15000 | 61.64 | 12.33 | 377.39 | 285.83 | 91.56 | 0.995 |
| A12 | Prof. | 314 | 120 | 33.9 | 85.5 | 30 | 1811.64 | 15000 | 60.39 | 12.08 | 459.28 | 367.11 | 92.17 | 0.9922 |
| A12 | Zygo | 314 | 120 | 33.9 | 85.5 | 30 | 1824.13 | 15000 | 60.80 | 12.16 | 391.75 | 304.88 | 86.87 | 0.9836 |
| A13 | Prof. | 0 | 130 | 33.9 | 85.5 | 30 | 2087.49 | 15000 | 69.58 | 13.92 | 392.84 | 484.24 | 91.4 | 0.9925 |
| A13 | Prof. | 314 | 130 | 33.9 | 85.5 | 30 | 2118.52 | 15000 | 70.62 | 14.12 | 469.29 | 375.62 | 93.67 | 0.9965 |
| A13 | Zygo | 314 | 130 | 33.9 | 85.5 | 30 | 2110.13 | 15000 | 70.34 | 14.07 | 360.85 | 267.67 | 93.18 | 0.9966 |
| A14 | Prof. | 0 | 140 | 33.9 | 85.5 | 30 | 2213.4 | 15000 | 73.78 | 14.76 | 472.51 | 369.56 | 102.95 | 0.9934 |
| A14 | Prof. | 314 | 140 | 33.9 | 85.5 | 30 | 2178.8 | 15000 | 72.63 | 14.53 | 400.94 | 299.94 | 101 | 0.9988 |
| A14 | Zygo | 314 | 140 | 33.9 | 85.5 | 30 | 2240.19 | 15000 | 74.67 | 14.93 | 340.56 | 239.47 | 101.09 | 0.9942 |

**Table A.2** PECVD of SiO2 with alumina shadow mask

**Hole Diameter Comparison**

| S.M. # | Hole Diam. (um) | Mask Thick. (um) | Spacer Thick. (um) | Time (m) | Dep. Height (A) | Step Height (A) | Cavity Dep. Rate (A/m) | % Dep. In Cavity | dr (um) | ro (um) | dr-ro (um) | R^2 |
|---|---|---|---|---|---|---|---|---|---|---|---|---|
| A7 | 70 | 33.9 | 85.5 | 30 | 743.14 | 15000 | 24.77 | 4.95 | 308.75 | 234.08 | 74.67 | 0.9503 |
| A8 | 80 | 33.9 | 85.5 | 30 | 792.65 | 15000 | 26.42 | 5.28 | 335.46 | 253.31 | 82.15 | 0.9804 |
| A9 | 90 | 33.9 | 85.5 | 30 | 1017.41 | 15000 | 33.91 | 6.78 | 346.17 | 262.77 | 83.4 | 0.9723 |
| A10 | 100 | 33.9 | 85.5 | 30 | 1266.87 | 15000 | 42.23 | 8.45 | 366.58 | 281.75 | 84.83 | 0.9528 |
| A11 | 110 | 33.9 | 85.5 | 30 | 1564.52 | 15000 | 52.15 | 10.43 | 380.53 | 290.7 | 89.83 | 0.9925 |
| A12 | 120 | 33.9 | 85.5 | 30 | 1849.16 | 15000 | 61.64 | 12.33 | 377.39 | 285.83 | 91.56 | 0.9950 |
| A13 | 130 | 33.9 | 85.5 | 30 | 2081.71 | 15000 | 69.39 | 13.88 | 392.75 | 298.9 | 93.85 | 0.9925 |
| A14 | 140 | 33.9 | 85.5 | 30 | 2212.99 | 15000 | 73.77 | 14.75 | 472.44 | 369.29 | 103.15 | 0.9934 |
| M8 | 80 | 96.5 | 79.1 | 30 | 490.49 | 15000 | 16.35 | 3.27 | 298.93 | 208.94 | 89.99 | 0.9714 |
| M9 | 90 | 96.5 | 79.1 | 30 | 508.84 | 15000 | 16.96 | 3.39 | 317.9 | 226.7 | 91.2 | 0.9575 |
| M10 | 100 | 96.5 | 79.1 | 30 | 655.73 | 15000 | 21.86 | 4.37 | 332.31 | 239.21 | 93.1 | 0.9781 |
| M11 | 110 | 96.5 | 79.1 | 30 | 688.51 | 15000 | 22.95 | 4.59 | 301.71 | 204.74 | 96.97 | 0.9757 |
| M12 | 120 | 96.5 | 79.1 | 30 | 1000.56 | 15000 | 33.35 | 6.67 | 305.38 | 204.87 | 100.51 | 0.9842 |
| M13 | 130 | 96.5 | 79.1 | 30 | 1021.2 | 15000 | 34.04 | 6.81 | 330.5 | 226.26 | 104.24 | 0.9923 |
| M14 | 140 | 96.5 | 79.1 | 30 | 1127.06 | 15000 | 37.57 | 7.51 | 325.09 | 208.78 | 116.31 | 0.9882 |
| M15 | 150 | 96.5 | 79.1 | 30 | 1314.01 | 15000 | 43.80 | 8.76 | 408.78 | 292 | 116.78 | 0.9491 |

**Spacer Layer Thickness Comparison**

| S.M. # | Hole Diam. (um) | Mask Thick. (um) | Spacer Thick. (um) | Time (m) | Dep. Height (A) | Step Height (A) | Cavity Dep. Rate (A/m) | % Dep. In Cavity | dr (um) | ro (um) | dr-ro (um) | R^2 |
|---|---|---|---|---|---|---|---|---|---|---|---|---|
| A14 | 140 | 33.9 | 85.5 | 30 | 2212.99 | 15000 | 73.77 | 14.75 | 472.44 | 369.29 | 103.15 | 0.9934 |
| B14 | 140 | 41.4 | 141.9 | 30 | 1129.76 | 15000 | 37.66 | 7.53 | 466.01 | 320.6 | 145.41 | 0.8986 |
| C14 | 140 | 22.5 | 195.5 | 30 | 849.46 | 15000 | 28.32 | 5.66 | 360.16 | -811.62 | 1171.78 | 0.0416 |
| D15 | 150 | 49.2 | 85.8 | 30 | 1832.15 | 15000 | 61.07 | 12.21 | 350.79 | 243.05 | 107.74 | 0.9869 |
| E15 | 150 | 54.9 | 144.2 | 30 | 1134.7 | 15000 | 37.82 | 7.56 | 365.67 | 235.61 | 130.06 | 0.9657 |
| F15 | 150 | 27.8 | 203.4 | 30 | 840.28 | 15000 | 28.01 | 5.60 | 383.46 | 211.61 | 171.85 | 0.8135 |

**Spacer Layer Thickness Comparison (Continued)**

| S.M. # | Hole Diam. (um) | Mask Thick. (um) | Spacer Thick. (um) | Time (m) | Dep. Height (A) | Step Height (A) | Cavity Dep. Rate (A/m) | % Dep. In Cavity | dr (um) | ro (um) | dr-ro (um) | R^2 |
|---|---|---|---|---|---|---|---|---|---|---|---|---|
| G15 | 150 | 70.2 | 80.7 | 30 | 1545.13 | 15000 | 51.50 | 10.30 | 347.46 | 233.93 | 113.53 | 0.9814 |
| H15 | 150 | 71.3 | 140.9 | 30 | 932.34 | 15000 | 31.08 | 6.22 | 405.76 | 260.05 | 145.71 | 0.9356 |
| I15 | 150 | 41.6 | 199.8 | 30 | 838.11 | 15000 | 27.94 | 5.59 | 319.89 | -8.85 | 328.74 | 0.5887 |
| J15 | 150 | 83.4 | 80.9 | 30 | 1570.17 | 15000 | 52.34 | 10.47 | 420 | 315.69 | 104.31 | 0.9688 |
| K15 | 150 | 69.8 | 132.9 | 30 | 1096.39 | 15000 | 36.55 | 7.31 | 425.94 | 276.71 | 149.23 | 0.9517 |
| L15 | 150 | 54.7 | 187.5 | 30 | 862.05 | 15000 | 28.74 | 5.75 | 551.81 | 378.71 | 173.1 | 0.9009 |
| M15 | 150 | 96.5 | 79.1 | 30 | 1314.01 | 15000 | 43.80 | 8.76 | 408.78 | 292 | 116.78 | 0.9491 |
| N15 | 150 | 101.2 | 131.3 | 30 | 770.32 | 15000 | 25.68 | 5.14 | 418.92 | 276.52 | 142.4 | 0.9132 |
| O15 | 150 | 58.4 | 184.1 | 30 | 869.04 | 15000 | 28.97 | 5.79 | 506.36 | 331.56 | 174.8 | 0.8487 |

**Mask Layer Thickness Comparison**

| S.M. # | Hole Diam. (um) | Mask Thick. (um) | Spacer Thick. (um) | Time (m) | Dep. Height (A) | Step Height (A) | Cavity Dep. Rate (A/m) | % Dep. In Cavity | dr (um) | ro (um) | dr-ro (um) | R^2 |
|---|---|---|---|---|---|---|---|---|---|---|---|---|
| D15 | 150 | 49.2 | 85.8 | 30 | 1832.15 | 15000 | 61.07 | 12.21 | 350.79 | 243.05 | 107.74 | 0.9869 |
| G15 | 150 | 70.2 | 80.7 | 30 | 1545.13 | 15000 | 51.50 | 10.30 | 347.46 | 233.93 | 113.53 | 0.9814 |
| J15 | 150 | 83.4 | 80.9 | 30 | 1570.17 | 15000 | 52.34 | 10.47 | 420 | 315.69 | 104.31 | 0.9688 |
| M15 | 150 | 96.5 | 79.1 | 30 | 1314.01 | 15000 | 43.80 | 8.76 | 408.78 | 292 | 116.78 | 0.9491 |
| B15 | 150 | 41.4 | 141.9 | 30 | 1314.3 | 15000 | 43.81 | 8.76 | 348.2 | 213.21 | 134.99 | 0.9159 |
| E15 | 150 | 54.9 | 144.2 | 30 | 1134.7 | 15000 | 37.82 | 7.56 | 365.67 | 235.61 | 130.06 | 0.9657 |
| K15 | 150 | 69.8 | 132.9 | 30 | 1096.39 | 15000 | 36.55 | 7.31 | 425.94 | 276.71 | 149.23 | 0.9517 |
| H15 | 150 | 71.3 | 140.9 | 30 | 932.34 | 15000 | 31.08 | 6.22 | 405.76 | 260.05 | 145.71 | 0.9356 |
| N15 | 150 | 101.2 | 131.3 | 30 | 770.32 | 15000 | 25.68 | 5.14 | 418.92 | 276.52 | 142.4 | 0.9132 |
| C15 | 150 | 22.5 | 195.5 | 30 | 1012.97 | 15000 | 33.77 | 6.75 | 371.58 | 192.45 | 179.13 | 0.8031 |
| F15 | 150 | 27.8 | 203.4 | 30 | 840.28 | 15000 | 28.01 | 5.60 | 383.46 | 211.61 | 171.85 | 0.8135 |
| I15 | 150 | 41.6 | 199.8 | 30 | 838.11 | 15000 | 27.94 | 5.59 | 319.89 | -8.85 | 328.74 | 0.5887 |
| L15 | 150 | 54.7 | 187.5 | 30 | 862.05 | 15000 | 28.74 | 5.75 | 551.81 | 378.71 | 173.1 | 0.9009 |
| O15 | 150 | 58.4 | 184.1 | 30 | 869.04 | 15000 | 28.97 | 5.79 | 506.36 | 331.56 | 174.8 | 0.8487 |

**Table A.3** RF-Sputtering of SiO2 with alumina shadow mask

**Hole Diameter Comparison**

| S.M. # | Hole Diam. (um) | Mask Thick. (um) | Spacer Thick. (um) | Time (m) | Dep. Height (A) | Step Height (A) | Cavity Dep. Rate (A/m) | % Dep. In Cavity | dr (um) | ro (um) | dr-ro (um) | R^2 |
|---|---|---|---|---|---|---|---|---|---|---|---|---|
| M4 | 40 | 96.5 | 79.1 | 86.95 | 395.56 | 6000 | 4.55 | 6.59 | 249.1 | 203.03 | 46.07 | 0.9110 |
| M5 | 50 | 96.5 | 79.1 | 86.95 | 425.84 | 6000 | 4.90 | 7.10 | 381.53 | 329.54 | 51.99 | 0.9741 |
| M6 | 60 | 96.5 | 79.1 | 86.95 | 582.46 | 6000 | 6.70 | 9.71 | 371.98 | 306.49 | 65.49 | 0.9868 |
| M7 | 70 | 96.5 | 79.1 | 86.95 | 556.92 | 6000 | 6.41 | 9.28 | 353.35 | 277.91 | 75.44 | 0.9579 |
| M8 | 80 | 96.5 | 79.1 | 86.95 | 606.71 | 6000 | 6.98 | 10.11 | 385.24 | 294.1 | 91.14 | 0.9703 |
| M9 | 90 | 96.5 | 79.1 | 86.95 | 684.92 | 6000 | 7.88 | 11.42 | 383.54 | 266.47 | 117.07 | 0.8913 |
| M10 | 100 | 96.5 | 79.1 | 86.95 | 778.29 | 6000 | 8.95 | 12.97 | 376.38 | 265.66 | 110.72 | 0.8419 |
| M11 | 110 | 96.5 | 79.1 | 86.95 | 876.26 | 6000 | 10.08 | 14.60 | 379.32 | 263.83 | 115.49 | 0.9757 |
| M12 | 120 | 96.5 | 79.1 | 86.95 | 965.27 | 6000 | 11.10 | 16.09 | 391.48 | 267.89 | 123.59 | 0.9742 |
| M13 | 130 | 96.5 | 79.1 | 86.95 | 1047.91 | 6000 | 12.05 | 17.47 | 379.17 | 258.76 | 120.41 | 0.9795 |
| M14 | 140 | 96.5 | 79.1 | 86.95 | 1263.25 | 6000 | 14.53 | 21.05 | 382.24 | 243.4 | 138.84 | 0.9292 |
| M15 | 150 | 96.5 | 79.1 | 86.95 | 1296.63 | 6000 | 14.91 | 21.61 | 401.51 | 252.24 | 149.27 | 0.9059 |

**Spacer Layer Thickness Comparison**

| S.M. # | Hole Diam. (um) | Mask Thick. (um) | Spacer Thick. (um) | Time (m) | Dep. Height (A) | Step Height (A) | Cavity Dep. Rate (A/m) | % Dep. In Cavity | dr (um) | ro (um) | dr-ro (um) | R^2 |
|---|---|---|---|---|---|---|---|---|---|---|---|---|
| A14 | 140 | 33.9 | 85.5 | 86.95 | 1978.94 | 6000 | 22.76 | 32.98 | 390.8 | 274.7 | 116.1 | 0.9855 |
| B14 | 140 | 41.4 | 141.9 | 86.95 | 1082.88 | 6000 | 12.45 | 18.05 | 394.32 | 264.16 | 130.16 | 0.9478 |
| C14 | 140 | 22.5 | 195.5 | 86.95 | 878.27 | 6000 | 10.10 | 14.64 | 419.21 | 281.39 | 137.82 | 0.9743 |
| D15 | 150 | 49.2 | 85.8 | 86.95 | 1775.15 | 6000 | 20.42 | 29.59 | 394.1 | 267.98 | 126.12 | 0.9811 |
| E15 | 150 | 54.9 | 144.2 | 86.95 | 1016.51 | 6000 | 11.69 | 16.94 | 397.32 | 242.24 | 155.08 | 0.9704 |
| F15 | 150 | 27.8 | 203.4 | 86.95 | 741.8 | 6000 | 8.53 | 12.36 | 393.3 | 203.71 | 189.59 | 0.8153 |
| G15 | 150 | 70.2 | 80.7 | 86.95 | 1446.21 | 6000 | 16.63 | 24.10 | 386.95 | 251.61 | 135.34 | 0.9789 |
| H15 | 150 | 71.3 | 140.9 | 86.95 | 964.04 | 6000 | 11.09 | 16.07 | 394.33 | 251.91 | 142.42 | 0.9818 |
| I15 | 150 | 41.6 | 199.8 | 86.95 | 760.91 | 6000 | 8.75 | 12.68 | 387.31 | 253.91 | 133.4 | 0.8510 |

**Spacer Layer Thickness Comparison (Continued)**

| S.M. # | Hole Diam. (um) | Mask Thick. (um) | Spacer Thick. (um) | Time (m) | Dep. Height (A) | Step Height (A) | Cavity Dep. Rate (A/m) | % Dep. in Cavity | dr (um) | ro (um) | dr-ro (um) | R^2 |
|---|---|---|---|---|---|---|---|---|---|---|---|---|
| J15 | 150 | 83.4 | 80.9 | 86.95 | 1332.05 | 6000 | 15.32 | 22.20 | 406.45 | 265.56 | 140.89 | 0.9845 |
| K15 | 150 | 69.8 | 132.9 | 86.95 | 1080.43 | 6000 | 12.43 | 18.01 | 413.38 | 255.95 | 157.43 | 0.9377 |
| L15 | 150 | 54.7 | 187.5 | 86.95 | 876.27 | 6000 | 10.08 | 14.60 | 419.02 | 289.16 | 129.86 | 0.9509 |
| M15 | 150 | 96.5 | 79.1 | 86.95 | 1296.63 | 6000 | 14.91 | 21.61 | 401.51 | 252.24 | 149.27 | 0.9059 |
| N15 | 150 | 101.2 | 131.3 | 86.95 | 854.71 | 6000 | 9.83 | 14.25 | 392.33 | 235.49 | 156.84 | 0.9446 |
| O15 | 150 | 58.4 | 184.1 | 86.95 | 789.35 | 6000 | 9.08 | 13.16 | 392.57 | 233.14 | 159.43 | 0.8989 |

**Mask Layer Thickness Comparison**

| S.M. # | Hole Diam. (um) | Mask Thick. (um) | Spacer Thick. (um) | Time (m) | Dep. Height (A) | Step Height (A) | Cavity Dep. Rate (A/m) | % Dep. in Cavity | dr (um) | ro (um) | dr-ro (um) | R^2 |
|---|---|---|---|---|---|---|---|---|---|---|---|---|
| D15 | 150 | 49.2 | 85.8 | 86.95 | 1775.15 | 6000 | 20.42 | 29.59 | 394.1 | 267.98 | 126.12 | 0.9811 |
| G15 | 150 | 70.2 | 80.7 | 86.95 | 1446.21 | 6000 | 16.63 | 24.10 | 386.95 | 251.61 | 135.34 | 0.9789 |
| J15 | 150 | 83.4 | 80.9 | 86.95 | 1332.05 | 6000 | 15.32 | 22.20 | 406.45 | 265.56 | 140.89 | 0.9845 |
| M15 | 150 | 96.5 | 79.1 | 86.95 | 1296.63 | 6000 | 14.91 | 21.61 | 401.51 | 252.24 | 149.27 | 0.9059 |
| B15 | 150 | 41.4 | 141.9 | 86.95 | 1251.27 | 6000 | 14.39 | 20.85 | 412.46 | 277.89 | 134.57 | 0.9481 |
| E15 | 150 | 54.9 | 144.2 | 86.95 | 1016.51 | 6000 | 11.69 | 16.94 | 397.32 | 242.24 | 155.08 | 0.9704 |
| K15 | 150 | 69.8 | 132.9 | 86.95 | 1080.43 | 6000 | 12.43 | 18.01 | 413.38 | 255.95 | 157.43 | 0.9377 |
| H15 | 150 | 71.3 | 140.9 | 86.95 | 964.04 | 6000 | 11.09 | 16.07 | 394.33 | 251.91 | 142.42 | 0.9818 |
| N15 | 150 | 101.2 | 131.3 | 86.95 | 854.71 | 6000 | 9.83 | 14.25 | 392.33 | 235.49 | 156.84 | 0.9446 |
| C15 | 150 | 22.5 | 195.5 | 86.95 | 993.07 | 6000 | 11.42 | 16.55 | 418.46 | 299.57 | 118.89 | 0.9537 |
| F15 | 150 | 27.8 | 203.4 | 86.95 | 741.8 | 6000 | 8.53 | 12.36 | 393.3 | 203.71 | 189.59 | 0.8153 |
| I15 | 150 | 41.6 | 199.8 | 86.95 | 760.91 | 6000 | 8.75 | 12.68 | 387.31 | 253.91 | 133.4 | 0.8510 |
| L15 | 150 | 54.7 | 187.5 | 86.95 | 876.27 | 6000 | 10.08 | 14.60 | 419.02 | 289.16 | 129.86 | 0.9509 |
| O15 | 150 | 58.4 | 184.1 | 86.95 | 789.35 | 6000 | 9.08 | 13.16 | 392.57 | 233.14 | 159.43 | 0.8989 |

Table A.4 Reactive RF-Sputtering of SiNx with alumina shadow mask

**Hole Diameter Comparison**

| S.M. # | Hole Diam. (um) | Mask Thick. (um) | Spacer Thick. (um) | Time (m) | Dep. Height (A) | Step Height (A) | Cavity Dep. Rate (A/m) | % Dep. In Cavity | dr (um) | ro (um) | dr-ro (um) | R^2 |
|---|---|---|---|---|---|---|---|---|---|---|---|---|
| M5 | 50 | 96.5 | 79.1 | 67.85 | 401.01 | 8300 | 5.91 | 4.83 | 326.87 | 280.09 | 46.78 | 0.8259 |
| M6 | 60 | 96.5 | 79.1 | 67.85 | 527.45 | 8300 | 7.77 | 6.35 | 324.7 | 272.62 | 52.08 | 0.9198 |
| M7 | 70 | 96.5 | 79.1 | 67.85 | 601.12 | 8300 | 8.86 | 7.24 | 347.79 | 290.46 | 57.33 | 0.9491 |
| M8 | 80 | 96.5 | 79.1 | 67.85 | 650.43 | 8300 | 9.59 | 7.84 | 347.45 | 275.93 | 71.52 | 0.8234 |
| M9 | 90 | 96.5 | 79.1 | 67.85 | | 8300 | | | | | | |
| M10 | 100 | 96.5 | 79.1 | 67.85 | 710.89 | 8300 | 10.48 | 8.56 | 371.66 | 243.83 | 127.83 | 0.8272 |
| M11 | 110 | 96.5 | 79.1 | 67.85 | 771.99 | 8300 | 11.38 | 9.30 | 398.52 | 229.58 | 168.94 | 0.8382 |
| M12 | 120 | 96.5 | 79.1 | 67.85 | 807.19 | 8300 | 11.90 | 9.73 | 442.75 | 255.09 | 187.66 | 0.7100 |
| M13 | 130 | 96.5 | 79.1 | 67.85 | 918.98 | 8300 | 13.54 | 11.07 | 441.34 | 240.62 | 200.72 | 0.7577 |
| M15 | 150 | 96.5 | 79.1 | 67.85 | 1072.31 | 8300 | 15.80 | 12.92 | 393.72 | 233.02 | 160.7 | 0.7589 |

**Spacer Layer Thickness Comparison**

| S.M. # | Hole Diam. (um) | Mask Thick. (um) | Spacer Thick. (um) | Time (m) | Dep. Height (A) | Step Height (A) | Cavity Dep. Rate (A/m) | % Dep. In Cavity | dr (um) | ro (um) | dr-ro (um) | R^2 |
|---|---|---|---|---|---|---|---|---|---|---|---|---|
| A14 | 140 | 33.9 | 85.5 | 67.85 | 1871.03 | 8300 | 27.58 | 22.54 | 370.42 | 248.94 | 121.48 | 0.9929 |
| B14 | 140 | 41.4 | 141.9 | 67.85 | 959.75 | 8300 | 14.15 | 11.56 | 385.82 | 203.38 | 182.44 | 0.8563 |
| C14 | 140 | 22.5 | 195.5 | 67.85 | 791.3 | 8300 | 11.66 | 9.53 | 374.37 | 174.48 | 199.89 | 0.5085 |
| D15 | 150 | 49.2 | 85.8 | 67.85 | 1660.72 | 8300 | 24.48 | 20.01 | 379.3 | 242.19 | 137.11 | 0.9688 |
| E15 | 150 | 54.9 | 144.2 | 67.85 | 985.83 | 8300 | 14.53 | 11.88 | 368.75 | 182.89 | 185.86 | 0.7567 |
| F15 | 150 | 27.8 | 203.4 | 67.85 | 763.05 | 8300 | 11.25 | 9.19 | 372.74 | 111.92 | 260.82 | 0.5490 |
| G15 | 150 | 70.2 | 80.7 | 67.85 | 1412.55 | 8300 | 20.82 | 17.02 | 375.44 | 239.1 | 136.34 | 0.9751 |
| H15 | 150 | 71.3 | 140.9 | 67.85 | 855.48 | 8300 | 12.61 | 10.31 | 352.33 | 137.38 | 214.95 | 0.7165 |
| I15 | 150 | 41.6 | 199.8 | 67.85 | 729.7 | 8300 | 10.75 | 8.79 | 350.38 | 114.9 | 235.48 | 0.3472 |

**Spacer Layer Thickness Comparison (Continued)**

| S.M. # | Hole Diam. (um) | Mask Thick. (um) | Spacer Thick. (um) | Time (m) | Dep. Height (A) | Step Height (A) | Cavity Dep. Rate (A/m) | % Dep. in Cavity | dr (um) | ro (um) | dr-ro (um) | R^2 |
|---|---|---|---|---|---|---|---|---|---|---|---|---|
| J15 | 150 | 83.4 | 80.9 | 67.85 | 1230.08 | 8300 | 18.13 | 14.82 | 364.12 | 192.24 | 171.88 | 0.8079 |
| K15 | 150 | 69.8 | 132.9 | 67.85 | 930 | 8300 | 13.71 | 11.20 | 375 | 130.38 | 244.62 | 0.4757 |
| L15 | 150 | 54.7 | 187.5 | 67.85 | 762.13 | 8300 | 11.23 | 9.18 | 390.52 | 196.1 | 194.42 | 0.6074 |
| M15 | 150 | 96.5 | 79.1 | 67.85 | 1072.31 | 8300 | 15.80 | 12.92 | 393.72 | 233.02 | 160.7 | 0.7589 |
| N15 | 150 | 101.2 | 131.3 | 67.85 | 805.31 | 8300 | 11.87 | 9.70 | 380.11 | 15.96 | 364.15 | 0.0510 |
| O15 | 150 | 58.4 | 184.1 | 67.85 | 726.7 | 8300 | 10.71 | 8.76 | 395.98 | 205.21 | 190.77 | 0.3465 |

**Mask Layer Thickness Comparison**

| S.M. # | Hole Diam. (um) | Mask Thick. (um) | Spacer Thick. (um) | Time (m) | Dep. Height (A) | Step Height (A) | Cavity Dep. Rate (A/m) | % Dep. in Cavity | dr (um) | ro (um) | dr-ro (um) | R^2 |
|---|---|---|---|---|---|---|---|---|---|---|---|---|
| D15 | 150 | 49.2 | 85.8 | 67.85 | 1660.72 | 8300 | 24.48 | 20.01 | 379.3 | 242.19 | 137.11 | 0.9688 |
| G15 | 150 | 70.2 | 80.7 | 67.85 | 1412.55 | 8300 | 20.82 | 17.02 | 375.44 | 239.1 | 136.34 | 0.9751 |
| J15 | 150 | 83.4 | 80.9 | 67.85 | 1230.08 | 8300 | 18.13 | 14.82 | 364.12 | 192.24 | 171.88 | 0.8079 |
| M15 | 150 | 96.5 | 79.1 | 67.85 | 1072.31 | 8300 | 15.80 | 12.92 | 393.72 | 233.02 | 160.7 | 0.7589 |
| B15 | 150 | 41.4 | 141.9 | 67.85 | 1111.02 | 8300 | 16.37 | 13.39 | 351.32 | 179.57 | 171.75 | 0.9206 |
| E15 | 150 | 54.9 | 144.2 | 67.85 | 985.83 | 8300 | 14.53 | 11.88 | 368.75 | 182.89 | 185.86 | 0.7567 |
| K15 | 150 | 69.8 | 132.9 | 67.85 | 930 | 8300 | 13.71 | 11.20 | 375 | 130.38 | 244.62 | 0.4757 |
| H15 | 150 | 71.3 | 140.9 | 67.85 | 855.48 | 8300 | 12.61 | 10.31 | 352.33 | 137.38 | 214.95 | 0.7165 |
| N15 | 150 | 101.2 | 131.3 | 67.85 | 805.31 | 8300 | 11.87 | 9.70 | 380.11 | 15.96 | 364.15 | 0.0510 |
| C15 | 150 | 22.5 | 195.5 | 67.85 | 778.48 | 8300 | 11.47 | 9.38 | 354.57 | -69.11 | 423.68 | 0.1708 |
| F15 | 150 | 27.8 | 203.4 | 67.85 | 763.05 | 8300 | 11.25 | 9.19 | 372.74 | 111.92 | 260.82 | 0.5490 |
| I15 | 150 | 41.6 | 199.8 | 67.85 | 729.7 | 8300 | 10.75 | 8.79 | 350.38 | 114.9 | 235.48 | 0.3472 |
| L15 | 150 | 54.7 | 187.5 | 67.85 | 762.13 | 8300 | 11.23 | 9.18 | 390.52 | 196.1 | 194.42 | 0.6074 |
| O15 | 150 | 58.4 | 184.1 | 67.85 | 726.7 | 8300 | 10.71 | 8.76 | 395.98 | 205.21 | 190.77 | 0.3465 |

**Table A.5** PECVD of SiO2 with nickel shadow mask

Hole Diameter Comparison

| S.M. # | Hole Diam. (um) | Mask Thick. (um) | Spacer Thick. (um) | Time (m) | Dep. Height (A) | Step Height (A) | Cavity Dep. Rate (A/m) | % Dep. In Cavity | dr (um) | ro (um) | dr-ro (um) | R^2 |
|---|---|---|---|---|---|---|---|---|---|---|---|---|
| J8 | 80 | 105.8 | 49.1 | 30 | 401.78 | 15000 | 13.39 | 2.68 | 253.93 | 180.88 | 73.05 | 0.9883 |
| J9 | 90 | 105.8 | 49.1 | 30 | 477.51 | 15000 | 15.92 | 3.18 | 198.81 | 118.46 | 80.35 | 0.9844 |
| J10 | 100 | 105.8 | 49.1 | 30 | 727.47 | 15000 | 24.25 | 4.85 | 276.74 | 182.24 | 94.5 | 0.9848 |
| J11 | 110 | 105.8 | 49.1 | 30 | 924.23 | 15000 | 30.81 | 6.16 | 296.99 | 197.29 | 99.7 | 0.9883 |
| J12 | 120 | 105.8 | 49.1 | 30 | 1042.65 | 15000 | 34.76 | 6.95 | 308.22 | 210.35 | 97.87 | 0.9960 |
| J13 | 130 | 105.8 | 49.1 | 30 | 1268.05 | 15000 | 42.27 | 8.45 | 316.62 | 213.28 | 103.34 | 0.9843 |
| J14 | 140 | 105.8 | 49.1 | 30 | 1363.73 | 15000 | 45.46 | 9.09 | 283.97 | 177.57 | 106.4 | 0.9893 |
| J15 | 150 | 105.8 | 49.1 | 30 | 1640.56 | 15000 | 54.69 | 10.94 | 371.54 | 276.92 | 94.62 | 0.9768 |

Spacer Layer Thickness Comparison

| S.M. # | Hole Diam. (um) | Mask Thick. (um) | Spacer Thick. (um) | Time (m) | Dep. Height (A) | Step Height (A) | Cavity Dep. Rate (A/m) | % Dep. In Cavity | dr (um) | ro (um) | dr-ro (um) | R^2 |
|---|---|---|---|---|---|---|---|---|---|---|---|---|
| A15 | 150 | 98.9 | 47.8 | 30 | 1127.04 | 15000 | 37.57 | 7.51 | 285.35 | 174.16 | 111.19 | 0.9916 |
| B15 | 150 | 105.5 | 76.9 | 30 | 665.66 | 15000 | 22.19 | 4.44 | 287.78 | 151.66 | 136.12 | 0.9577 |
| C15 | 150 | 110.5 | 102 | 30 | 520.51 | 15000 | 17.35 | 3.47 | 321.92 | 178.03 | 143.89 | 0.9375 |
| D15 | 150 | 109.3 | 45.4 | 30 | 823.48 | 15000 | 27.45 | 5.49 | 323.17 | 197.39 | 125.78 | 0.9766 |
| E15 | 150 | 114.5 | 75.9 | 30 | 634.82 | 15000 | 21.16 | 4.23 | 300.26 | 165.48 | 134.78 | 0.9320 |
| F15 | 150 | 116.8 | 99 | 30 | 646.77 | 15000 | 21.56 | 4.31 | 358.48 | 212.6 | 145.88 | 0.9479 |
| G15 | 150 | 105.2 | 49 | 30 | 1163.06 | 15000 | 38.77 | 7.75 | 347.17 | 236.38 | 110.79 | 0.9888 |
| H15 | 150 | 113.4 | 75.9 | 30 | 877.15 | 15000 | 29.24 | 5.85 | 350.06 | 208.55 | 141.51 | 0.9731 |
| I15 | 150 | 116.6 | 101.9 | 30 | 813.31 | 15000 | 27.11 | 5.42 | 356.09 | 217 | 139.09 | 0.9721 |
| J15 | 150 | 105.8 | 49.1 | 30 | 1640.56 | 15000 | 54.69 | 10.94 | 371.54 | 276.92 | 94.62 | 0.9768 |
| K15 | 150 | 119.7 | 78.7 | 30 | 1049.67 | 15000 | 34.99 | 7.00 | 358.43 | 228.64 | 129.79 | 0.9412 |
| L15 | 150 | 124.8 | 102.7 | 30 | 903.79 | 15000 | 30.13 | 6.03 | 328.24 | 189.59 | 138.65 | 0.9782 |

Spacer Layer Thickness Comparison (Continued)

| S.M. # | Hole Diam. (um) | Mask Thick. (um) | Spacer Thick. (um) | Time (m) | Dep. Height (A) | Step Height (A) | Cavity Dep. Rate (A/m) | % Dep. In Cavity | dr (um) | ro (um) | dr-ro (um) | R^2 |
|---|---|---|---|---|---|---|---|---|---|---|---|---|
| M15 | 150 | 112.3 | 49.3 | 30 | 1520.86 | 15000 | 50.70 | 10.14 | 372.83 | 269.12 | 103.71 | 0.9871 |
| N15 | 150 | 125.2 | 80.9 | 30 | 1009.18 | 15000 | 33.64 | 6.73 | 337.1 | 219.61 | 117.49 | 0.9886 |
| O15 | 150 | 128.9 | 109.2 | 30 | 719.1 | 15000 | 23.97 | 4.79 | 351.13 | 217.07 | 134.06 | 0.9804 |

Mask Layer Thickness Comparison

| S.M. # | Hole Diam. (um) | Mask Thick. (um) | Spacer Thick. (um) | Time (m) | Dep. Height (A) | Step Height (A) | Cavity Dep. Rate (A/m) | % Dep. In Cavity | dr (um) | ro (um) | dr-ro (um) | R^2 |
|---|---|---|---|---|---|---|---|---|---|---|---|---|
| A15 | 150 | 98.9 | 47.8 | 30 | 1127.04 | 15000 | 37.57 | 7.51 | 285.35 | 174.16 | 111.19 | 0.9916 |
| G15 | 150 | 105.2 | 49 | 30 | 1163.06 | 15000 | 38.77 | 7.75 | 347.17 | 236.38 | 110.79 | 0.9888 |
| J15 | 150 | 105.8 | 49.1 | 30 | 1640.56 | 15000 | 54.69 | 10.94 | 371.54 | 276.92 | 94.62 | 0.9768 |
| D15 | 150 | 109.3 | 45.4 | 30 | 823.48 | 15000 | 27.45 | 5.49 | 323.17 | 197.39 | 125.78 | 0.9766 |
| M15 | 150 | 112.3 | 49.3 | 30 | 1520.86 | 15000 | 50.70 | 10.14 | 372.83 | 269.12 | 103.71 | 0.9871 |
| B15 | 150 | 105.5 | 76.9 | 30 | 665.66 | 15000 | 22.19 | 4.44 | 287.78 | 151.66 | 136.12 | 0.9577 |
| H15 | 150 | 113.4 | 75.9 | 30 | 877.15 | 15000 | 29.24 | 5.85 | 350.06 | 208.55 | 141.51 | 0.9731 |
| E15 | 150 | 114.5 | 75.9 | 30 | 634.82 | 15000 | 21.16 | 4.23 | 300.26 | 165.48 | 134.78 | 0.9320 |
| K15 | 150 | 119.7 | 78.7 | 30 | 1049.67 | 15000 | 34.99 | 7.00 | 358.43 | 228.64 | 129.79 | 0.9412 |
| N15 | 150 | 125.2 | 80.9 | 30 | 1009.18 | 15000 | 33.64 | 6.73 | 337.1 | 219.61 | 117.49 | 0.9886 |
| C15 | 150 | 110.5 | 102 | 30 | 520.51 | 15000 | 17.35 | 3.47 | 321.92 | 178.03 | 143.89 | 0.9375 |
| I15 | 150 | 116.5 | 101.9 | 30 | 813.31 | 15000 | 27.11 | 5.42 | 356.09 | 217 | 139.09 | 0.9721 |
| F15 | 150 | 116.8 | 99 | 30 | 646.77 | 15000 | 21.56 | 4.31 | 358.48 | 212.6 | 145.88 | 0.9479 |
| L15 | 150 | 124.8 | 102.7 | 30 | 903.79 | 15000 | 30.13 | 6.03 | 328.24 | 189.59 | 138.65 | 0.9782 |
| O15 | 150 | 128.9 | 109.2 | 30 | 719.1 | 15000 | 23.97 | 4.79 | 351.13 | 217.07 | 134.06 | 0.9804 |

Table A.6 RF-Sputtering of SiO2 with nickel shadow mask

Hole Diameter Comparison

| S.M. # | Hole Diam. (um) | Mask Thick. (um) | Spacer Thick. (um) | Time (m) | Dep. Height (A) | Step Height (A) | Cavity Dep. Rate (A/m) | % Dep. In Cavity | dr (um) | ro (um) | dr-ro (um) | R^2 |
|---|---|---|---|---|---|---|---|---|---|---|---|---|
| J6 | 60 | 105.8 | 49.1 | 86.95 | 321.15 | 6000 | 3.69 | 5.35 | 311.28 | 244.03 | 67.25 | 0.9795 |
| J7 | 70 | 105.8 | 49.1 | 86.95 | 419.17 | 6000 | 4.82 | 6.99 | 379.44 | 307.54 | 71.9 | 0.9859 |
| J8 | 80 | 105.8 | 49.1 | 86.95 | 433.96 | 6000 | 4.99 | 7.23 | 385.8 | 299.86 | 85.94 | 0.9704 |
| J9 | 90 | 105.8 | 49.1 | 86.95 | 490.77 | 6000 | 5.64 | 8.18 | 375.02 | 281.99 | 93.03 | 0.9371 |
| J10 | 100 | 105.8 | 49.1 | 86.95 | 657.43 | 6000 | 7.56 | 10.96 | 367.71 | 258.41 | 109.3 | 0.9697 |
| J11 | 110 | 105.8 | 49.1 | 86.95 | 806.9 | 6000 | 9.28 | 13.45 | 409.92 | 275.17 | 134.75 | 0.9755 |
| J12 | 120 | 105.8 | 49.1 | 86.95 | 909.38 | 6000 | 10.46 | 15.16 | 401.68 | 273.19 | 128.49 | 0.9691 |
| J13 | 130 | 105.8 | 49.1 | 86.95 | 978.83 | 6000 | 11.26 | 16.31 | 397.38 | 253.4 | 143.98 | 0.9502 |
| J14 | 140 | 105.8 | 49.1 | 86.95 | 1084.03 | 6000 | 12.47 | 18.07 | 389.13 | 245.08 | 144.05 | 0.9790 |
| J15 | 150 | 105.8 | 49.1 | 86.95 | 1219.26 | 6000 | 14.02 | 20.32 | 380.97 | 225.94 | 155.03 | 0.9669 |

Spacer Layer Thickness Comparison

| S.M. # | Hole Diam. (um) | Mask Thick. (um) | Spacer Thick. (um) | Time (m) | Dep. Height (A) | Step Height (A) | Cavity Dep. Rate (A/m) | % Dep. In Cavity | dr (um) | ro (um) | dr-ro (um) | R^2 |
|---|---|---|---|---|---|---|---|---|---|---|---|---|
| A15 | 150 | 98.9 | 47.8 | 86.95 | 1151.49 | 6000 | 13.24 | 19.19 | 426.06 | 274.81 | 151.25 | 0.9700 |
| B15 | 150 | 105.5 | 76.9 | 86.95 | 729.51 | 6000 | 8.39 | 12.16 | 373.63 | 217.53 | 156.1 | 0.9571 |
| C15 | 150 | 110.5 | 102 | 86.95 | 619.85 | 6000 | 7.13 | 10.33 | 378.05 | 214.98 | 163.07 | 0.8731 |
| D15 | 150 | 109.3 | 46.4 | 86.95 | 916.34 | 6000 | 10.54 | 15.27 | 368.85 | 218.94 | 149.91 | 0.9716 |
| E15 | 150 | 114.5 | 75.9 | 86.95 | 711.86 | 6000 | 8.19 | 11.86 | 369.93 | 224.23 | 145.7 | 0.9594 |
| F15 | 150 | 116.8 | 99 | 86.95 | 672.93 | 6000 | 7.74 | 11.22 | 369.02 | 162.91 | 206.11 | 0.9444 |
| G15 | 150 | 105.2 | 49 | 86.95 | 1083.72 | 6000 | 12.46 | 18.06 | 370.72 | 209.16 | 161.56 | 0.8888 |
| H15 | 150 | 113.4 | 75.9 | 86.95 | 857.08 | 6000 | 9.86 | 14.28 | 371.42 | 206.74 | 164.68 | 0.9395 |
| I15 | 150 | 116.5 | 101.9 | 86.95 | 800.19 | 6000 | 9.20 | 13.34 | 372.82 | 202.88 | 169.94 | 0.9442 |

**Spacer Layer Thickness Comparison (Continued)**

| S.M. # | Hole Diam. (um) | Mask Thick. (um) | Spacer Thick. (um) | Time (m) | Dep. Height (A) | Step Height (A) | Cavity Dep. Rate (A/m) | % Dep. In Cavity | dr (um) | ro (um) | dr-ro (um) | R^2 |
|---|---|---|---|---|---|---|---|---|---|---|---|---|
| J15 | 150 | 105.8 | 49.1 | 86.95 | 1219.26 | 6000 | 14.02 | 20.32 | 380.97 | 225.94 | 155.03 | 0.9669 |
| K15 | 150 | 119.7 | 78.7 | 86.95 | 914.55 | 6000 | 10.52 | 15.24 | 381.69 | 229.7 | 151.99 | 0.9416 |
| L15 | 150 | 124.8 | 102.7 | 86.95 | 842.11 | 6000 | 9.68 | 14.04 | 381.35 | 219.28 | 162.07 | 0.9444 |
| M15 | 150 | 112.3 | 49.3 | 86.95 | 1266.13 | 6000 | 14.56 | 21.10 | 377.32 | 233.57 | 143.75 | 0.9582 |
| N15 | 150 | 125.2 | 80.9 | 86.95 | 936.53 | 6000 | 10.77 | 15.61 | 380.15 | 211.61 | 168.54 | 0.9295 |
| O15 | 150 | 128.8 | 109.2 | 86.95 | 793.38 | 6000 | 9.12 | 13.22 | 385.36 | 231.53 | 153.83 | 0.9480 |

**Mask Layer Thickness Comparison**

| S.M. # | Hole Diam. (um) | Mask Thick. (um) | Spacer Thick. (um) | Time (m) | Dep. Height (A) | Step Height (A) | Cavity Dep. Rate (A/m) | % Dep. In Cavity | dr (um) | ro (um) | dr-ro (um) | R^2 |
|---|---|---|---|---|---|---|---|---|---|---|---|---|
| A15 | 150 | 98.9 | 47.8 | 86.95 | 1151.49 | 6000 | 13.24 | 19.19 | 426.06 | 274.81 | 151.25 | 0.9700 |
| G15 | 150 | 105.2 | 49 | 86.95 | 1083.72 | 6000 | 12.46 | 18.06 | 370.72 | 209.16 | 161.56 | 0.8888 |
| J15 | 150 | 105.8 | 49.1 | 86.95 | 1219.26 | 6000 | 14.02 | 20.32 | 380.97 | 225.94 | 155.03 | 0.9669 |
| D15 | 150 | 109.3 | 45.4 | 86.95 | 916.34 | 6000 | 10.54 | 15.27 | 368.85 | 218.94 | 149.91 | 0.9716 |
| M15 | 150 | 112.3 | 49.3 | 86.95 | 1266.13 | 6000 | 14.56 | 21.10 | 377.32 | 233.57 | 143.75 | 0.9582 |
| B15 | 150 | 105.5 | 76.9 | 86.95 | 729.51 | 6000 | 8.39 | 12.16 | 373.63 | 217.53 | 156.1 | 0.9571 |
| H15 | 150 | 113.4 | 75.9 | 86.95 | 857.08 | 6000 | 9.86 | 14.28 | 371.42 | 206.74 | 164.68 | 0.9395 |
| E15 | 150 | 114.5 | 75.9 | 86.95 | 711.86 | 6000 | 8.19 | 11.86 | 369.93 | 224.23 | 145.7 | 0.9594 |
| K15 | 150 | 119.7 | 78.7 | 86.95 | 914.55 | 6000 | 10.52 | 15.24 | 381.69 | 229.7 | 151.99 | 0.9416 |
| N15 | 150 | 125.2 | 80.9 | 86.95 | 936.53 | 6000 | 10.77 | 15.61 | 380.15 | 211.61 | 168.54 | 0.9295 |
| C15 | 150 | 110.5 | 102 | 86.95 | 619.85 | 6000 | 7.13 | 10.33 | 378.05 | 214.98 | 163.07 | 0.8731 |
| I15 | 150 | 116.5 | 101.9 | 86.95 | 800.19 | 6000 | 9.20 | 13.34 | 372.82 | 202.88 | 169.94 | 0.9442 |
| F15 | 150 | 116.8 | 99 | 86.95 | 672.93 | 6000 | 7.74 | 11.22 | 369.02 | 162.91 | 206.11 | 0.9444 |
| L15 | 150 | 124.8 | 102.7 | 86.95 | 842.11 | 6000 | 9.68 | 14.04 | 381.35 | 219.28 | 162.07 | 0.9444 |
| O15 | 150 | 128.8 | 109.2 | 86.95 | 793.38 | 6000 | 9.12 | 13.22 | 385.36 | 231.53 | 153.83 | 0.9480 |

Table A.7 Reactive RF-Sputtering of SiNx with nickel shadow mask

**Hole Diameter Comparison**

| S.M. # | Hole Diam. (um) | Mask Thick. (um) | Spacer Thick. (um) | Time (m) | Dep. Height (A) | Step Height (A) | Cavity Dep. Rate (A/m) | % Dep. In Cavity | dr (um) | ro (um) | dr-ro (um) | R^2 |
|---|---|---|---|---|---|---|---|---|---|---|---|---|
| J4 | 40 | 105.8 | 49.1 | 67.85 | 268.79 | 8300 | 3.96 | 3.24 | 362.62 | 302.7 | 59.92 | 0.9081 |
| J5 | 50 | 105.8 | 49.1 | 67.85 | 363.62 | 8300 | 5.36 | 4.38 | 366.28 | 285.2 | 81.08 | 0.9777 |
| J6 | 60 | 105.8 | 49.1 | 67.85 | 434.27 | 8300 | 6.40 | 5.23 | 369.41 | 280.79 | 88.62 | 0.9855 |
| J7 | 70 | 105.8 | 49.1 | 67.85 | 447.24 | 8300 | 6.59 | 5.39 | 380.1 | 282.43 | 97.67 | 0.9494 |
| J8 | 80 | 105.8 | 49.1 | 67.85 | 518.66 | 8300 | 7.64 | 6.25 | 374.89 | 266.63 | 108.26 | 0.9626 |
| J9 | 90 | 105.8 | 49.1 | 67.85 | 675.46 | 8300 | 9.96 | 8.14 | 371.83 | 242.63 | 129.2 | 0.9441 |
| J10 | 100 | 105.8 | 49.1 | 67.85 | 790.16 | 8300 | 11.65 | 9.52 | 384.25 | 200.51 | 183.74 | 0.8888 |
| J11 | 110 | 105.8 | 49.1 | 67.85 | 888.52 | 8300 | 13.10 | 10.71 | 393.14 | 173.5 | 219.64 | 0.8057 |
| J12 | 120 | 105.8 | 49.1 | 67.85 | 884.3 | 8300 | 13.03 | 10.65 | 394.97 | 185.14 | 209.83 | 0.9200 |
| J13 | 130 | 105.8 | 49.1 | 67.85 | 960.46 | 8300 | 14.16 | 11.57 | 407.52 | 221.21 | 186.31 | 0.9677 |
| J14 | 140 | 105.8 | 49.1 | 67.85 | 1080.37 | 8300 | 15.92 | 13.02 | 414.2 | 242 | 172.2 | 0.9613 |
| J15 | 150 | 105.8 | 49.1 | 67.85 | 1211.07 | 8300 | 17.85 | 14.59 | 446.06 | 229.89 | 216.17 | 0.6831 |

**Spacer Layer Thickness Comparison**

| S.M. # | Hole Diam. (um) | Mask Thick. (um) | Spacer Thick. (um) | Time (m) | Dep. Height (A) | Step Height (A) | Cavity Dep. Rate (A/m) | % Dep. In Cavity | dr (um) | ro (um) | dr-ro (um) | R^2 |
|---|---|---|---|---|---|---|---|---|---|---|---|---|
| A15 | 150 | 98.9 | 47.8 | 67.85 | 1389.3 | 8300 | 20.48 | 16.74 | 357.37 | 185.39 | 171.98 | 0.9342 |
| B15 | 150 | 105.5 | 76.9 | 67.85 | 982.61 | 8300 | 14.48 | 11.84 | 374.74 | 143.87 | 230.87 | 0.8573 |
| C15 | 150 | 110.5 | 102 | 67.85 | 789.78 | 8300 | 11.64 | 9.52 | 397.77 | 232.89 | 164.88 | 0.9569 |
| D15 | 150 | 109.3 | 45.4 | 67.85 | 1140.77 | 8300 | 16.81 | 13.74 | 399 | 198.13 | 200.87 | 0.9413 |
| E15 | 150 | 114.5 | 75.9 | 67.85 | 921.16 | 8300 | 13.58 | 11.10 | 399.76 | 145.19 | 254.57 | 0.7716 |
| F15 | 150 | 116.8 | 99 | 67.85 | 759.51 | 8300 | 11.19 | 9.15 | 388.84 | 178.93 | 209.91 | 0.8249 |
| G15 | 150 | 105.2 | 49 | 67.85 | 1204.09 | 8300 | 17.75 | 14.51 | 395.36 | 179.14 | 216.22 | 0.8026 |
| H15 | 150 | 113.4 | 75.9 | 67.85 | 941.03 | 8300 | 13.87 | 11.34 | 403.89 | 92.42 | 311.47 | 0.7720 |
| I15 | 150 | 116.5 | 101.9 | 67.85 | 834.87 | 8300 | 12.30 | 10.06 | 433.01 | 253.5 | 179.51 | 0.8156 |

**Spacer Layer Thickness Comparison (Continued)**

| S.M. # | Hole Diam. (um) | Mask Thick. (um) | Spacer Thick. (um) | Time (m) | Dep. Height (A) | Step Height (A) | Cavity Dep. Rate (A/m) | % Dep. In Cavity | dr (um) | ro (um) | dr-ro (um) | R^2 |
|---|---|---|---|---|---|---|---|---|---|---|---|---|
| J15 | 150 | 105.8 | 49.1 | 67.85 | 1211.07 | 8300 | 17.85 | 14.59 | 446.06 | 229.89 | 216.17 | 0.6831 |
| K15 | 150 | 119.7 | 78.7 | 67.85 | 555.03 | 8300 | 8.18 | 6.69 | 387.01 | 240.63 | 146.38 | 0.9338 |
| L15 | 150 | 124.7 | 102.7 | 67.85 | 841.8 | 8300 | 12.41 | 10.14 | 444.01 | 244.25 | 199.76 | 0.7439 |
| M15 | 150 | 112.3 | 49.3 | 67.85 | 1269.94 | 8300 | 18.72 | 15.30 | 398.06 | 219.62 | 178.44 | 0.9485 |
| N15 | 150 | 125.2 | 80.9 | 67.85 | 939.53 | 8300 | 13.85 | 11.32 | 389.45 | 219.98 | 169.47 | 0.9639 |
| O15 | 150 | 128.5 | 109.2 | 67.85 | 859.99 | 8300 | 12.67 | 10.36 | 404.59 | 146.65 | 257.94 | 0.6452 |

**Mask Layer Thickness Comparison**

| S.M. # | Hole Diam. (um) | Mask Thick. (um) | Spacer Thick. (um) | Time (m) | Dep. Height (A) | Step Height (A) | Cavity Dep. Rate (A/m) | % Dep. In Cavity | dr (um) | ro (um) | dr-ro (um) | R^2 |
|---|---|---|---|---|---|---|---|---|---|---|---|---|
| A15 | 150 | 98.9 | 47.8 | 67.85 | 1389.3 | 8300 | 20.48 | 16.74 | 357.37 | 185.39 | 171.98 | 0.9342 |
| G15 | 150 | 105.2 | 49 | 67.85 | 1204.09 | 8300 | 17.75 | 14.51 | 395.36 | 179.14 | 216.22 | 0.8026 |
| J15 | 150 | 105.8 | 49.1 | 67.85 | 1211.07 | 8300 | 17.85 | 14.59 | 446.06 | 229.89 | 216.17 | 0.6831 |
| D15 | 150 | 109.3 | 45.4 | 67.85 | 1140.77 | 8300 | 16.81 | 13.74 | 399 | 198.13 | 200.87 | 0.9413 |
| M15 | 150 | 112.3 | 49.3 | 67.85 | 1269.94 | 8300 | 18.72 | 15.30 | 398.06 | 219.62 | 178.44 | 0.9485 |
| B15 | 150 | 105.5 | 76.9 | 67.85 | 982.61 | 8300 | 14.48 | 11.84 | 374.74 | 143.87 | 230.87 | 0.8573 |
| E15 | 150 | 114.5 | 75.9 | 67.85 | 921.16 | 8300 | 13.58 | 11.10 | 399.76 | 145.19 | 254.57 | 0.7716 |
| K15 | 150 | 119.7 | 78.7 | 67.85 | 555.03 | 8300 | 8.18 | 6.69 | 387.01 | 240.63 | 146.38 | 0.9338 |
| N15 | 150 | 125.2 | 80.9 | 67.85 | 939.53 | 8300 | 13.85 | 11.32 | 389.45 | 219.98 | 169.47 | 0.9639 |
| C15 | 150 | 110.5 | 102 | 67.85 | 789.78 | 8300 | 11.64 | 9.52 | 397.77 | 232.89 | 164.88 | 0.9569 |
| I15 | 150 | 116.5 | 101.9 | 67.85 | 834.87 | 8300 | 12.30 | 10.06 | 433.01 | 253.5 | 179.51 | 0.8156 |
| F15 | 150 | 116.8 | 99 | 67.85 | 759.51 | 8300 | 11.19 | 9.15 | 388.84 | 178.93 | 209.91 | 0.8249 |
| L15 | 150 | 124.7 | 102.7 | 67.85 | 841.8 | 8300 | 12.41 | 10.14 | 444.01 | 244.25 | 199.76 | 0.7439 |
| O15 | 150 | 128.5 | 109.2 | 67.85 | 859.99 | 8300 | 12.67 | 10.36 | 404.59 | 146.65 | 257.94 | 0.6452 |

## Appendix B

Table B.1 describes the data taken from the LED encapsulation study. The data is presented by block (emitting aperture diameter), location within block, $h_1$ and $d_2$ corresponding to the shadow mask parameters that formed that encapsulation and the bare and lensed or planar encapsulated LED emission intensity. The raw data for these values is taken from the Spiricon LBA-PC program and is of arbitrary units. The data for the bare and encapsulated LEDs are then divided to get the ratio of emission, which is denoted in Table B.1 as Lensed/Bare and Planar/Bare. The percent increase of emission created by encapsulating the LEDs compared to the bare LEDs is presented in the next column after the ratio. The conclusions presented in Chapter VI originate from comparisons of the data presented in Table B.1.

**Table B.1** LED emission results

| Block | Location | h1 | d2 | Bare | Lensed | Lensed/Bare | % Increase | Bare | Planar | Planar/Bare | % Increase |
|---|---|---|---|---|---|---|---|---|---|---|---|
| 10um | G1 | 9.3 | 130 | 77,292 | 165,858 | 2.15 | 114.6 | 35,630 | 87,418 | 2.45 | 145.35 |
| | G2 | 25.5 | 130 | 79,460 | 175,335 | 2.21 | 120.7 | 40,524 | 93,945 | 2.32 | 131.83 |
| | G3 | 30.7 | 130 | 85,022 | 187,726 | 2.21 | 120.8 | 41,210 | 97,994 | 2.38 | 137.79 |
| | G4 | 42.0 | 130 | 74,263 | 164,999 | 2.22 | 122.2 | 45,148 | 97,200 | 2.15 | 115.29 |
| | G5 | 57.7 | 130 | 78,519 | 149,453 | 1.90 | 90.3 | 52,181 | 106,782 | 2.05 | 104.64 |
| | G6 | 67.3 | 130 | 83,215 | 142,618 | 1.71 | 71.4 | 56,513 | 106,420 | 1.88 | 88.31 |
| | G7 | 73.0 | 130 | 89,731 | 148,085 | 1.65 | 65.0 | 60,360 | 111,782 | 1.85 | 85.19 |
| 30um | G1 | 9.3 | 130 | 669,549 | 1,214,178 | 1.81 | 81.3 | 557,215 | 961,506 | 1.73 | 72.56 |
| | G2 | 25.5 | 130 | 735,089 | 1,227,444 | 1.67 | 67.0 | 661,543 | 1,036,619 | 1.57 | 56.70 |
| | G3 | 30.7 | 130 | 790,942 | 1,379,771 | 1.74 | 74.4 | 754,025 | 1,144,752 | 1.52 | 51.82 |
| | G4 | 42.0 | 130 | 908,421 | 1,639,755 | 1.81 | 80.5 | 932,504 | 1,304,279 | 1.40 | 39.87 |
| | G5 | 57.7 | 130 | 998,671 | 1,705,451 | 1.71 | 70.8 | 1,161,717 | 1,521,993 | 1.31 | 31.01 |
| | G6 | 67.3 | 130 | 1,106,394 | 1,590,961 | 1.44 | 43.8 | 1,481,418 | 1,870,707 | 1.26 | 26.28 |
| | G7 | 73.0 | 130 | 1,333,717 | 1,700,562 | 1.28 | 27.5 | 1,973,286 | 2,296,956 | 1.16 | 16.40 |
| 50um | G1 | 9.3 | 130 | 2,544,792 | 4,149,272 | 1.63 | 63.0 | 2,931,292 | 4,136,800 | 1.41 | 41.13 |
| | G2 | 25.5 | 130 | 2,904,740 | 4,869,664 | 1.68 | 67.6 | 3,681,637 | 4,803,411 | 1.30 | 30.47 |
| | G3 | 30.7 | 130 | 3,498,976 | 5,711,187 | 1.63 | 63.2 | 4,632,477 | 6,089,235 | 1.31 | 31.45 |
| | G4 | 42.0 | 130 | 4,066,010 | 6,299,779 | 1.55 | 54.9 | 6,179,023 | 7,652,986 | 1.24 | 23.85 |
| | G5 | 57.7 | 130 | 5,070,568 | 6,530,556 | 1.29 | 28.8 | 7,868,614 | 9,891,417 | 1.26 | 25.71 |
| | G6 | 67.3 | 130 | 6,317,942 | 7,719,704 | 1.22 | 22.2 | 9,950,830 | 12,520,166 | 1.26 | 25.82 |
| | G7 | 73.0 | 130 | 7,902,153 | 9,545,265 | 1.21 | 20.8 | 11,696,684 | 15,692,856 | 1.34 | 34.16 |
| 70um | G1 | 9.3 | 130 | 3,769,011 | 6,426,304 | 1.71 | 70.5 | 4,474,461 | 6,497,829 | 1.45 | 45.22 |
| | G2 | 25.5 | 130 | 4,270,041 | 7,337,065 | 1.72 | 71.8 | 5,118,654 | 6,989,319 | 1.37 | 36.55 |
| | G3 | 30.7 | 130 | 4,764,905 | 8,492,311 | 1.78 | 78.2 | 6,083,724 | 8,092,465 | 1.33 | 33.02 |
| | G4 | 42.0 | 130 | 5,477,302 | 9,612,580 | 1.75 | 75.5 | 7,463,068 | 9,152,849 | 1.23 | 22.64 |
| | G5 | 57.7 | 130 | 6,167,523 | 9,280,119 | 1.50 | 50.5 | no light | | | |
| | G6 | 67.3 | 130 | 7,181,217 | 9,770,965 | 1.36 | 36.1 | 10,171,152 | 12,624,996 | 1.24 | 24.13 |
| | G7 | 73.0 | 130 | 8,497,405 | 10,311,285 | 1.21 | 21.3 | 11,646,548 | 14,403,812 | 1.24 | 23.67 |

| Block | Location | h1 | d2 | Bare | Lensed | Lensed/Bare |
|---|---|---|---|---|---|---|
| 90um | G1 | 9.3 | 130 | 4,742,476 | 7,079,784 | 1.49 |
| (ND 1.0) | G2 | 25.5 | 130 | 5,266,368 | 8,471,343 | 1.61 |
| | G3 | 30.7 | 130 | 6,466,141 | 9,989,910 | 1.54 |
| | G4 | 42.0 | 130 | 6,680,988 | 10,026,479 | 1.50 |
| | G5 | 57.7 | 130 | 7,078,617 | 9,872,028 | 1.39 |
| | G6 | 67.3 | 130 | 8,084,377 | 10,662,194 | 1.32 |
| | G7 | 73.0 | 130 | 8,377,012 | 10,968,532 | 1.31 |
| 110um | G1 | 9.3 | 130 | 8,824,877 | 14,550,535 | 1.65 |
| (ND 1.0) | G2 | 25.5 | 130 | 9,426,687 | 14,761,685 | 1.57 |
| | G3 | 30.7 | 130 | 9,493,368 | 14,381,060 | 1.51 |
| | G4 | 42.0 | 130 | 10,587,965 | 15,137,382 | 1.43 |
| | G5 | 57.7 | 130 | 10,603,300 | 14,496,175 | 1.37 |
| | G6 | 67.3 | 130 | 11,383,995 | 14,909,660 | 1.31 |
| | G7 | 73.0 | 130 | 11,666,166 | 14,822,903 | 1.27 |

| % Increase | Bare | Planar | Planar/Bare | % Increase |
|---|---|---|---|---|
| 49.3 | 5,326,625 | 8,083,146 | 1.52 | 51.75 |
| 60.9 | 5,882,529 | 9,443,848 | 1.61 | 60.54 |
| 54.5 | 6,218,860 | 10,704,812 | 1.72 | 72.13 |
| 50.1 | 6,679,281 | 11,714,869 | 1.75 | 75.39 |
| 39.5 | 7,234,831 | 12,391,364 | 1.71 | 71.27 |
| 31.9 | 7,290,295 | 12,586,403 | 1.73 | 72.65 |
| 30.9 | 7,429,035 | 13,256,093 | 1.78 | 78.44 |
| 64.9 | 8,717,496 | 15,508,313 | 1.78 | 77.90 |
| 56.6 | 9,121,096 | 16,304,312 | 1.79 | 78.75 |
| 51.5 | 9,519,041 | 17,083,335 | 1.79 | 79.46 |
| 43.0 | 9,911,985 | 17,273,929 | 1.74 | 74.27 |
| 36.7 | 10,100,060 | 17,897,990 | 1.77 | 77.21 |
| 31.0 | 10,199,698 | 18,547,217 | 1.82 | 81.84 |
| 27.1 | 10,728,145 | 18,901,576 | 1.76 | 76.19 |

The following is the derivation of the extraction efficiency, as a function of emitting aperture diameter, of a hemispherically encapsulated, extended source LED. Figure B.1 shows a diagram of the parameters used to derive the extraction efficiency. This derivation was used to produce the results described in Chapter VI.

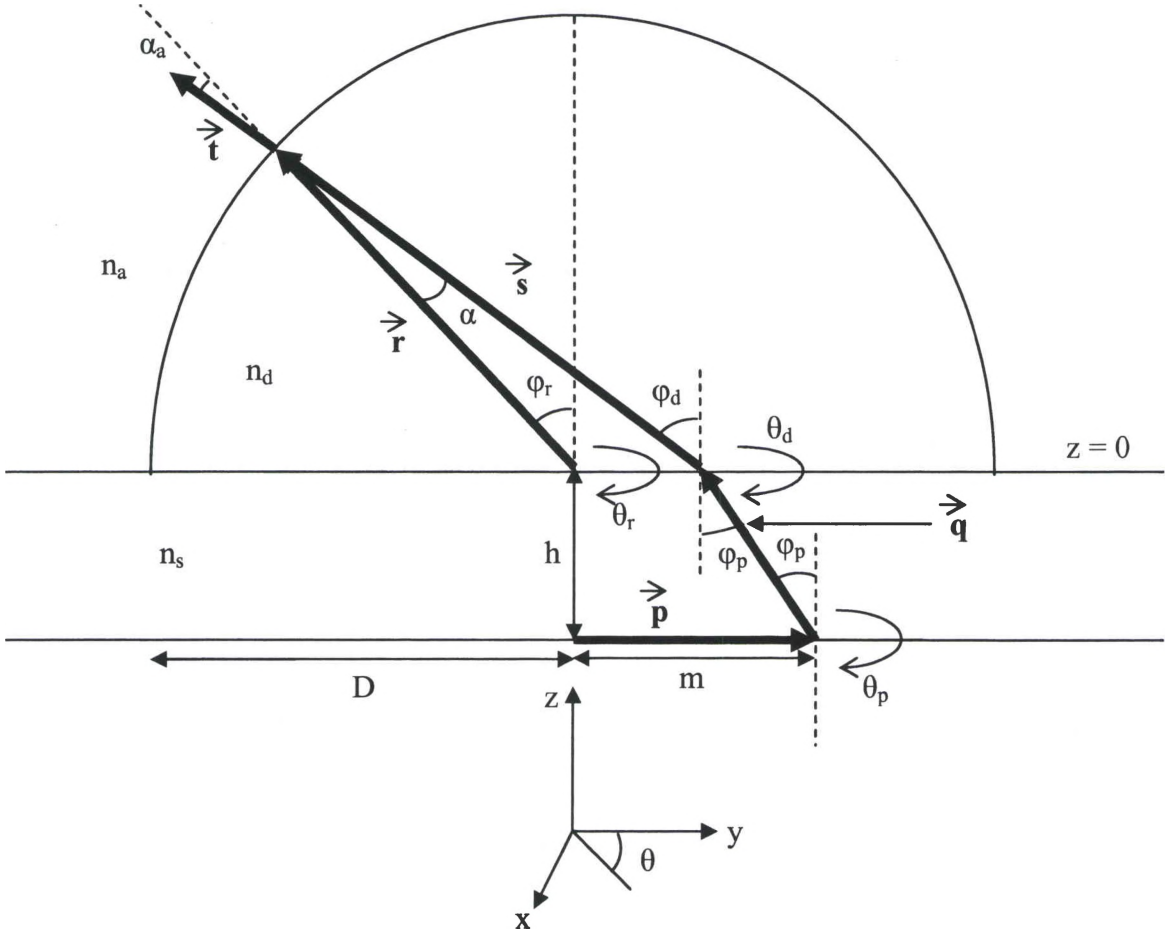


**Figure B.1** Diagram of the parameters used in the derivation

$$\vec{p} = m\hat{y} - h\hat{z}$$

$$\vec{q} = \vec{p} + h\hat{z} + h\tan\varphi_p \sin\theta_p \hat{x} + h\tan\varphi_p \cos\theta_p \hat{y}$$

$$\vec{q} = (m\hat{y} - h\hat{z}) + h\hat{z} + h\tan\varphi_p \sin\theta_p \hat{x} + h\tan\varphi_p \cos\theta_p \hat{y}$$

$$\vec{q} = h\tan\varphi_p \sin\theta_p \hat{x} + (h\tan\varphi_p \cos\theta_p + m)\hat{y}$$

**Find t:**

Snell's Law:

$$n_s \sin\varphi_p = n_d \sin\varphi_d$$

$$\theta_d = \theta_p$$

Law of Sines:

$$\frac{s}{\sin(90^\circ + \varphi_r)} = \frac{r}{\sin(90^\circ - \varphi_d)}$$

$$\frac{s}{\cos\varphi_r} = \frac{r}{\cos\varphi_d}$$

Eq. 1:

$$r\cos\varphi_r = s\cos\varphi_d$$

Eq. 2:

$$r\sin\varphi_r \cos\theta_r = s\sin\varphi_d \cos\theta_d + q_y$$

Eq. 3:

$$r\sin\varphi_r \sin\theta_r = s\sin\varphi_d \sin\theta_d + q_x$$

(Eq. 2) ^ 2:

$$r^2 \sin^2 \varphi_r \cos^2 \theta_r = \left[ s \sin \varphi_d \cos \theta_d + q_y \right]^2$$

$$r^2 \sin^2 \varphi_r \cos^2 \theta_r = s^2 \sin^2 \varphi_d \cos^2 \theta_d + 2q_y(s) \sin \varphi_d \cos \theta_d + {q_y}^2$$

(Eq. 3) ^ 2:

$$r^2 \sin^2 \varphi_r \sin^2 \theta_r = \left[ s \sin \varphi_d \sin \theta_d + q_x \right]^2$$

$$r^2 \sin^2 \varphi_r \sin^2 \theta_r = s^2 \sin^2 \varphi_d \sin^2 \theta_d + 2q_x(s) \sin \varphi_d \sin \theta_d + {q_x}^2$$

(Eq. 2) ^ 2 + (Eq. 3) ^ 2:

$$\begin{aligned} & r^2 \sin^2 \varphi_r \cos^2 \theta_r + r^2 \sin^2 \varphi_r \sin^2 \theta_r \\ & = s^2 \sin^2 \varphi_d \cos^2 \theta_d + s^2 \sin^2 \varphi_d \sin^2 \theta_d \\ & + 2q_y(s) \sin \varphi_d \cos \theta_d + 2q_x(s) \sin \varphi_d \sin \theta_d + {q_y}^2 + {q_x}^2 \end{aligned}$$

$$\begin{aligned} & r^2 \sin^2 \varphi_r (\sin^2 \theta_r + \cos^2 \theta_r) \\ & = s^2 \sin^2 \varphi_d (\sin^2 \theta_d + \cos^2 \theta_d) + 2(s) \sin \varphi_d (q_y \cos \theta_d + q_x \sin \theta_d) + {q_y}^2 + {q_x}^2 \end{aligned}$$

(Eq. 2) ^ 2 + (Eq. 3) ^ 2 = Eq. 4:

$$r^2 \sin^2 \varphi_r = s^2 \sin^2 \varphi_d + 2(s) \sin \varphi_d (q_y \cos \theta_d + q_x \sin \theta_d) + {q_y}^2 + {q_x}^2$$

Eq. 4 (LHS):

$$r^2 \sin^2 \varphi_r = r^2 (1 - \cos^2 \varphi_r)$$

Eq. 1:

$$\cos \varphi_r = \frac{s \cos \varphi_d}{r}$$

Eq. 4 (LHS):

$$r^2 \sin^2 \varphi_r = r^2 \left[ 1 - \left( \frac{s \cos \varphi_d}{r} \right)^2 \right] = r^2 \left[ \frac{r^2 - s^2 \cos^2 \varphi_d}{r^2} \right]$$

$$r^2 \sin^2 \varphi_r = r^2 - s^2 \cos^2 \varphi_d$$

Eq. 4:

$$r^2 - s^2 \cos^2 \varphi_d = s^2 \sin^2 \varphi_d + 2(s) \sin \varphi_d (q_y \cos \theta_d + q_x \sin \theta_d) + {q_y}^2 + {q_x}^2$$

$$0 = -r^2 + s^2 (\sin^2 \varphi_d + \cos^2 \varphi_d) + 2(s) \sin \varphi_d (q_y \cos \theta_d + q_x \sin \theta_d) + {q_y}^2 + {q_x}^2$$

$$s^2 + 2(s) \sin \varphi_d (q_y \cos \theta_d + q_x \sin \theta_d) + {q_y}^2 + {q_x}^2 - r^2 = 0$$

Quadratic Equation:

$$s = \frac{-b \pm \sqrt{b^2 - 4ac}}{2a}$$

Where:

$$a = 1$$

$$b = 2 \sin \varphi_d (q_y \cos \theta_d + q_x \sin \theta_d)$$

$$c = {q_y}^2 + {q_x}^2 - r^2$$

$$s = \frac{\left[ -2\sin\varphi_d (q_y \cos\theta_d + q_x \sin\theta_d) \pm \sqrt{4\sin^2\varphi_d (q_y \cos\theta_d + q_x \sin\theta_d)^2 - 4({q_y}^2 + {q_x}^2 - r^2)} \right]}{2}$$

$$s = -\sin\varphi_d (q_y \cos\theta_d + q_x \sin\theta_d) + \sqrt{\sin^2\varphi_d (q_y \cos\theta_d + q_x \sin\theta_d)^2 - ({q_y}^2 + {q_x}^2 - r^2)}$$

**Find $\theta_r$ and $\varphi_r$:**

Numerator = Eq. 3 (RHS), Denominator = Eq. 2 (RHS):

$$\theta_r = \tan^{-1}\left[ \frac{s\sin\varphi_d \sin\theta_d + q_x}{s\sin\varphi_d \cos\theta_d + q_y} \right]$$

Eq. 1:

$$\varphi_r = \cos^{-1}\left[ \frac{s\cos\varphi_d}{r} \right]$$

$$\vec{t} = r\sin\varphi_r \sin\theta_r \hat{x} + r\sin\varphi_r \cos\theta_r \hat{y} + r\cos\varphi_r \hat{z}$$

**Find $\alpha$:**

$$\cos\alpha = \frac{\vec{t} \cdot (\vec{t} - \vec{q})}{|\vec{t}| \cdot |\vec{t} - \vec{q}|}$$

Snell's Law:

$$n_d \sin\alpha = n_a \sin\alpha_a = \sin\alpha_a$$

**Find the reflection coefficients:**

$$R_{s-d}(\varphi_p)=\frac{1}{2}\left[\left(\frac{n_s\cos\varphi_p-n_d\cos\varphi_d}{n_s\cos\varphi_p+n_d\cos\varphi_d}\right)^2+\left(\frac{n_s\cos\varphi_d-n_d\cos\varphi_p}{n_s\cos\varphi_d+n_d\cos\varphi_p}\right)^2\right]$$

$$R_{d-a}(\alpha)=\frac{1}{2}\left[\left(\frac{n_d\cos\alpha-\cos\alpha_a}{n_d\cos\alpha+\cos\alpha_a}\right)^2+\left(\frac{n_d\cos\alpha_a-\cos\alpha}{n_d\cos\alpha_a+\cos\alpha}\right)^2\right]$$

**Find the transmission coefficients:**

$$T_{s-d}(\varphi_p)=1-R_{s-d}(\varphi_p)$$

$$T_{d-a}(\alpha)=1-R_{d-a}(\alpha)$$

**Find $\eta_{ext}$:**

$$\eta_{ext}=\frac{\int_{m=0}^{D}\int_{\varphi_p=0}^{\pi/2}\int_{\theta_p=0}^{2\pi}\cos\varphi_p(2\pi)(m)dmT_{s-d}(\varphi_p)T_{d-a}(\alpha)\sin\varphi_p d\theta_p d\varphi_p}{2\int_{m=0}^{D}\int_{\varphi_p=0}^{\pi/2}\int_{\theta_p=0}^{2\pi}\cos\varphi_p\sin\varphi_p(2\pi)(m)dmd\theta_p d\varphi_p}$$

$$\eta_{ext}=\frac{\int_{m=0}^{D}\int_{\varphi_p=0}^{\pi/2}\int_{\theta_p=0}^{2\pi}\cos\varphi_p(m)T_{s-d}(\varphi_p)T_{d-a}(\alpha)\sin\varphi_p d\theta_p d\varphi_p dm}{2\left[\frac{m^2}{2}\right]\Big|_0^D\left[\frac{\sin^2\varphi_p}{2}\right]\Big|_0^{\pi/2}(2\pi)}$$

$$\eta_{ext}=\frac{\int_{m=0}^{D}\int_{\varphi_p=0}^{\pi/2}\int_{\theta_p=0}^{2\pi}(m)T_{s-d}(\varphi_p)T_{d-a}(\alpha)\cos\varphi_p\sin\varphi_p d\theta_p d\varphi_p dm}{D^2\pi}$$

# VITA

| | |
|---|---|
| December 4, 1979 | Born – Lexington, Kentucky |
| 2002 | B.S., Xavier University, Cincinnati, Ohio |
| 2000-2002 | Research Assistant, Department of Physics<br>Xavier University, Cincinnati, Ohio |
| 2004 | M.S., University of Dayton, Dayton, Ohio |
| 2002-2004 | Student Trainee (Electrical Engineering),<br>Sensors Directorate<br>Air Force Research Laboratory, WPAFB, Ohio |

## PUBLICATIONS/CONFERENCE APPERANCES

Techniques for Shadow Mask Deposition of Non-planar Dielectric Layers, IEEE/LEOS 16th Annual Meeting, October 2003, Tucson, Arizona.

Techniques for Shadow Mask Deposition of Non-planar Dielectric Layers, Great Lakes Photonics Symposium, June 2004, Cleveland, Ohio.

## FIELDS OF STUDY

Major field; Optoelectronic Devices

Semiconductor Lasers and LEDs, Professor Andrew M. Sarangan and colleague Thomas R. Nelson

Shadow Mask Deposition of Dielectrics, Professor Andrew M. Sarangan and colleague Thomas R. Nelson